# 3.2 First-Principles Calculation of Material Properties

# Theoretical study on dynamical processes in heterogeneous catalysis using density functional theory and machine learning methods

H. H. HALIM, T. N. PHAM,Y.-L. WANG, T. OTA, S. E. M. PUTRA
Y. HAMAMOTO, K. INAGAKI, I. HAMADA, and Y. MORIKAWA
*Department of Precision Engineering, Graduate School of Engineering, Osaka University, 2-1 Yamadaoka Suita, Osaka 565-0871*

In 2022-2023, we carried out theoretical investigation of chemical processes at surfaces and interfaces, Cu-Zn surface alloy formation on Cu(997), Hydrogenation of formate species using atomic hydrogen on a Cu(111) model catalyst, oxygen vacancy migration in $SrFeO_{3-\delta}$ and $Sr_3Fe_2O_{7-\delta}$, NO-H2O coadsorption on Cu(111), and activity and selectivity of $N_2$ fixation on B doped g-$C_9N_{10}$.

In this report, we report Cu-Zn surface alloy formation on Cu(997)[1]. The catalysts based on metal-alloys are well recognized in the field of heterogenous catalysis considering the emerging of unique properties upon alloying. Given the optimal composition and environment, these catalysts can offer high catalytic performance that outperform their alloy constituents. There have been notorious examples on the application of metal-alloy based catalysts in heterogenous catalysis. In the present study, we focus on Cu-Zn surface alloy which has been reported to be very active for methanol synthesis by hydrogenation of $CO_2$. Experimental studies have shown that the deposition of Zn on Cu(111) promotes the activity of methanol production by an order of magnitude at Zn coverage of 0.197. In addition, the Cu-Zn alloy has been reported as a good model of $Cu/ZnO/Al_2O_3$ (CZA), the industrial catalyst used to synthesize methanol by hydrogenation of $CO_2$. Thus, this alloy has been extensively involved in the investigation of the true active site of CZA which remains under controversy.

Recently, it was reported that by coupling Molecular Dynamics (MD), active-learning, and automated event detection, Lim et al. have successfully reveal the restructuring mechanisms of Pd deposited on Ag. By adopting similar methodologies, we performed MD simulation of Zn depositions on Cu(997) surface to explicitly capture the mechanisms that are responsible to the Cu-Zn surface alloying. The MD simulations were implemented based on force-field that was trained by means of Gaussian Process (GP). The database, containing information of atomic forces acting on various environments, were obtained from DFT calculations. The task of training was done by using Fast Learning of Atomistic Rare Events (FLARE) code which utilizes the uncertainty information from GP, together with active on-the-fly learning scheme to build the force-field efficiently.

We used DFT calculations to provide forces of the central atom on each atomic environment. All DFT calculations were performed using the STATE code. The electron-ion interaction was described by ultrasoft pseudopotentials. We took into account the van der Waals (vdW) interactions by applying optB86b-vdW exchange correlation functional as implemented in the STATE code.

To construct GP force-field, we used FLARE

code with two- and three-body multispecies kernels. The interaction cutoffs for two- and three-body kernels are set to 7.0 Å and 4.5 Å, respectively. The hyperparameters embedded to these kernels, namely two-body signal variances ($\sigma_2$), two-body length scale ($l_2$), three-body signal variances ($\sigma_3$), three-body length scale ($l_3$), and noise hyperparameter ($\sigma_n$) was optimized by maximizing the log marginal likelihood using BFGS algorithm as implemented in SciPy used inside the FLARE code. The database is constructed by employing active and on-the-fly learning scheme that update the database based on uncertainty information calculated by GP. In order to provide new atomic environments to be candidate for the database, MD code internal to FLARE is used to evolve atomic structures with 1 fs timestep within canonical (NVT) ensemble. The temperature is set up at 700 K with all atoms are allowed to move. To obtain more diverse atomic environments, we manually changed the initial structure after certain MD steps during the on-the-fly learning when no significance improvement in the Mean Absolute Error (MAE) was found. The details of this procedure and the resulting database are reported in the next section.

To observe the alloying process of Cu-Zn, we performed MD simulations within NVT ensemble at temperature 700 K for up to 6.25 $\mu$s. Figure 1 shows the evolution of deposited Zn atoms on Cu(997) until the Cu-Zn surface alloy is formed. To clearly observed the number of Zn atoms that substituted at the terrace, we also plotted the composition of Cu and Zn atoms as a function of rows for every certain timesteps. Such plots accompany each MD snapshots in Figure 1. The snapshots of the MD simulation are also presented as video in the Supporting Information. In the beginning (Figure 6a), the Zn atoms are found to localize at the step edge, covering the original Cu step adatoms. The profile of boundary between Cu and Zn is still fairly linear. After 1.25 $\mu$s, some of the Zn atoms are incorporated

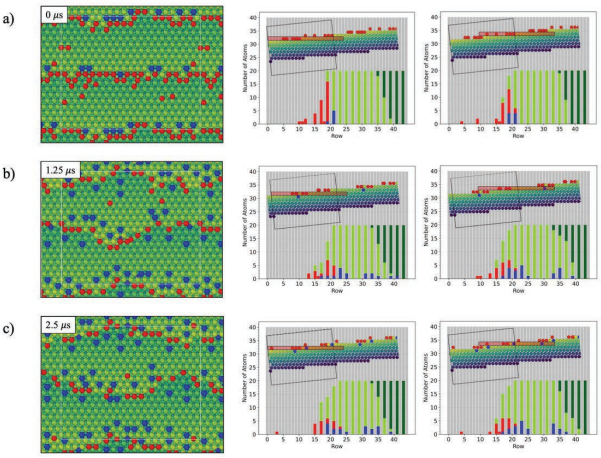


Figure 1: The snapshots of MD simulations showing the evolution of deposited Zn atoms on Cu(997). The green to yellow atom indicates the Cu atom, the red atom indicates Zn as adatom, and blue atom indicates substituted Zn atom. The two plots accompanied each snapshot show the composition of atom as a function of row. In each plot, the red, blue, light green, and dark green bars indicate the number of Zn as adatom, Zn as incorporated atom, Cu as surface atom, and Cu atom which is covered by additional Cu or Zn layer.

at the upper and lower terrace near the step edge (Figure 1b). At this stage, almost no Zn atoms are incorporated at the middle terrace. We also noticed Zn atoms are dominantly incorporated to the upper terrace whereas only few incorporated Zn atoms found at the lower terrace. After 2.5 $\mu$s (Figure 1c), the distribution of the Zn on the surface and the number of incorporated Zn atom are still relatively similar.

## References

[1] Harry Handoko Halim and Yoshitada Morikawa: ACS Physical Chemistry Au **2**, 430-447 (2022).

# Prediction of Material Properties using Density Functional Theory

Osamu Sugino

*Institute for Solid State Physics,*

*The University of Tokyo, Kashiwa-no-ha, Kashiwa, Chiba 277-8581*

We have studied properties of cuprate superconductors and zirconia cathode materials using the SCAN and PBE exchange-correlation (xc) functionals, respectively, of the density functional theory (DFT). Our DFT calculations of cuprates reproduced lattice properties and electronic band structures consistent with available experimental data and predicted properties of layered ones [1]. Our calculated free energy landscape for the oxygen reduction reaction occurring on the zirconia surface suggested that a high reactivity appears not only when doped with nitrogen atoms and oxygen vacancies also in the pristine conditions. It is therefore possible that the role of defects may be increase of the carrier conductivity rather than enhancement of the reactivity [2].

We have used for the electronic structure calculations the packages VASP and Quantum Espresso implemented in the ISSP supercomputers. We have used for modeling the defective zirconia the abICS package developed by S. Kasamatsu [3].

The accuracy of the xc functionals is essential in providing reliable prediction of material properties. We tried to improve the accuracy using a machine learning method. We used the accurate electronic structures of small molecules provided by a quantum chemical calculation together with the theoretically derived properties of the xc functionals [4]. Those different data of molecules and theory are found to play a complementary role in increasing the accuracy and numerical stability of the functional as demonstrated by calculation of various crystals.

References

[1] A. N. Tatan, et al., AIP Advances 12, 105308 (2022).

[2] S. Muhammady, et al., J. Phys. Chem. C 126, 15662 (2022).

[3] https://www.pasums.issp.u-tokyo.ac.jp/abics

[4] R. Nagai et al., Phys. Rev. Research 4, 013106 (2022); Electron. Struct. 1, 37-38 (2022).

# Clarification of Microscopic Mechanisms of Semiconductor Epitaxial Growth and Device-Interface Formation by Large-Scale Quantum-Theory-Based Computations

Atsushi Oshiyama

*Institute of Materials and Systems for Sustainability, Nagoya University*

*Furo-cho, Chikusa-ku, Nagoya 464-8601*

In the fiscal year of 2022, on the basis of the total-energy electronic-structure calculations and molecular dynamics simulations within the density-functional theory (DFT), we have studied the epitaxial growth of wide-gap semiconductors and graphene sheets, atomic and electronic structures of semiconductor surfaces and their interfaces with insulators. The main computational tools are our RSDFT (Real Space DFT) code and RS-CPMD (Car-Parrinello Molecular Dynamics) code as well as VASP code. Specifically, we have studied 1) the atom-scale mechanism of GaN epitaxial growth [1,2], 2) the mechanism of graphene growth on SiC surfaces [3], 3) atomic and electronic structures of stepped SiC surfaces [4] and GaN/AlSiO interfaces [5], and 5) the role of point defects in SiN which have been speculated to be the principal element of current flash memories. The below is the explanation of the issues 2) and 5) above.

## Initial stage of graphene formation on SiC(0001) Surfaces

Graphene has a consolidated background as an innovative two-dimensional (2D) material because of the peculiar electronic and mechanical properties. Several methods have been proposed to produce graphene sheets. Among them, an emerging technology consists in the thermal decomposition of silicon carbide (SiC). The major advantage of this technique is the possibility of growing graphene directly on a semiconducting substrate, thus avoiding the difficult step of extracting and transferring graphene sheets on a substrate. From a scientific standpoint, the formation of graphene from a SiC crystal, possibly

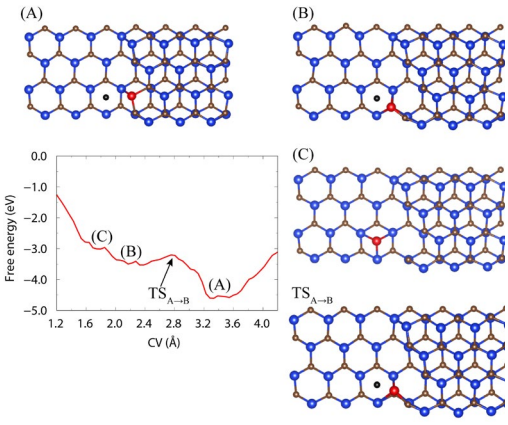


Fig. 1: Free-energy profile of Si desorption from the step edge and major relevant configurations. The color code for the atoms is blue for Si and brown for C. The collective variable (CV) used in the meta-dynamics is the distance between a desorbing Si (red sphere) and the center of mass (black sphere) of the lower terrace site formed by three C atoms.

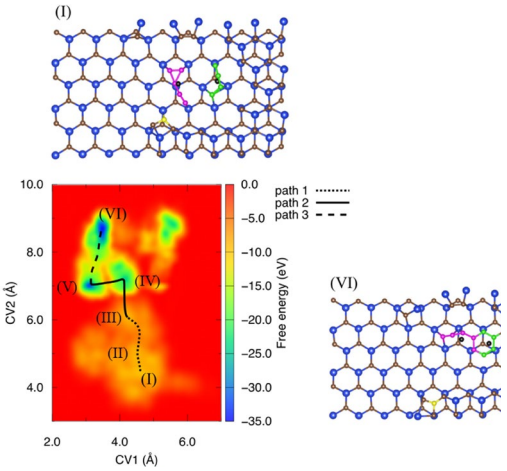


Fig. 2: Free-energy landscape (the bottom-left) and minimum free-energy reaction pathway (path1 + path2 + path3: the dotted, solid and dashed lines) for the clustering of carbon atoms. The labels from (I) to (VI) in the landscape indicate the positions of the (meta) stable configurations along the pathway. The stable configurations (I) and (VI) are shown in the top-left and the bottom-right, respectively. In (I), C5 and C4 clusters are highlighted with magenta and green spheres, respectively. Those clusters become a single cluster C9 in the final configuration (VI). The CV1 is the distance between the COM of C5 (left black sphere) and COM of C4 (right black sphere) and the CV2 is the distance between the COM of C5 and a C atom (yellow sphere).

accompanied by a selective removal of Si atoms and subsequent condensation of C atoms, is still an unexplored issue.

Based on the first principles molecular dynamics empowered by free energy sampling methods, we have clarified atomistic processes of the initial stage of graphene formation on SiC(0001). Our simulations have shown that the desorption of a Si atom from a step edge and its subsequent migration to a stable site on the nearby terrace is an endothermic reaction (Fig. 1). Yet, this step is an essential initial trigger to the process that eventually will lead to the formation of a graphene sheet. We have found that a subsequent Si desorption leaves behind under-coordinated C atoms and this, in turn, triggers the formation of three stable C-C bonds via an exothermic reaction. This second step paves the route to the formation of larger carbon structure at the SiC(0001) surface. Following the guidelines that these simulations indicate, we focused on the processes occurring upon desorption of several Si atoms. We have clarified how small C clusters formed at the exposed surface can merge into a larger structure presenting a C6 ring, the expected seed of a graphene-like conformation (Fig. 2). The extension of this carbon bond network realized in this way is accompanied by a remarkable energy gain, leading to an exothermic reaction and to a stable carbon structure precursor of an actual graphene flake.

## Nitrogen Vacancy in Silicon Nitride: Emergence of Floating Gap States

Silicon nitride（SiN）thin films are fabricated near interfaces of Si-MOS structures, and utilized as memory elements in non-volatile flash memories which sustain our energy-saving society. The microscopic mechanism of the memory function is unknown, however. We have performed DFT calculations with hybrid approximation to the exchange-correlation functional and clarified the atomic and electronic structures of nitrogen vacancy ($V_N$) in SiN. The results indicate that the floating electron state inherent to host SiN is localized near $V_N$ and induce a gap state which is free from energy

barriers upon electron capture and emission, thus being a strong candidate for the memory unit.

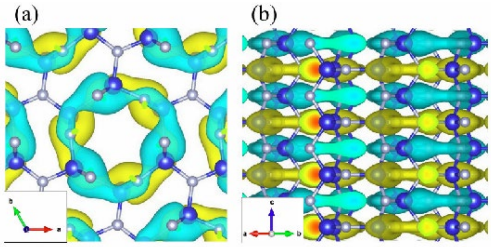


Fig. 3: KS orbital of the CBB of β-$Si_3N_4$ viewed from *c* axis (a) and from its perpendicular direction (b). The isovalue surface of the KS orbital is shown by the yellow (+) and bluegreen (-) blobs. The blue and gray balls depict Si and N atoms, respectively.

Figure 3 shows the Kohn-Sham (KS) orbital of the conduction-band bottom (CBB) of SiN (its crystalline form β-$Si_3N_4$). The orbital is distributed not near atomic sites but in the internal space, showing the *floating* character. We have found from the DFT calculations that the floating state is ubiquitous in various sparse materials such as carbon nanomaterials and even in typical tetrahedral-symmetry semiconductors [Matsushita, Oshiyama: PRL 2012, 2014, Nano Lett. 2017].

When a single N atom is removed from SiN (i.e., $V_N$), the nearest neighbor three Si atoms lose their partner, inducing 3 Si dangling bonds (DBs). These DB states are linear combined and induce a totally symmetric state in the valence band and remaining two states in the gap. Depending on the position of the Fermi level in the gap, $V_N$ changes its charge state from +1 to -3, showing interesting competition between the Jahn-Teller splitting and the exchange splitting.

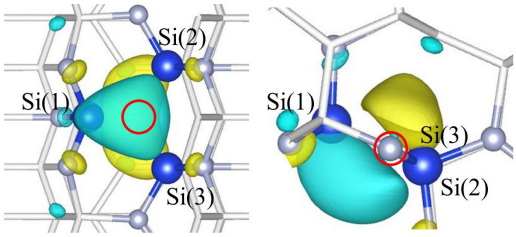


Fig. 4: KS orbital of localized the floating state in the gap of SiN. Isovalue surface of the orbital from (a) a perpendicular and (b) a parallel directions to a plane consisting of 3 neighbor Si atoms.

More interestingly, the floating state near CBB (Fig. 3) capture additional electrons and localized near $V_N$ (Fig. 4). This is due to the ionicity of SiN: The N atom in SiN is an anion so that $V_N$ is effectively positive, thus attracting electrons. This generates additional gap states, making $V_N$ multiply charged. The floating state localized in the N-deficit region may be responsible for the memory function.

The group id codes for the achievements above are k0042 and m0037.

## Related publications

[1] M. Boero, K. M. Bui, K. Shiraishi, K. Ishisone, Y. Kangawaa, and A. Oshiyama, Appl. Surf. Sci. **599**, 153935 (2022).
[2] K. M. Bui, K. Shiraishi and A. Oshiyama, Appl. Surf. Sci. **613**, 155840 (2023).
[3] M. Boero, F. Imoto and A. Oshiyama, Phys. Rev. Materials **6**, 093403 (2022).
[4] T. Kimura, K. Chokawa, K. Shiraishi, and A. Oshiyama, Phys. Rev. B **106**, 035309 (2022).
[5] K. Chokawa, K. Shiraishi and A. Oshiyama, J. Appl. Phys **133**, 065301 (2023).
[6] F. Nanataki, K. Shiraishi, J.-I. Iwata, Y.-i. Matsushita, and A. Oshiyama, Phys. Rev. B **106**, 155201 (2022)

# Understanding structure-property relationships of disordered materials using first-principles based high-throughput simulation framework

Shusuke KASAMATSU

*Academic Assembly (Faculty of Science),*

*Yamagata University, Kojirakawa, Yamagata-shi, Yamagata 990-8560*

Characterizing the order within disorder of atomic arrangements in materials is imperative for predicting, understanding, and designing a wide variety of materials functionalities such as electronic, ionic, and thermal conductivity/insulation and catalytic activity. Recently, we have been focusing on developing methods to perform sufficient statistical thermodynamics sampling in disordered systems, and we have also started to consider how to analyze such huge amounts of data to extract meaningful structure-property relationships.

For sampling of disordered crystalline systems, we had already introduced our abICS (ab Initio Configuration Sampling) framework for deriving an on-lattice neural network model from first-principles calculations in past Activity Reports [1]. This year, we benchmarked its performance on calculating temperature-dependent disorder in the cation sublattice of three spinel oxides. The efficiency of the approach in an active-learning setting was demonstrated clearly against random sampling, and issues such as accuracy degradation vs. lattice relaxation and the ability to learn energetics for varying compositions were discussed [2].

As a first application to an unsolved materials science problem, abICS was used to understand the hydration behavior of heavily Sc-doped $BaZrO_3$, known as a promising perovskite proton conductor for solid oxide fuel cells. Although this class of materials has been known as a good proton conductor for 40 years, the local structure that activates the hydration reaction, which is the key reaction to introduce protons into the system, remained unknown. Using abICS, we simulated the ratio of Sc-$V_O$-Sc, Sc-$V_O$-Zr, and Zr-$V_O$-Zr that contribute to hydration under experimental thermodynamic conditions. We also obtained a machine-learning model for lattice volumes and predicted doping and hydration-dependent lattice constants in excellent agreement with experiment. Careful comparison with *in situ* XAS and thermogravimetry measurements lead to the conclusion that Sc-$V_O$-Sc and Sc-$V_O$-Zr are the active sites for hydration [3].

In the case of liquid and amorphous systems, we have been relying on available software for neural network potential training such as

Simple-NN [4]. Training a reliable model for liquid and amorphous systems up to two components is now relatively easy to achieve, and for such systems, we have now started to consider how to understand the order within disorder. Towards this end, we have been examining the applicability of topological data analysis [5], which characterizes the structure in terms of the size and shapes of rings and cavities. Figure 1 shows the temperature-dependent first order persistence diagram for liquid and amorphous $ZnCl_2$, where each dot corresponds to a ring of Zn atoms; the "birth" axis corresponds to the bond distance for forming the rings, and the "death axis" roughly corresponds to the roundness of the rings. A clear change is seen in the ring distribution vs. temperature, suggesting that we can characterize the subtle difference between liquid and amorphous $ZnCl_2$ in terms of the intermediate-range order, which may be related to the exponential decay in viscosity at the glass transition.

## References

[1] S. Kasamatsu, ISSP Supercomputer Center Activity Report 2020, pp. 16-26.

[2] S. Kasamatsu et al., J. Chem. Phys. **157**, 104114 (2022).

[3] K. Hoshino, S. Kasamatsu, et al., Chem. Mater. **35**, 2289-2301 (2023).

[4] K. Lee et al., Comp. Phys. Comm. **242**, 95 (2019).

[5] I. Obayashi et al., J. Phys. Soc. Jpn., **91**, 091013 (2022).

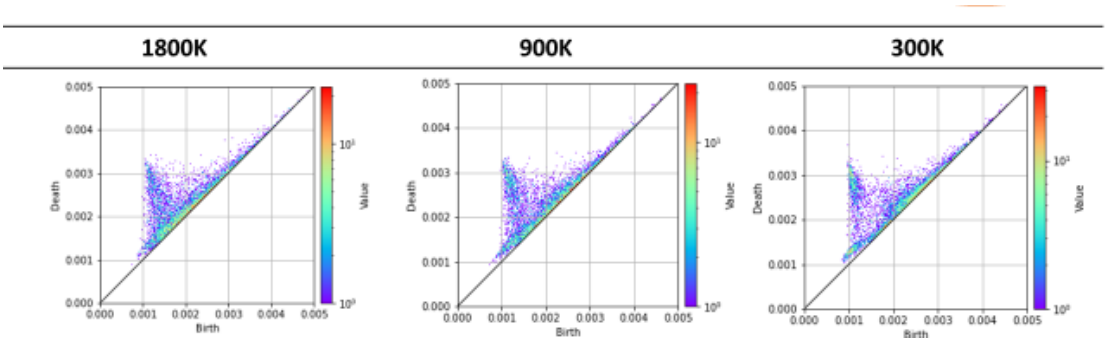


Fig. 1: First order persistence diagrams of liquid and amorphous $ZnCl_2$.

# Development of first-principles calculation code RSPACE and design of highly functional interface

Tomoya ONO
*Graduate School of Engineering, Kobe University*
*Rokkodai-cho, Nada, Kobe 657-8501*

4H-silicon carbide (4H-SiC) is an IV-IV type semiconductor with a wide band gap of 3.2 eV, and the 4H-SiC based metal-oxide-semiconductor field-effect transistor (MOSFET) is expected to be used in next generation switching devices operating at high power and high frequency applications. However, the potential of 4H-SiC has not been fully utilized owing to the low on current of MOSFETs, which is caused by defects at the 4H-SiC/$SiO_2$ interface. The post-oxidation annealing process using $N_2O$, NO, or $N_2$ gas has been proposed to reduce the density of interface defects and increase the on current. In our previous study, we investigated the total energies and electronic structures of the nitride layers by density functional theory (DFT) calculation using the surface models, where the 4H-SiC/$SiO_2$ interfaces are modeled by the OH terminated surfaces. However, the surface models do not include the effect of the $SiO_2$ networks on the interface atomic structure. In this project of 2022, we employ the models containing the $SiO_2$ layers on the SiC substrate.

Figure 1 shows our computational models, where the surface of the 4H-SiC substrate is terminated with the $SiO_2$ layer and the other side of the substrate is terminated with H atoms. The rectangular supercells of 10.1 Å × 5.3 Å × 26.3 Å for the *a*-face model, 10.1 Å × 6.2 Å × 27.3 Å for the *m*-face model, and 18.5 Å × 5.3 Å × 26.8 Å for the Si-face model were employed. The *z*-axis was taken to be the direction perpendicular to the surface. We considered the modification incorporating four Si vacancies ($V_{Si}$s) and 16 N atoms at C sites ($N_C$s). The cases in which $V_{Si}$s were arranged parallel to the surface were investigated to evaluate the anisotropy of the formation energy of the nitride layer. In our model, the areal N-atom density was on the order of $10^{14}$ $cm^{-1}$, which is consistent with the experimental results. Although there are two inequivalent lattice sites of 4H-SiC, i.e., *h* (hexagonal) and *k* (quasi-cubic) sites, our previous studies have shown that nitride layers tend to grow at the *k* site. Thus, we consider the cases in which $V_{Si}$s are arranged at the *k* site. We also investigated the interfaces with the nitride layer at the second layer for all the faces. For the first-principles calculation, we used the RSPACE code[1, 2], which is based on the real-space finite-difference approach within the frameworks of density functional theory (DFT) and is developed in this project. We employed the local density approximation of the DFT to describe the exchange and correlation effects. Electron-ion interactions were approximated by the projector-augmented wave method. The structural optimization was performed until the residual forces are smaller than 0.001 Hartree/Bohr radius.

The formation energy of the above interaction for generating one $V_{Si}$ to insert a nitride layer was obtained as

$$E_{\rm form} = E_{\rm total}^{(\rm w/\ mod)}/4 + E(SiO_2) + 4\mu_{CO} + 2\mu_N - E_{\rm total}^{(\rm w/o\ mod)}/4 - 6\mu_{NO}, \quad (1)$$

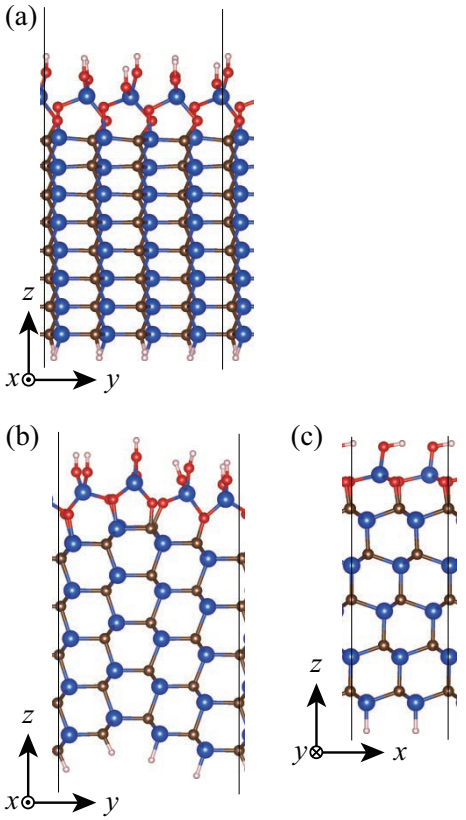


Figure 1: Interface atomic structures with CO bonds for (a) $a$-, (b) $m$-, and (c) C-face models before N-atom incorporation. Blue, brown, red, and gray spheres are Si, C, O, and H atoms, respectively. Black lines are the boundaries of the supercell.

where $E(SiO_2)$ is the total energy of a $SiO_2$ unit in a bulk of quartz $SiO_2$. $E_{\rm total}^{(\rm w/o\ mod)}$ and $E_{\rm total}^{(\rm w/\ mod)}$ represent the total energies of the interface without and with N-atom incorporation, respectively. In addition, $\mu_{\rm NO}$, $\mu_{\rm CO}$, and $\mu_{\rm N}$ are the chemical potentials of a NO molecule, a CO molecule, and N atoms in a $N_2$ molecule, respectively. We set the temperature at 1000 K and the partial pressure of NO gas ($p_{\rm NO}$) at 1 atm. The partial pressures of CO ($p_{\rm CO}$) and $N_2$ ($p_{N_2}$) gases were set at $10^{-5}$ atm and $0.25 \times 10^{-5}$ atm.

The formation energies of the nitride layers are shown in Fig. 2. All the reactions are exothermic and the nitride layers growing along the $a$ face are the most stable among

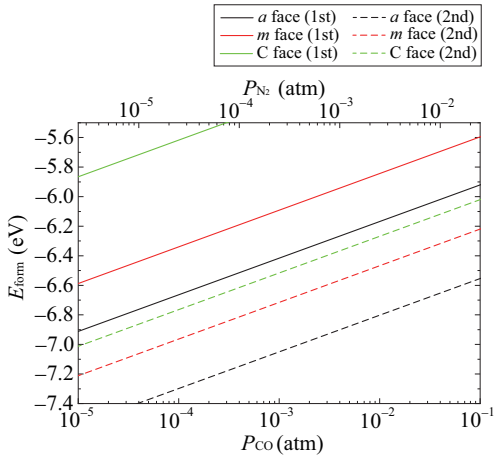


Figure 2: Formation energies $E_{\rm form}$ defined Eq. (1) for interface with CO bonds with respect to partial pressures of CO and $N_2$. Reprinted from Ref. 3.

those along the $a$, $m$, and Si faces. The formation energy of the nitride layer at the topmost layer is smaller than that at the second layer, resulting in the localization of the N atoms at the interface. Note that the NO annealing generates the nitride layers immediately below the $SiO_2$ layers without any transition layers. It was found that the effect from the $SiO_2$ layer on the interface atomic structure after the NO annealing and our conclusions derived by the surface models do not change when the $SiO_2$ layers are attached to the substrates.

## References

[1] T. Ono and K. Hirose, Phys. Rev. Lett. **82**, 5016 (1999).

[2] K. Hirose, T. Ono, Y. Fujimoto, and S. Tsukamoto, *First Principles Calculations in Real-Space Formalism, Electronic Configurations and Transport Properties of Nanostructures* (Imperial College, London, 2005).

[3] N. Komatsu, M. Ohmoto, M. Uemoto, and T. Ono, J. Appl. Phys. **132**, 155701 (2022).

# First-Principles Study on Carrier Mobility of $SiC_6$ Nanoribbons

Yoshiyuki EGAMI
*Division of Applied Physics, Faculty of Engineering, Hokkaido University*
*Kita 13, Nishi 8, Kita-ku, Sapporo, Hokkaido 060-8628*

In recent years, as semiconductor electronic devices have become smaller, a remarkable reduction in carrier mobility due to the thinning of silicon channels has become an important issue. Therefore, two-dimensional materials that can maintain high carrier mobility even with thin films have been attracting attention. A typical 2-dimensional material, graphene, has a carrier mobility of about 100 times that of silicon, and is therefore expected to become a post-silicon material. However, since the energy band gap of graphene is zero, it is difficult to apply it to semiconductor devices. So, several studies have been performed to open the gap. Among them, this work focuses on siligraphene, in which graphene is doped with silicon atoms. In particular, it is shown that $SiC_6$ siligraphene has a negative Poisson's ratio and a unique property that the carrier mobility changes significantly with strain. On the other hand, the carrier mobility of $SiC_6$ nanoribbons fabricated by cutting $SiC_6$ siligraphene as a channel material has not yet been clarified.

In this work, the carrier mobility of $SiC_6$ nanoribbon considering acoustic phonon scattering at room temperature is evaluated using the effective mass, elastic modulus, and deformation potential obtained by first-principles calculations [1]. As a result, the electron mobility of $SiC_6$ nanoribbons is significantly lower than that of $SiC_6$ siligraphene, but the hole mobility is sufficiently improved to be applied to $n$-type transistor materials. For future work, it is necessary to investigate the dependence of carrier mobility on the width and edge structure of the nanoribbon.

Ballistic electron transport properties in $SiC_6$ nanoribbons connected to semi-infinite electrodes consisting of graphene are also evaluated [1, 2]. There are two types of conduction channels: in the 1st channel, the scattering wave function is extended throughout the system via the delocalized $\pi$ orbitals of carbon atoms (Fig. 1(a)), resulting in a conduction channel with high transmission. On the other hand, in the 2nd channel, the scattering wave propagates via states consisting of $sp^3$ orbitals of silicon atoms, but most of the wave is reflected at nanoribbon region (Fig. 1(b)) and the transmission is quite small.

This work has been performed on System B of the Supercomputer Center, the Institute for Solid State Physics, the University of Tokyo.

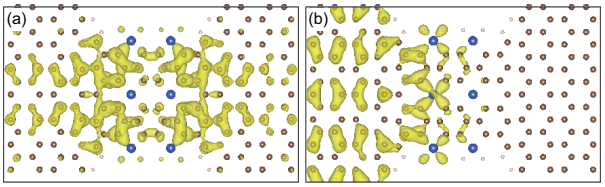


Figure 1: Charge density distribhutions of scattering wave functions.

## References

[1] K. Hirose *et al.*: First-principles calculations in real-space formalism (Imperial College Press, 2005).

[2] Y. Egami, S. Tsukamoto and T. Ono: Phys. Rev. Res. **3**, 013038 (2021).

# Analyses related to atomic structures and atom dynamics at complex structures such as surfaces, interfaces and defects

Satoshi WATANABE
*Department of Materials Engineering, the University of Tokyo*
*7-3-1 Hongo, Bunkyo-ku, Tokyo, 113-8656*

## 1 Introduction

To deepen our understanding on atomic arrangements and dynamics in/at complex structures such as surfaces, interfaces and defects is crucial for further development of novel information and energy devices. We have been tackling this issue using various simulation methods including multi-scale or machine-learning approaches. In the following, two of our results in fiscal year 2022 are described.

## 2 Defect structures in $WS_2$ thin films

Investigations on $WS_2$ aiming at electronic devices have been active recently. However, the performance of prototype devices were much lower than expected because of structural defects in fabricated $WS_2$ thin films. We examined [1] defect structures of $WS_2$ thin films using the high-dimiensional neural network potential (HDNNP). We successfully generated HDNNP with the root mean square error of energy from density functional theory (DFT) calculation of about 6 meV/atom. Molecular dynamics (MD) simulations using the HDNNP and $WS_2$ slab models reveal that S vacancies introduced in the slab are transformed into structures consisting of 5-memberd and 9-membered rings or other structures including rings different from 6-membered one spontaneously.

## 3 Electrical conductivity and Seebeck coefficient of organic semiconductors

Organic semiconductors have attracted much attention recently as thermoelectric materials. However, their power generation efficency is still insufficient for practical applications. We developed [2] a realistic evaluation method of the electrical conductivity and Seebeck coefficient of organic semiconductors using electronic structure calculations based on DFT. In our method, many structures were obtained using MD simulations with an empirical force field to consider thermal fluctuation in a crystal explicitly. The Seebeck coefficient and carrier mobility were obtained from the average of the density states and transfer integrals between adjacent moleculres calculated for each structure, respectively. We applied our scheme to pentacene and rubrene. Our results agree well with experimental data.

## References

[1] R. Otsuka, K. Shimizu, H. Wakabayashi, S. Watanabe: 70th JPSJ Spring Meeting 2023, 16p-B414-7 (in Japanese).

[2] M. Ohno, K. Shimizu, and S. Watanabe: Appl. Phys. Express **16** (2023) 011005.

# Theoretical study of point defects in visible-light-driven semiconductor photocatalysts using first-principles calculations

Seiichiro L. TEN-NO
*Graduate School of System Informatics, Kobe University*
*Rokkodai-Cho, Nada-Ku, Kobe 657-8501*

### Point Defect in Layered Perovskite Photocatalyst $Y_2Ti_2O_5S_2$

Layered perovskite $Y_2Ti_2O_5S_2$ (YTOS) is a strong candidate for semiconductor photocatalysts for overall water splitting under visible light. Although YTOS has a band gap sutable for absorption of visible light and valence/conduction band positions useful for overall water splitting, structural defects during synthesis should be controlled to promote photocatalytic performance [1, 2, 3].

We have investigated the point defects and electronic structures using first-principles calculations based on the density functional theory (DFT). The DFT calculations were performed within the PBE+$U$ (Perdew–Burke–Ernzerhof functional with Hubbard $U$ correction) functional using the projector augmented wave (PAW) method, as implemented in the Vienna ab initio simulation package (VASP).

We have evaluated the formation energy of anion vacancies $E_{\rm form}$ using the chemical potentials $\Delta\mu_i$ relative to bulk precipitate. $\Delta\mu_i$ were determined by the phase diagram of the relevant compounds in the synthesis of YTOS. Fig. 1(a) shows the phase diagrams as functions of $\Delta\mu_{\rm Ti}$ and $\Delta\mu_{\rm Y}$ for S-rich conditions, in which YTOS is stable within the area of the ABC triangle. In Fig. 1(b), $E_{\rm form}$ of $V_S$, $V_{O_c}$, and $V_{O_{ab}}$ for S-rich conditions is shown as a function of the Fermi level $E_{\rm F}$ measured from the valence band maximum $E_{\rm V}$. The evaluation of $E_{\rm form}$ suggests that the S-defect (O-defect) is easy to form when $E_{\rm F}$ is near the valence (conduction) band.

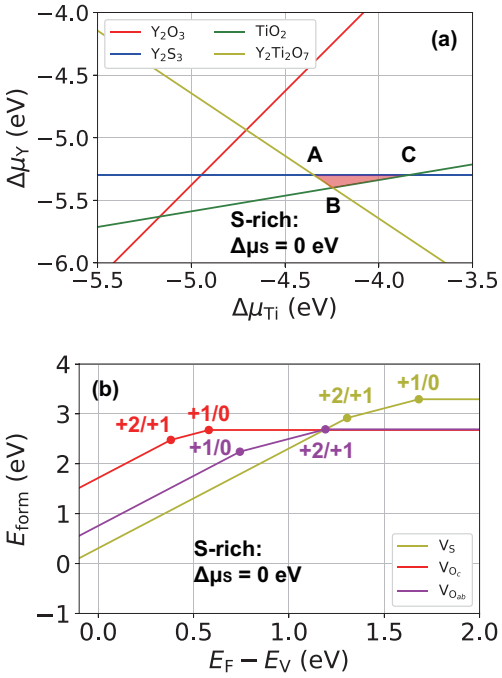


Figure 1: (a) Quaternary phase diagram of YTOS with respect to $\Delta\mu_{\rm Ti}$ and $\Delta\mu_{\rm Y}$ for S-rich conditions. (b) Formation energy of anion vacancies $E_{\rm form}$ against $E_{\rm F} - E_{\rm V}$.

### Chemical Doping in Perovskite Photocatalyst $SrTiO_3$

Perovskite $SrTiO_3$ (STO) is a typical semiconductor photocatalyst for overall water split-

ting under ultraviolet. According to the recent experiment [5], it is observed that Al-doped STO can enable a quantum efficiency of almost unity at wavelengths between 350 and 360 nm.

To explore more efficient dopants for higher-performance photocatalysts, we have studied the dopant effects on the electronic structures of STO using the first-principles analysis. The DFT calculations were performed within the PBE+$U$ functional using PAW method as implemented in VASP. We treated the supercell models including one $V_O$ and two $X_{Ti}$ (one $Mg_{Ti}$) with X being B, Al, Ga, In, Tl, Sc.

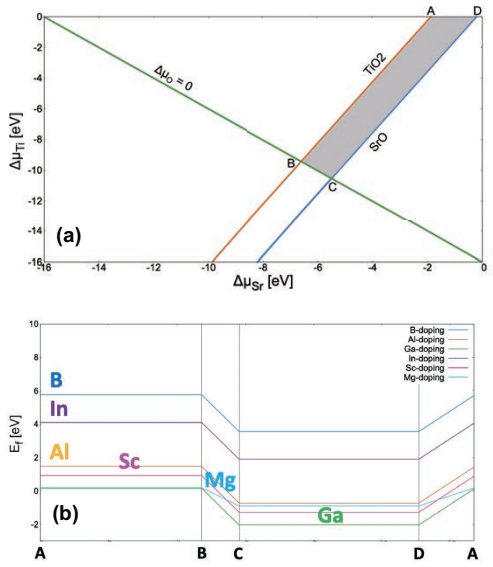


Figure 2: (a) Ternary phase diagram of STO with respect to $\Delta\mu_{Sr}$ and $\Delta\mu_{Ti}$. (b) Dopant formation energy of each dopnat $E_f$ along ABCD points.

The supercell calculations showed that each dopant except for Tl can cancel the defect level arising from the $V_O$. We have also evaluated the formation energy of each dopant $E_f$ using the chemical potentials $\Delta\mu_i$ relative to bulk precipitate. $\Delta\mu_i$ were determined by the phase diagram of the relevant compounds of STO. Fig. 2(a) shows the phase diagrams as functions of $\Delta\mu_{Sr}$ and $\Delta\mu_{Ti}$, in which STO is stable within the area of the ABCD square. In Fig. 2(b), $E_f$ of each dopant is shown along ABCD points.

### Water oxidation reaction on $BiVO_4$

Perovskite $BiVO_4$ (BVO) is used as an $O_2$-evolution photocatalyst for overall water splitting. We have investigated the reaction processes of the water oxidation on BVO using the first-principles calculations. The DFT calculations were performed within PBE and revised PBE (RPBE) using the slab models with (110) facet. Fig. 3 shows the energy diagram of $O_2$- and $H_2O_2$-evolution on BVO (110) surface, which suggests that $H_2O_2$-evolution is expected to be favorable on the (110) facet compared to $O_2$-evolution.

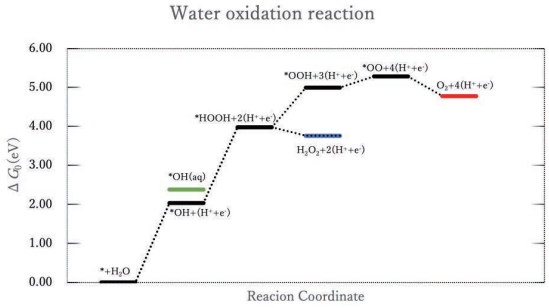


Figure 3: Energy diagram of $O_2$- and $H_2O_2$-evolution

## References

[1] Q. Wang *et. al.*: Nat. Mater. **18**, 827 (2019).

[2] Z. Pan *et. al.*: Res. Chem. Intermed. **47**, 225 (2021).

[3] M. Nakabayashi, K. Nishiguchi *et. al.*: J. Phys. Chem. C (in press: https://doi.org/10.1021/acs.jpcc.3c00820).

[4] M. Cococcioni *et. al.*: Phys. Rev. B **71**, 035105 (2005).

[5] T. Takata *et. al.*: Nature **581**, 413 (2020).

# Development of Thermal Functional Materials Based on First-principles Simulations

Wenyang DING[1], and Junichiro SHIOMI[1,2]

*1. Department of Mechanical Engineering, The University of Tokyo, Japan*

*2. Institute of Engineering Innovation, The University of Tokyo, Japan*

Manipulating thermal conductivity of crystalline materials by phonon engineering has attracted tremendous attention. Van der Waals (vdW) heterostructures are an ideal candidate to realize low thermal conductivity in their through-thickness direction due to its weak interlayer interactions and prominent disorder by alternating stacking orders.[1] However, previous studies have not been able to characterize phonon propagation thought vdW heterostructures in mode-wise fashion, which has limited the understanding and engineering of the heat conduction. Herein, for the first time, heat conduction in vdW heterostructures are resolved to the level of individual phonon polarizations, whose incident angles are utilized to elucidate the role that phonon interference and phonon tunneling play in vdW heterostructures.

First, we searched for vdW graphene-$WS_2$ heterostructure with the ultralow thermal conductivity by combining Bayesian optimization and non-equilibrium molecular dynamics (NEMD) including all the orders of anharmonicity. It is found that the lowest thermal conductivity of optimized heterostructure is 0.04 W/m-K, only 5% of graphite thermal conductivity and 13% of pristine $WS_2$ thermal conductivity (Fig. 1). Interestingly, the thermal conductivity of optimized heterostructure possesses only half of the thermal conductivity of the corresponding periodic superlattice. Moreover, the lattice thermal conductivity of pristine $WS_2$, pristine graphite, periodic superlattice, and the optimized heterostructure are also calculated by utilizing mode-resolved atomistic Green's function (AGF) method. Since AGF only considers harmonic interatomic force constants, it serves to probe the characteristics of elastic phonon scattering whose influence on thermal conductivity is partial but significant as can be seen in the comparison with NEMD results (Fig. 1). To further study the characteristics of elastic phonon scattering, the mode-resovled phonon transmissions are calculated using the S-matrix analysis.[2]

## References

(1) Liu, Y.; Weiss, N. O.; Duan, X.; Cheng, H.-C.; Huang, Y.; Duan, X. Van der Waals heterostructures and devices. *Nature Reviews Materials* **2016**, *1* (9), 16042.

(2) Ong, Z.-Y. Atomistic S-matrix method for numerical simulation of phonon reflection, transmission, and boundary scattering. *Physical Review B* **2018**, *98* (19), 195301.

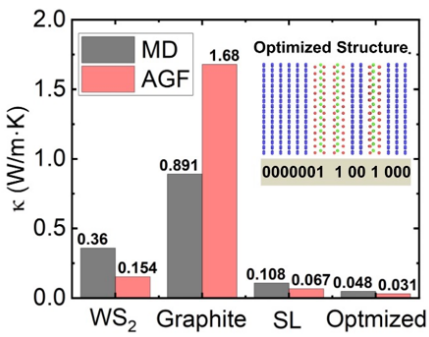


Fig. 1 Comparison of the thermal conductivity of difference. structures and methods.

# First-principles study of energy and spintronics materials

Fumiyuki ISHII, Naoya YAMAGUCHI, Rifky SYARIATI,
Hikaru SAWAHATA, Hana Pratiwi KADARISMAN, Kaiki SHIBATA,
Yaotang ZHANG, Vierta SARASWATI, Takahiro TOMINAGA,
Yedija Yusua Sibuea TEWENG, Juhri HENDRAWAN,
Yume MORISHIMA, Khusnul YAKIN, Wardah AMALIA,
Syifa Fauzia Hariyanti PUTURI, Ahmad GHIFFARI, Salsabila Amanda PUTRI
*Nanomaterials Research Institute, Kanazawa University*
*Kanazawa, 920-1192, Japan*

1. *$MnBi_2Te_4$ van der Waals layers*[1]

The transverse thermoelectric effect, which produces an electric field in the direction of the cross product of the temperature gradient and magnetization of magnetic materials, has attracted much attention in recent years because of its potential applicability to a large area. Since $MnBi_2Te_4$ was predicted to have antiferromagnetic order in the interlayer and to be a ferrimagnetic semiconductor with quantized anomalous Hall conductivity in an odd number of three or more septuple layers, it is expected to generate a transverse thermoelectric effect. We have performed first-principles calculations by using OpenMX code[2] for ultrathin $MnBi_2Te_4$ films and estimating the coefficient representing the magnitude of the transverse thermoelectric effect. The anomalous Hall and Nernst effect were calculated by using our developed efficient methods by local Berry phase in momentum space[3]. A large enhancement in transverse thermoelectric effect, anomalous Nernst coefficient, larger than $20\mu$V/K, was obtained by the Seebeck term for a wide range of carrier concentrations. The present results motivate further studies on the anomalous Nernst effect in intrinsically or doped magnetic semiconductors.

2. *Hapkeite $Fe_2Si$*[4]

In order to obtain a guideline for exploring new inexpensive and high-performance thermoelectric materials, the first-principles calculations were performed to clarify the thermoelectric properties of Fe-Si alloys, which are the most abundant iron-based compounds. As a result, we obtained a large transverse thermoelectric transport coefficient $\alpha_{xy}$ of 2.06 A/mK for the model crystal structure of a mineral Hapkeite $Fe_2Si$ contained in a meteorite Dhofar 280, which is believed to originate from the Moon. Calculated results show that the model structure, Hapkite $Fe_2Si$, exhibits a more significant transverse thermoelectric transport coefficient than bcc-Fe and hexagonal $Fe_2Si$. Detailed analysis of the electronic states and transport coefficients indicates that the significant transverse thermoelectric effect is due to an anomaly in the density of states (DOS) at the interface between the Fe layer and the Si-Fe alternating layer. The band-edge type van Hove singularity contributed to the DOS at the Fermi level. Several previous studies have attempted to generate transverse thermoelectric effect through multi-layered structures with each layer on the order of 1 nm scale. A similar interfacial effect that enhances the transverse thermoelectric ef-

fect may be observed. Therefore, this finding is promising for the design of new transverse thermoelectric materials.

3. *Persistent spin helix in diamond*[5]
Density functional theory (DFT) simulations were performed to investigate the diamond (111) surface. We investigated how different terminations such as hydroxyl (OH) and hydrogen (H) affect the strength of the spin-orbit coupling on the diamond surface and the spin structure in momentum space. The calculation results reveal that the OH-terminated state contributes to the valence band maximum (VBM), while the H-terminated state contributes to the conduction band minimum (CBM). Due to the OH termination, persistent spin helix spintexture is obtained and the spin-orbit coupling coefficient is found to be 14.2 meV·Å at the valence band maximum (VBM). This is significant compared to the ZnO($10\bar{1}0$) surface and slightly larger than various n-type sphalerite quantum wells. Moreover, it is larger than the 3.6 meV·Å resulting from the hydrogen termination of diamond. Due to the large spin-orbit coupling coefficient, the wavelength of persistent spin helix is shortened, and miniaturization of spin field effect transistors can be expected.

4. *The Rashba effect of PbS/Au(111)*
We have performed the first-principles calculation of the PbS(111) which has buckled honeycomb structure on the Au(111) surfaces. The broken inversion symmetry due to the buckling of the system shifted the energy and caused the Rashba effect. The orientation or contact at the interface highly controls the Rashba effect at heterostructures. For the metal-metal contact, Pb-Au, allows the Rashba effect at the interface, while metal-insulator contact, S-Au, does not. The PbS(111) can be used to generate the Rashba effect surface state of thin noble metals.

# References

[1] Y. Morishima, N. Yamaguchi, H. Sawahata, and F. Ishii, Appl. Phys. Express, **16** 043003 (2023).

[2] H. Sawahata, N. Yamaguchi, S. Minami, and F. Ishii, Phys. Rev. B **107**, 024404 (2023).

[3] T. Ozaki *et al.*, http://www.openmx-square.org/

[4] T. Tominaga N. Yamaguchi, H. Sawahata, and F. Ishii, Jpn. J. Appl. Phys. **62** SD1019(2023).

[5] H.P. Kadarisman, N. Yamaguchi, and F. Ishii, Appl. Phys. Express, **16** 023001(2023).

# First Principles Studies on Spin Tranfer Torque Magnetic Randum Access Memory (STT-MRAM)

Kenji SHIRAISHI

*Institute for Materials and Systems for Sustainability,*

*Nagoya University, Furo-cho, Chikusa-ku, Nagoya, 464-8601*

Spin-transfer torque magnetic random-access memory (STT-MRAM) is expected to be a non-volatile memory that replaces SRAM and DRAM currently in use. MgO layer in CoFeB/MgO/CoFeB MTJ consists of irregularly shaped grains with a diameter of 10 to 15 nm, and the presence of mainly the Σ5 (210) [001] grain boundaries was observed at the interface between the grains. iPMA is generally known to be sensitive to the cleanliness of the interface between the ferromagnetic layer and the insulator [1]. In this study, we focus on the grain boundary which occurred most frequently in MgO film and investigated the influence of the grain boundary for iPMA by performing the first principles calculations.

Near grain boundary (within a 4 Å range from the center line of grain boundary, the magnitude of iPMA strongly decreases. It is because the DOS peaks in the down spin channel for "|m|=1" above Fermi energy are decreased. It causes the spin orbit coupling hybridization of (|1|×|1|) changes from perpendicular magnetic anisotropy to in-plane magnetic anisotropy. In the DOS peaks in the down spin channel above Fermi energy in ideal model, the wave functions mainly form the bonding orbitals between interfacial Fe atoms and second layer Fe atoms. Near grain boundary, the in-plane symmetry is broken by the grain boundary and the hybridization between interfacial Fe atoms and second layer Fe atoms weakens. It causes that the unoccupied down spin states of "|m|=1" extend above Fermi energy. We suggest that it is necessary to keep the d orbital hybridization around Fe atoms for further microfabrication.

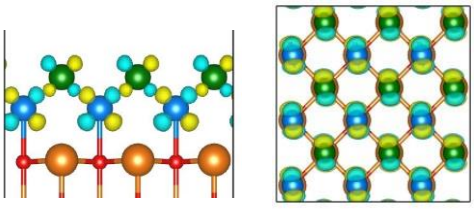

Fig.1: Wave functions at Γ point in down spin states

## References

[1] A. Hallal, H. X. Yang, B. Dieny, and M. Chshiev, Phys. Rev. B 88, (2013) 184423.

# First Principles Studies on Si-rich a-SiN for Flash Memory Application

Kenji SHIRAISHI

*Institute for Materials and Systems for Sustainability,*

*Nagoya University, Furo-cho, Chikusa-ku, Nagoya, 464-8601*

SiN is a useful material under harsh environments due to its high thermal stability and toughness against fracture, and lately utilized as passivation layer in Si solar cells. To advance our understanding of the memory function in SiN, however, the most important task never achieved so far is the determination of the thermodynamic level (TD) induced by $V_N$. This TD level is responsible for the electron capture and emission and its determination involves assessment of roles of hybridization, spin polarization and ionicity of $V_N$ in SiN. We find that the appearance of this TD level is promoted by the spontaneous structural transformation near $V_N$, resulting in multiple charge states of nitrogen vacancy.

We have performed the density-functional calculations with the hybrid approximation that clarify the atomic and electronic structures of the N vacancy ($V_N$) in $Si_3N_4$. We have found that the floating state hidden in the conduction bands create a new π-like state in collaboration with the dangling-bond states around the $V_N$, (Fig.1) thus rendering the $V_N$ being multiple charge states from +1 to -5 (Fig.2). The newly found π state is unprecedented in the sense that it has the origin of the floating state distributed not around atomic sites but in the internal space of the material. The multiple charge states we have found may be utilized as an active element in information technology.

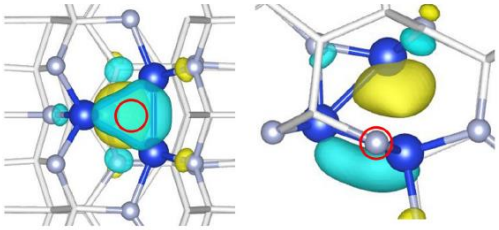

Fig.1: π-like state appeared in $V_N$ in $Si_3N_4$

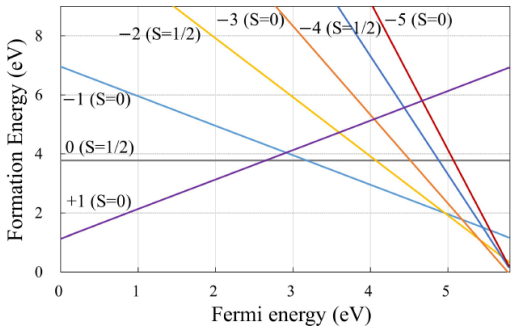


Fig.2: formation energy of $V_N$ in $Si_3N_4$.

## References

[1] F. Nanataki, K. Shiraishi, J. Iwata, Y. Matsushita, A. Oshiyama, Phys. Rev. B 88, (2013) 184423.

# Hydrogen production by water splitting on $CeO_2$ (100) facet

Akira YOKO

*Advanced Institute for Materials Research,*

*Tohoku University, Katahira 2-1-1,Aoba-ku, Sendai, Miyagi 980-8577*

$CeO_2$ nanocubes with (100) facet have been synthesized by supercritical method, and it was found to have high oxygen storage capacity. In this study, the redox property of the (100) facet was studied by using first-principles calculations.

In this study, first principles simulations based on density functional theory (DFT) was conducted. Plane wave basis DFT simulations were conducted using VASP code. Structures of $CeO_2$ at surface and bulk were calculated with generalized gradient approximation proposed by Perdew, Burke, and Ernzerhof (PBE) [1]. The valence configurations of the pseudopotentials were $5s^2 5p^6 4f^1 5d^1 6s^2$ for Ce and $2s^2 2p^6$ for O. The DFT+U method introduced by Dudarev et al. [2] was used to treat electron localization. The parameter U-J was set to 5.0 eV for Ce4f and 5.5 eV for O2p states, respectively, based on previous studies of $CeO_2$ [3]. The Monkhorst-Pack k-point mesh of 4×4×4 was used for the unit cell of $CeO_2$. The slab model exposing (100) facet includes 60 atoms, and that for (111) facet includes 108 atoms. The Monkhorst -Pack k-point mesh for the slab model was 4×4×1.

Figure 1(a) and 1(b) show $CeO_2$ (100) bare surface and hydroxylated surface, respectively. For the (100) facet model, half of the oxygen was moved to the other side to exclude polarity keeping the $CeO_2$ composition. When $CeO_2$ is fully hydroxylated by water adsorption and dissociation, the surface state is changed as Figure 1(b). Interestingly, the lattice expansion observed inside of the bare surface model (Fig. 1(a)) was relaxed with surface hydroxylation owing to the surface stabilization.

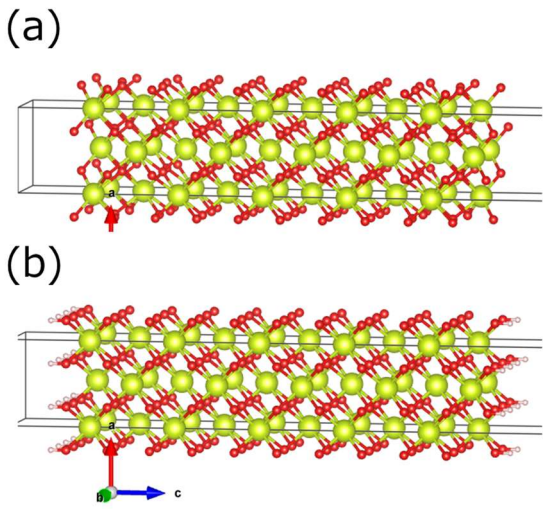


Fig. 1: $CeO_2$ (100) bare surface and hydroxylated (100) surface.

## References

[1] J.P. Perdew, K. Burke, M. Ernzerhof, Phys. Rev. Lett., 77 (1996), p. 38650. [2] S. Dudarev, G. Botton, S. Savrasov, C. Humphreys, A. Sutton, Phys. Rev. B, 57 (1998), p. 1505. [3] P.R. Keating, D.O. Scanlon, B.J. Morgan, N.M. Galea, G.W. Watson, J. Phys. Chem. C, 116 (2012), pp. 2443-2452

# Electronic structure analysis of $SiC/SiO_2$ interface under gated electric field

Yu-ichiro MATSUSHITA

*Laboratory for Materials and Structures, Institute of Innovative Research, Tokyo Institute of Technology, Ookayama, Meguro-ku, Tokyo 152-8552*

SiC-MOS devices have attracted much attention as next-generation power devices due to their excellent characteristics. However, the device characteristics are at most 10% of the theoretical performance value of SiC, which is thought to be due to high-density interface defects. However, we have proposed a new type of mechanism for the generation of interfacial levels, which originates from the peculiarity of the wave function at the lower end of the conduction band of SiC.

In this study, we have performed a comparative study of the electronic structure of the $SiC/SiO_2$ interfaces under a gated electric field by means of theoretical calculations based on density functional theory, including the dependence of the electronic structure on the plane orientation. It is found [1] that the wavefunction at the conduction band minimum (CBM) at the $SiC(0001)/SiO_2$ interface tends to be localized at the cubic site closest to the interface. On the other hand, we found that such localization of the wavefunction cannot be observed on nonpolar interfaces such as the (11-20) plane. We found that this is related to the structural channel near the interface. Of particular importance, the localization of the wavefunction at this (0001) interface is distributed much closer to the interface (<5 Å) than expected from the effective mass approximation (EMA), and thus is expected to be more sensitively scattered by interface defects. This result may explain why the channel mobility of the (0001) plane is particularly low compared to the other planes (e.g., (1120)), which is well known from experiments.

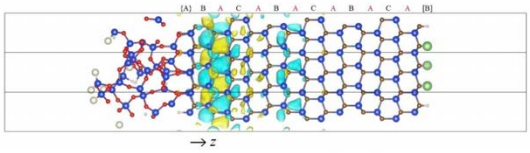


FIG 1. Isosurface at 38% of the peak value of wavefunction localized at outermost cubic site (F = 1.0 MV/cm, CBM). The blue, brown, red, and small white balls depict Si, C, O, and H atoms, respectively.

We have also clarified that the

deviation from the EMA, which is a frequently used method to analyze the electronic structures in semiconducting devices, is attributed to the long structural periodicity along the [0001] direction in the SiC crystals.

Furthermore, in actual SiC-MOS interfaces, the introduction of nitrogen is used to improve the interface properties. However, its microscopic mechanism has not been elucidated. In addition, considering the recent experimental results that the introduced nitrogen also diffuses to the SiC side. We study how the electronic states at the SiC / SiO2 interface are affected when nitrogen is introduced as a dopant based on first-principles calculations. As a result, we found that the deep doping of nitrogen relaxes the confinement potential near the interface and the localization of the wavefunction, which is expected to improve the device properties. We succeeded in proposing a new way to improve SiC-MOS devices.

Fig. 1: Supercomputer System B at SCC-ISSP.

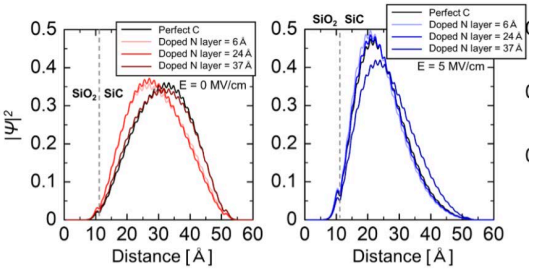


FIG 2. Local density of states (LDOS) of the CBM in slabs with di↵erent N-doped regions. For clarity, averaging was done over the atomic layer thickness period. Applied electric fields are 0, 5, and 10 MV/cm, respectively.

## References

[1] K. Tachiki, Y. Nishiya, J.-I. Iwata, and Y. Matsushita, arXiv:2303.08527 (2023).

[2] H. Yoshioka, J.-I. Iwata, and Y. Matsushita, arXiv:2303.05085 (2023).

# Density functional theory study of adsorption and reaction of molecules on metal surfaces

Ikutaro Hamada

*Department of Engineering, Graduate School of Engineering,*

*Osaka University, 2-1 Yamada-Oka, Suita, Osaka 565-0871*

Graphene doped with foreign elements has attracted enormous attention because of emergent electronic properties, besides its own unique structural, electronic, and mechanical properties, as well as its stack(s) with the same and/or different two-dimensional materials.

Graphene doped with nitrogen has been shown to exhibit catalytic activity toward electrochemical oxygen reduction reaction (ORR). To understand the mechanism of ORR on nitrogen-doped graphene, it is important to understand the interaction between graphene and water, a common solvent in electrochemistry. However, density functional theory with the conventional semilocal approximation fails to describe the weak water-graphene interaction accurately. In this work [1], we use rev-vdW-DF2 [2], one of the van der Waals density functionals, which has been shown to be able to describe the water-graphene interaction accurately [3], to study the interaction between water molecule and nitrogen-doped graphene. We consider different water orientations and different nitrogen configurations and obtain the preferred orientations of the water molecule, depending on the nitrogen configuration. We reveal that graphitic and pyridinic nitrogen atoms are charged positively and negatively respectively, which lead to different water orientations. The interaction energy curves obtained in this work may serve as references for future studies and be useful for modeling of graphene/water interfaces with hybrid quantum-mechanics/molecular mechanics-type methods.

Nitrogen-doped graphene with a single transition metal atom (single atom catalyst, SAC) has also been attracted much attention as it shows ORR activity comparable to platinum, and there have been numerous studies both experimentally and theoretically. However, the mechanism of ORR on SAC is not yet fully resolved. In this study [4], we focus on the exchange-correlation functional to be used to study ORR on SAC, in particular Fe and Co SAC embedded in a nitrogen-doped graphene (Fe/Co-$N_4$-C). By choosing the results obtained using the Bayesian error estimate functional with van der Waals correlation (BEEF-vdW) [5] as references, we perform systematical calculations of the ORR intermediates on Fe-$N_4$-C and Co-$N_4$-C using commonly used semilocal exchange-correlation functionals with and without dispersion correction and find that revised Perdew-Burke-Ernzerhof (RPBE) [6,7] functional with Grimme's dispersion correction [8] (RPBE-D3) gives the results consistent with those obtained using BEEF-vdW. The conclusion drawn in this work as well as the strategy taken there will be useful to choose an appropriate (low-cost) exchange-correlation function to study electrochemical and heterogeneous reactions.

## References

[1] A. F. Z. Abidin and I. Hamada, Phys. Rev. B **105**, 075416 (2022).

[2] I. Hamada, Phys. Rev. B **89**, 121103 (R) (2014).

[3] J. G. Brandenburg, A. Zen, D. Alfé, and A. Michaelides, J. Chem. Phys. **151**, 164702 (2019).

[4] A. F. Z. Abidin and I. Hamada, Surf. Sci. **724**, 122144 (2022).

[5] J. Wellendorff, *et al*., Phys. Rev. B **85**, 235149 (2012).

[6] J. P. Perdew, K. Burke, and M. Ernzerhof, Phys. Rev. Lett. **77**, 3865 (1996).

[7] B. Hammer, L. B. Hansen, and J. K. Norskøv, Phys. Rev. B **59**, 7413 (1999).

[8] S. Grimme, J. Antony, S. Ehrlich, and H. Krieg, J. Chem. Phys. **132**, 154104 (2010).

# Theoretical determination of charge injection levels in organic semiconductor films

Ryo Uza and Susumu Yanagisawa
*Department of Physics and Earth Sciences, University of the Ryukyus*
*Senbaru 1, Nishihara Okinawa 903-0213*

Zinc phthalocyanine (ZnPc) can be used as a p-type semiconductor with hole carriers. Fluorinated zinc phthalocyanine ($F_{16}$ZnPc) can also be used as an n-type semiconductor. ZnPc and $F_{16}$ZnPc are attracting attention as organic solar cell materials. Fundamental understanding on the formation mechanism of charge injection levels is urgent for their practical application. In the present work, Vienna Ab-initio Simulation Package (VASP) was used to determine from first-principles the lattice parameters of the crystals and the atomistic structure of molecular films by the van der Waals (vdW) density functional[1]. Subsequently, the band energy calculations were performed with the GW approximation, which included the effects of electronic polarization. The ionization potential ($I$) or electron affinity ($A$) of any molecule depends on the electronic polarization of the surrounding molecules and the electrostatic interactions upon the ionized molecule from its surroundings[2]. The effect induced by the molecules surrounding an ionized molecule, which stabilizes the charge injected into the molecule by the polarization clouds with an opposite charge, is called electronic polarization. In this work, both the effects of the electrostatic interaction and the electronic polarization were included in the calculations to quantitatively predict the level of charge injection.

The result indicates that in case of ZnPc thin film the energy levels are relatively shifted up in the standing configuration and shifted down in the lying configuration. This comes from the electric quadrupole moment of the neutral molecule. Electric quadrupoles generate electrostatic potentials in crystals and films. The generated electrostatic potential is governed by the electric quadrupole tensor and depends on the distance between molecules and the orientation angle of the constituent molecule. Therefore, the shift is opposite for the standing and lying configurations, as the orientation angle of the molecules relative to the nearest neighbor molecules changes and the sign of the electrostatic potential is different. Similarly, given the opposite signs of the $zz$ component of the electric quadrupole tensor, the signs of the electrostatic potential for ZnPc and $F_{16}$ZnPc are opposite.

The effect of electronic polarization was determined using the GW approximation to calculate $I$ and $A$, and the density of states was obtained by matching the corresponding energy levels to the peak of the density of states. It was found that the positions of the density of states peaks are in good agreement with the experimental photoelectron/inverse photoelectron spectra[3] (Fig. 1). The calculated energy gap is slightly shallower than the experimental results, which can be corrected by improving the accuracy of the GW approximation.

Overall, it is concluded that the present theoretical method is of practical use in predicting the frontier energy levels of organic semiconductor thin film. Prediction of the charge injection levels in mixed films of ZnPc and

$F_{16}$ZnPc is in progress.

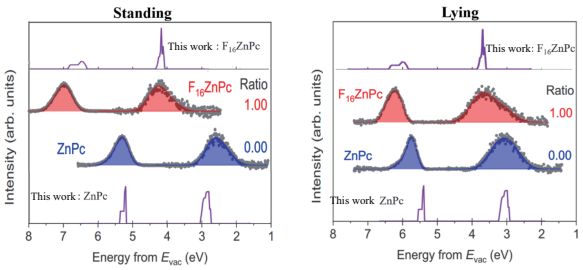


Figure 1: Theoretical density of states (DOS) of ZnPc and $F_{16}$ZnPc thin films with standing and lying configurations. The experimental DOS measured with direct/inverse photoemission[3] are also displayed.

## References

[1] I. Hamada: Phys. Rev. B **89**, 121103 (2014).

[2] K. Yamada, S. Yanagisawa, T. Koganezwa, K. Mase, N. Sato, and H. Yoshida: Phys. Rev. B **97**, 245206 (2018).

[3] Y. Uemura, S. A. Abd-Rahman, S. Yanagisawa, and H. Yoshida: Phys. Rev. B **102**, 125302 (2020).

# Reduction of Rare Metals in Fuel Cell and Formic Acid Decomposition Catalysts

Norihito Sakaguchi

*Center for Advanced Research of Energy and Materials, Faculty of Engineering, Hokkaido University, Sapporo, Hokkaido 060-8628*

We investigated the adsorption and diffusion properties of single-atom catalysts on light-element doped graphene supported on the metal substrates, with the aid of the first-principles calculation based on the density functional theory (DFT). We also investigated the catalytic activities of the considered systems in oxygen reduction and formic acid decomposition reactions.

At first, we investigated the stabilities of single Pt and Cu atoms on light-element doped graphene supported on the metal substrates. We considered Fe, Ni, and Cu as metal substrates. We performed the total energy and electronic structure calculations using The Vienna Ab initio Simulation Package (VASP). We installed a parallelized VASP with Intel® MPI Library and Intel® Math Kernel Library. We have reported that the adsorption of Pt and Cu atoms on light-element doped graphene with flat structures became stronger through supporting the magnetic substrates, i.e., Fe and Ni substrates, last year. We reinvestigated the adsorption properties of Pt and Cu atoms on light-element doped graphene with flat structures on non-magnetic substrates, i.e., Cu substrates. We revealed that the ferromagnetic electronic structures of metal substrates are not required to enhance the chemical bonding between single-atom catalysts and light-element doped graphene light-element doped graphene. In most cases of steric light-element doped graphene, the non-magnetic substrates also weaken the Pt and Cu adsorption and enhance the catalyst diffusion on the light-element doped graphene in the same way as the magnetic substrates.

Based on the previously reported volcano plots, we also investigated the catalytic activities of the considered systems in oxygen reduction and formic acid decomposition reactions from the adsorption energies of the components of the reactants. Although the strong chemical bonds between catalysts and supports are expected to lead to higher catalytic activities, the enhancements of catalytic reactions have been found only in a few systems.

## References

[1] Y. Kunisada, N. Sakaguchi, Nano Express 3 (2022) 042001.

# Development of Efficient Oxygen Storage Materials and Hydrogen Permeation Barrier Materials

Yuji Kunisada

*Center for Advanced Research of Energy and Materials, Faculty of Engineering, Hokkaido University, Sapporo, Hokkaido 060-8628*

We investigated the doping effects on the oxygen absorption/desorption properties of brownmillerite-type oxides,[1] with the aid of the first-principles calculation based on the density functional theory (DFT). We also performed O K-edge electron energy loss spectroscopy (EELS) simulations to build the EELS database for characterizing the experimental EELS spectra obtained with transmission electron microscopy. Besides, the solubility and diffusion properties of hydrogen isotopes in amorphous ceramic materials were also investigated to validate its application as hydrogen permeation barrier materials.

We investigated the oxygen absorption energies with various heteroatom substitutions in $Ca_2AlMnO_5$ using The Vienna Ab initio Simulation Package (VASP). We installed a parallelized VASP with Intel® MPI Library and Intel® Math Kernel Library. We revealed the effects of local atomic distortions induced by dopants on the oxygen absorption energies. We also performed EELS simulations of nonequivalent O atoms using Z+1 approximation to construct the database of the O K-edge EELS spectra.

We also investigated the hydrogen isotope solubility and diffusion properties in the amorphous ceramic materials. We considered $Al_2O_3$ as the hydrogen permeation membrane. We performed melt-quenching technique to obtain the amorphous structure last year. However, the obtained structures are not fully in the amorphous phase due to insufficient melting. Therefore, we obtained the atomic structures of the amorphous $Al_2O_3$ using higher melting temperatures and longer time steps for molecular dynamics simulations. Next, we performed 2000 DFT calculations with various hydrogen positions in amorphous $Al_2O_3$ to determine the relationship between the dissolution energies and the local structures. Using the Voronoi analysis, we evaluate the volume occupied by the hydrogen atoms. Finally, we revealed the dependence of the dissolution energies and diffusion barriers on the volume occupied by the hydrogen atoms.

## References

[1] K. Tanahashi, Y. Omura, H. Naya, Y. Kunisada, N. Sakaguchi, A. Kurniawan, T. Nomura, ISIJ International 62 (2022) 2578-2586.

# Densest binary/ternary sphere packings and prediction of quaternary hydrides

Ryotaro Koshoji, Masahiro Fukuda, Mutsuaki Kawamura, Taisuke Ozaki
*Institute for Solid State Physics, University of Tokyo*
*Kashiwa-no-ha, Kashiwa, Chiba 277-8581*

It was widely accepted in the 2000s that the Barlow packings such as FCC structure are the densest unary sphere packings. Despite the simpleness of the problem, it is also too difficult to identificate the densest binary sphere packings (DBSPs), however, the development of computers has been enabling us to explore the DBSPs by computer simulations. If we only explore the periodic dense packings of spheres of $n$ different sizes by computer, the packing fraction at given sphere-composition ratio is maximized by filling the space with not more than $n$ kinds of periodic packings. In 2012, Hopkins *et al.* explored the DBSPs under the restriction that the number of spheres in the unit cell with periodic boundary condition is not more than 12 and constructed the phase diagram for the first time. They also showed that in some radius and composition ratios a considerable number of the structures have competitive packing fractions, so it is necessary to optimize the packing structure precisely with small distortions.

We developed the structural optimization algorithm based on the steepest-decent method that is easy to implement. The computational cost is small and we showed that it is as precise as the Torquato-Jiao algorithm. Our algorithm, which produces initial structures as layer-by-layer stacking structures, completely revisit the previous studies with small corrections, and we successfully found the 12 putative DBSPs since the maximum number of spheres in unit cell is set to be double. As a result, a total of 28 putative DBSPs are known at the present time.

In ternary systems, the DBSPs are the candidates for the phase separations as well as the FCC packings of small, medium, and large spheres. Following our studies, we constructed the phase diagrams for the first time since previous studies on the dense ternary sphere packings (DTSPs) do not construct the phase diagrams. As a result, we totally discovered the 59 putative DTSPs [1]. One of the well-ordered DTSPs is the (13-2-1) structure shown in Fig. 1(a). The structure is the DTSP at several radius ratios such as 0.44 : 0.64 : 1.00, at which small and medium spheres are too large to be placed in the tetrahedral and octahedral sites if large spheres comprising the fcc structure contact with each other. The clathrate network of small spheres correspond to that of boron in $UB_{12}$, and the (13-2-1) structure has one additional small sphere placed in the cuboctahedron of small spheres. A medium sphere is placed in the tetrahedral site as $CaF_2$.

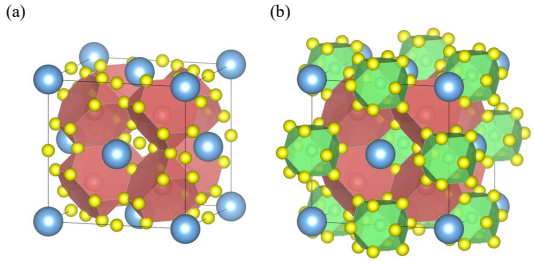


Figure 1: (a) The (13-2-1) structure. (b) The (12-1-2-1) structure.

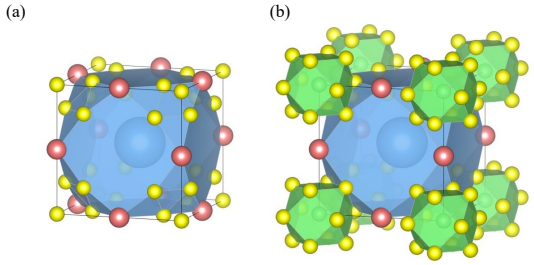


Figure 2: (a) The (13-3-1) structure. (b) The (12-1-3-1) structure.

The clathrate network has structural similarity with $LaH_{10}$ and $YH_6$. The crystal structures of

Table 1: The list of substitution atoms for spheres, where the symbol E corresponds to empty.

| sphere size | elements |
|---|---|
| small | H |
| semi-small | E, H, Li, Be, Na, Mg, Al, K, Ca, Sc, Ti, V, Cr, Mn, Fe, Co, Ni, Cu, Zn |
| medium | From Li to Hg (except for B to Ne, Si to Ar, Br, Kr, Xe, Ce to Lu, Pt) |
| large | From K to Hg (except for Br, Kr, Xe, Ce to Lu, Pt) |

the binary hydrides correspond to the DBSPs of the $XY_{10}$ and (6-1) structures, respectively. Therefore, we can expect that the (13-2-1) structure also correspond the hydrides under high pressure. However, crystal structures tend to prefer the coordination polyhedron [72]. Therefore, we replace the small sphere at the center of the cuboctahedron with metallic atoms so that the metallic atoms should be coordinated by 12 small spheres comprising a cuboctahedron. We call the quaternary structure shown in Fig. 1(b) as the (12-1-2-1) structure. This structure also has the $Fm\bar{3}m$ symmetry. We also focus on the (13-3-1) structure shown in Fig. 2(a). It is the DTSP at several radius ratios such as 0.30 : 0.40 : 1.00 and can be derived by substituting an atom at the vertex of the unit cell of the perovskite structure with a cuboctahedron of 13 small spheres. To produce the structural prototype of hydrides, we replace the small sphere at the center of the cuboctahedron with metallic atoms as shown in Fig. 2(b), and we call it as the (12-1-3-1) structure.

Table 1 shows the list of substitution atoms for spheres in the (12-1-2-1) and (12-1-3-1) structures. Small spheres are substituted with only hydrogen atoms. The number of chemical compositions for each structural prototype is 36652. To screen out unstable candidates, we execute the structural optimizations and molecular dynamic simulations with static/dynamic crystal lattices. We use the standard enthalpies of formations (SEFs) to estimate the structural stabilities. We calculate the phonon dispersions for some of hydrides which have lower SEFs and no spin polarization.

As a result, we confirm that at least 23 hydrides are dynamically stable [2]. We found that many hydrides prefer the $(12\text{-}1\text{-}2\text{-}1)_V$ structure shown in Fig. 3 to the (12-1-2-1) structure. It it worth mentioning that the $(12\text{-}1\text{-}2\text{-}1)_V$ structure is isotypic to the $Pm\bar{3}$ structure of $ScYH_6$ (cP8). Importantly, the previous study indicated that cP8-$ScYH_6$ may possess the lowest enthalpy in the pressure range of 50150 GPa. Since several quaternary hydrides

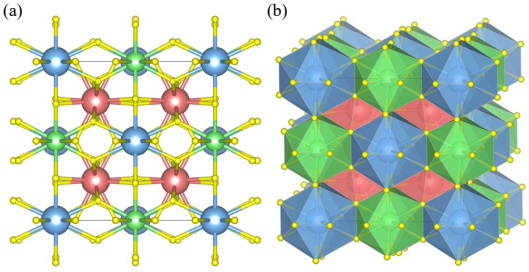


Figure 3: The $(12\text{-}1\text{-}2\text{-}1)_V$ structure.

of which we confirm the dynamic stabilities are the superstructures of cP8-$ScYH_6$, we can expect that they may also have the lowest enthalpies under higher pressures. In fact, the SEFs under 10 GPa of the four kinds of the decomposition paths from $H_{12}ScY_2Ca$:

$$ScH_2 + 2YH_2 + CaH_2 + 2H_2, \quad (1)$$
$$ScH_2 + 2YH_3 + CaH_2 + H_2, \quad (2)$$
$$ScH_3 + 2YH_2 + CaH_2 + 1.5H_2, \quad (3)$$
$$ScH_3 + 2YH_3 + CaH_2 + 0.5H_2, \quad (4)$$

are calculated, and we found that $H_{12}ScY_2Ca$ are considerably stable since it has almost the same enthalpy as the decomposition of Eqs. (1) and (3) while it is less stable than the decompositions of Eqs. (2) and (4) by about 1.2 eV/f.u., corresponding to the thermodynamic instability of 78.6 meV/atom compared to the case of Eq. (4).

Finally, we calculate the superconducting transition temperatures $T_c$ by density functional theory for superconductors, are found to be 5.7 and 6.7 K for the selected two hydrides $H_{12}ScY_2Ca$ and $H_{12}ScY_2Sr$, respectively [2].

## References

[1] R. Koshoji and T. Ozaki: J. Phys. Commun. **6**, 075002 (2022).

[2] R. Koshoji, M. Fukuda, M. Kawamura, T. Ozaki: Phys. Rev. Materials. **6**, 114802 (2022).

# Control of magnetic anisotropy by strain and electric polarization at interfaces

Yoshihiro GOHDA
*Department of Materials Science and Engineering, Tokyo Institute of Technology*
*J1-3, Nagatsuta-cho 4259, Midori-ku, Yokohama 226-8502, Japan*

Magnetocrystalline-anisotropy (MCA) energy is of importance in controlling the direction of magnetic moments. The dependence of the magnetic anisotropy on lattice constants can be utilized for magnetoelectric couplings via domain modulations of ferroelectric materials under ferromagnetic ones. Such interface multiferroicity is promising for the reduction of energy consumptions in magnetic devices avoiding the Joule heating by the electric current. The magnetoelectric effect of $Co_2FeSi$ was found to be much larger than that of $Fe_3Si$ [2], albeit its origin is yet to be clarified.

In this project, we performed first-principles calculations of ferromagnetic Heusler compounds to clarify the microscopic origin behind the strain-mediated modulation of the MCA energy $E_{\mathrm{MCA}}$. In $Co_2FeSi$, site-projected $E_{\mathrm{MCA}}$ of both Co and Fe decrease with an isotropic expansion of the in-plane lattice as shown in Fig. 1(a). This can be compared with a formulation connectable to X-ray magnetic circular dichroism observations via the quadrupole moment of the spin-density distribution (quadrupole term) and changes in orbital magnetic moments (Bruno term) [1]. As is clear from the figure, the quadrupole term is dominant for $Co_2FeSi$ corresponding to the $\uparrow\downarrow$ spin-flip term, i.e., couplings between up-spin unperturbed states and down-spin virtual states, in Fig. 1(b). In contrast, the MCA energy modulation in $Fe_3Si$ was found to be attributed to neither Bruno nor quadruple terms.

In addition, phase equilibria in permanent magnets were discussed through first-principles thermodynamics [3, 4].

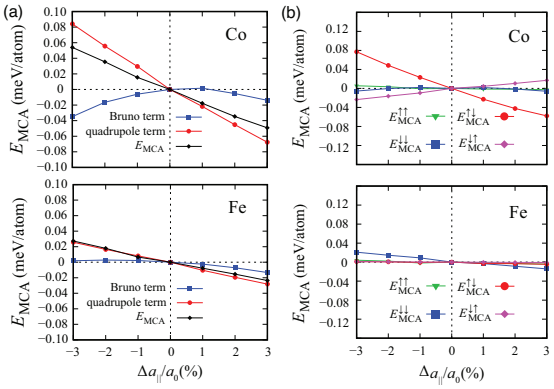


Figure 1: Site-resolved $E_{\mathrm{MCA}}$ of $Co_2FeSi$ as a function of the distortion ratio $\Delta a_{||}/a_0$: (a) total $E_{\mathrm{MCA}}$ and contributions from the Bruno and quadrupole terms; (b) $E^{\uparrow\uparrow}_{\mathrm{MCA}}$, $E^{\downarrow\downarrow}_{\mathrm{MCA}}$, $E^{\uparrow\downarrow}_{\mathrm{MCA}}$, and $E^{\downarrow\uparrow}_{\mathrm{MCA}}$

[1] J. Stöhr, J. Magn. Magn. Mater. **200**, 470 (1999).
[2] S. Fujii, Y. Gohda, *et al.*, NPG Asia Mater. **14**, 43 (2022).
[3] S. Tsuna and Y. Gohda, J. Appl. Phys. **133**, 115103 (2023).
[4] S. Nishino and Y. Gohda, Jpn. J. Appl. Phys. **62**, 030902 (2023).

# Discovery of Super-Composite Electrical Insulating Materials Based on Multiscale Physics and Deep Learning of Polymers

Hajime SHIMAKAWA, Haruto SUZUKI, Chihiro TATEYAME, Yuki MORI,
Akiko KUMADA, and Masahiro SATO
*Department of Electrical Engineering & Information Systems*
*The University of Tokyo, Hongo, Bunkyo-ku, Tokyo 113-8656*

Materials Informatics (MI), a data-driven material design method, is considered effective for designing polymer materials that require a vast amount of manufacturing information. However, although sample information including fillers and measurement conditions have a great influence on material properties, the methods for extracting them as features have not been sufficiently investigated, and the use of MI is currently limited [1]. In this study, we investigated electrical and thermal feature extraction for polymers using multi-scale physics based on first-principles and molecular dynamics calculations. We also used machine learning to predict the electrical and thermal properties of composite polymer materials. Furthermore, the importance of each material information was examined based on feature engineering.

In multiscale electrical feature computation, we successfully developed computational methods of ionic charge mobility in polymer matrix and hole trapping barrier between polymer matrix and nano-filler. In machine learning, experimental results of thermal and electrical conductivity of the composite materials in PoLyInfo [2] were used. The thermal and electrical conductivities were learned by adding polymer information, filler information, volume fraction, measurement temperature, sample thickness, and process conditions, and the prediction accuracy improved with each additional feature. The prediction accuracy increased significantly when filler information was added for thermal conductivity, and when process information was added for electrical conductivity. While filler volume fraction had a significant effect on prediction of thermal conductivity, it was not sufficient for prediction of electrical conductivity, indicating that input of process conditions is necessary in predicting electrical conductivity. Our results show a new potential of materials informatics for the prediction of complex polymer properties.

## References

[1] L. Chen, et al.: Mater. Sci. Eng. R Rep., 144, 100595 (2021)
[2] https://polymer.nims.go.jp/en/

# First-principles study of photoresponsive functional materials

Shinji TSUNEYUKI

*Department of Physics, The University of Tokyo*

*Hongo, Bunkyo-ku, Tokyo 113-0033*

The technology to connect and control semiconductor or magnetic devices with light is attracting attention as an essential technology in the era of 5G and beyond 5G. The development of materials and devices necessary for this purpose is required. This research aims to develop and demonstrate a first-principles simulation method for the optical responsivity of materials, which will serve as a basis for such research and development.

This academic year, we developed a first-principles method to calculate the dielectric properties of crystals with significant anharmonic effect in phonon in the sub-THz to THz range and applied the technique to rutile $TiO_2$ [1].

The method is based on Cowley's lattice dynamics theory on dielectric properties [2]. We calculate the Born effective charges of ions from the Berry phase and employ the modified self-consistent phonon approach to calculate phonon frequencies and linewidths, including third and fourth-order anharmonicity.

We find that the optical phonon frequencies and line widths at the gamma point better agree with experimental measurements than those obtained by the perturbative approach (Fig.1). We also find that the four-phonon scattering process contributes as much to the phonon linewidths of some phonon modes as the third-order anharmonic term. This method is versatile and relatively computationally inexpensive, and will be useful for future development of dielectric materials.

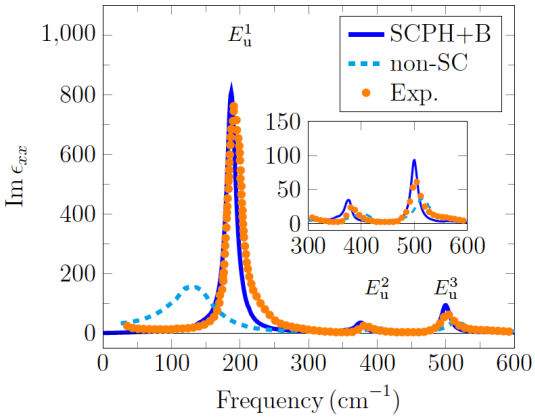


Fig.1 The imaginary part of the dielectric function $\varepsilon_{xx}$. The results of the present method and a perturbative approach are show in a solid line and a dashed line, respectively (from Ref. [1]).

## References

[1] T. Amano, T. Yamazaki, R. Akashi, T. Tadano and S. Tsuneyuki, Phys. Rev. B, 107, 094305 (2023).

[2] R. Cowley, Adv. Phy. 12, 421 (1963).

# Analyses on electronic and magnetic structure and parallelization development in quasi-particle self-consistent *GW* code

Tatsuki ODA[1,2], Kazuki MURANAKA[2], Chandro PARDEDE[2], Jakub LUTSINEC[2], Ko HYODO[2], Masao OBATA[1,2]

[1]*Institute of Science and Engineering, Kanazawa University, Kanazawa, Ishikawa 920-1192*

[2]*Graduate School of Natural Science and Technology, Kanazawa University, Kanazawa, Ishikawa, 920-1192*

We have studied electronic structure in several systems of magnetic material. In one of the investigations, we found new foundations of magnetic shape memory alloy on the electronic instability to modulated phases using the quasi-particles self-consistent GW method (QSGW) in which the electron-correlation of random phase approximation is explicitly included in the self-energy part of one particle energy level. This method was used in the software *ecalj* [1] which has been developed by the researcher T. Kotani. Our group has developed its highly parallelized code, achieving a one-order faster using the computer facilitated in ISSP. We have also developed the density functional theory (DFT) code optimized for GPU architecture.

(A) Application to $Ni_2MnGa$ by QSGW method

According to the QSGW approach, the Ni $e_g$ orbitals in the cubic (austenite) phase, which lead to martensite phase transition by band Jahn-Teller effect, were found to locate just on the Fermi level. This implies a clear definitive origin of band Jahn-Teller (JT) effect in comparison with the results obtained by the density functional approach of generalized gradient approximation (GGA). From the analysis of generalized susceptibility in the cubic phase, the instabilities responsible for the modulated structures of 10M, 14M, and 6M were found to be an intrinsic property in the electronic states [2]. These states may stabilize the modulated one, accompanied by tetragonal local JT distortions. Their property of Fermi surface nesting sensitively depends on a subtle change in the magnetic moment, corresponding to the experimental fact that the modulated structure appears depending on temperature and the composition of the magnetic element. We also found that there is another secondary peak in the generalized susceptibility.

The results of QSGW show a lot of improved features in the electronic structure. The Ni 3d $e_g$ component, appearing just at the Fermi level, can be definitive theoretical evidence for the existence of phase instability at low temperatures. Compared with the GGA +U or GGA results, the eigenvalue levels of the minority spin state shift to higher energies,

indicating an increase in exchange splitting and, thus, an increasing total magnetic moment. The energy level shift in the minority spin state is small but makes a drastic change in the generalized susceptibility. The change is quantitative, but the meaning of its result provides a qualitative conclusion in the martensite phase of 10M or 14M appearing at low temperatures. Such an instability indicated from the investigation of susceptibility is found to be much more sensitive to the magnetic moment, implying a close relationship with the composition of the magnetic element and the external magnetic field.

(B) Optimization of DFT code for GPU

The use of GPU parallelization has shown a great promise in accelerating DFT calculations and reducing the computational cost. The results obtained from our GPU-accelerated DFT code demonstrate its potential to accelerate electronic structure calculations, making it a promising tool for studying large-scale systems in materials science, physics, and chemistry.

Several of the subprogram in the DFT code need a lot of memory data for accomplishing their operations. In a plane-wave-basis code, the routines of fast Fourier transformation (FFT) and matrix-matrix multiplication (MMM) are essential in the total computational cost. The problem has been a large amount of data transfer between GPU and CPU. Such problem may be resolved in our plane wave code with a currently available GPU equipped at ISSP computer.

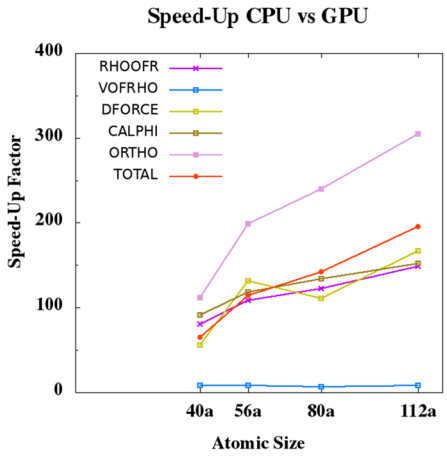


Fig. 1: Time ratio of GPU vs. CPU.

We combined the use of OpenACC programming and CUDA library that provides the routines of FFT and MMM. The OpenACC can manage data transfer from host to device and vice versa easily and parallelize some kinds of calculations with simple directive. We performed DFT calculations on the different system size; modulated magnetic shape memory alloy $Ni_2MnGa$ (NMG); $(NMG)_{10}$(40 atoms), $(NMG)_{20}$(80 atoms), $(NMG)_{14}$(56 atoms), $(NMG)_{28}$(112 atoms). Our code gained speed-up 65-195-fold depending on its system size. However, we faced memory limitation due to memory capacity on the GPU. As the larger system we calculate, the large memory capacity we need to perform the calculation.

**References**

[1] T. Kotani, J. Phys. Soc. Jpn. **83**, 094711 (2014); *ecalj*: https://github.com/tkotani/ecalj/.

[2] M. Obata, T. Kotani, and T. Oda, Phys. Rev. Mater. **7**, 024413 (2023).

# Systematic elucidation of structure and electronic state of π-electron-proton coupled molecular conductors under pressure

Shun DEKURA†

*Institute for Solid State Physics, The University of Tokyo,*
*Kashiwanoha 5-1-5, Kashiwa, Chiba 277-8581*

κ-$H_3$(Cat-EDT-TTF)$_2$ (= H-TTF) and its analogues, which have been recently developed in our group, show unique π-electron–proton coupled physical properties owing to the strongly correlated electrons and dynamics of protons in the H-bonds: such as quantum spin liquid / quantum paraelectric states or charge ordering transition coupled to the dynamics of protons.[1–4] Although H-TTF shows charge ordering with proton localization under hydrostatic pressure, it was very recently found that S/Se substituted H-TTF analogue, H-ST, shows metallization and superconducting transition under hydrostatic pressure, and shows metal–insulator transition under uniaxial pressure. To understand the π-electron–proton coupled physical properties of H-ST under physical pressure, in this study, the author performed first-principles structural optimization of H-ST under hydrostatic and uniaxial pressure, using OpenMX software (Ver. 3.9) on the ISSP Supercomputer System B (ohtaka), using GGA-PBE exchange-correlation functional.

Structural optimizations were performed by minimizing the enthalpy under hydrostatic or uniaxial pressures up to 2.0 GPa. The optimized structures under hydrostatic pressures did not show proton localization up to 2.0 GPa. On the other hand, the optimized structures under uniaxial pressures showed proton localization below 2.0 GPa. The results are consistent with the experimentally observed behavior, and suggests that isotropy of the applied pressure, in addition to the band width increase, is key to cause metallization in H-ST. However, structural optimization of H-TTF under hydrostatic pressure did not result in proton localization unlike the experimental observation, which indicates the importance of quantum nature of protons to fully understand the behavior of H-TTF analogues under pressure.

## References

1) H. Mori, S. Yokomori, S. Dekura, and A. Ueda, Chem. Commun. **58**, 5668 (2022).
2) A. Ueda, S. Yamada, T. Isono, H. Kamo, A. Nakao, R. Kumai, H. Nakao, Y. Murakami, K. Yamamoto, Y. Nishio, and H. Mori, J. Am. Chem. Soc. **136**, 12184 (2014).
3) A. Ueda, K. Kishimoto, T. Isono, S. Yamada, H. Kamo, K. Kobayashi, R. Kumai, Y. Murakami, J. Gouchi, Y. Uwatoko, Y. Nishio, and H. Mori, RSC Adv. **9**, 18353 (2019).
4) M. Shimozawa, K. Hashimoto, A. Ueda, Y. Suzuki, K. Sugii, S. Yamada, Y. Imai, R. Kobayashi, K. Itoh, S. Iguchi, M. Naka, S. Ishihara, H. Mori, T. Sasaki, and M. Yamashita, Nat. Commun. **8**, 1821 (2017).

†Current address: Institute of Multidisciplinary Research for Advanced Materials (IMRAM), Tohoku University, 2-1-1 Katahira, Aoba-ku, Sendai 980-8577

# Elucidation of the mechanism of fast proton conduction based on proton tautomerism in molecular crystals by using first-principles calculations

Shun DEKURA†

*Institute for Solid State Physics, The University of Tokyo,*

*Kashiwanoha 5-1-5, Kashiwa, Chiba 277-8581*

The author has been developing anhydrous superprotonic conductors based on single-crystalline molecular solids, and elucidating their peculiar conduction mechanism involving molecular internal degrees of freedom.[1–4] In this study, we elucidated the mechanism of anhydrous superprotonic conduction ($\sigma > 10^{-3}$ S/cm) with the low activation energy ($E_a$) of ca. 1.0 eV based on proton tautomerism in 1,2,3-triazolium phosphate. To evaluate the activation energies accompanied with the proton conduction in the crystal structure, first-principles NEB calculations were performed using OpenMX software (Ver. 3.9) on the ISSP Supercomputer System B (ohtaka), using a generalized gradient approximation (GGA) proposed by Perdew, Burke, and Ernzerhof to the exchange-correlation functional.

At first, the experimentally obtained X-ray structure was optimized fixing the unit-cell geometry for the initial state, where all the four 1,2,3-triazolium in the unit cell are 1*H*,3*H*-tautomer. Then, the structure with one 2*H*,3*H*-tautomer out of four 1,2,3-triazolium in the unit cell was optimized as final state. The NEB calculation for this step suggested that this tautomerization occurs via hydrogen-bond formation with transient proton transfer to phosphate in the adjacent layer. The corresponding $E_a$ was ca. 1.2 eV, consistent with the experimentally observed one. The result strongly supports the low-barrier anhydrous proton conduction realized by proton tautomerism. However, only one step of whole proton conduction process has been elucidated in this research; the other processes are now under consideration.

## References

1) Y. Sunairi, S. Dekura, A. Ueda, T. Ida, M. Mizuno, and H. Mori, J. Phys. Soc. Jpn. **89**, 051008 (2020).

2) S. Dekura, Y. Sunairi, K. Okamoto, F. Takeiri, G. Kobayashi, Y. Hori, Y. Shigeta, and H. Mori, Solid State Ionics **372**, 115775 (2021).

3) Y. Hori, S. Dekura, Y. Sunairi, T. Ida, M. Mizuno, H. Mori, and Y. Shigeta, J. Phys. Chem. Lett. **12**, 5390 (2021).

4) S. Dekura, M. Mizuno, and H. Mori, Angew. Chem. Int. Ed. **61**, e202212872 (2022).

†Current address: Institute of Multidisciplinary Research for Advanced Materials (IMRAM), Tohoku University, 2-1-1 Katahira, Aoba-ku, Sendai 980-8577

# First-principles calculations of electron correlation parameters to elucidate π-electron–proton coupled physical properties of the unconventional molecular conductors Cat-TTF analogues

Shun DEKURA†

*Institute for Solid State Physics, The University of Tokyo,*
*Kashiwanoha 5-1-5, Kashiwa, Chiba 277-8581*

κ-$H_3$(Cat-EDT-TTF)$_2$ (= H-TTF) and its analogues, which have been recently developed in our group, show unique π-electron–proton coupled physical properties owing to the strongly correlated electrons and dynamics of protons in the H-bonds.[1)] In particular, a charge-ordering (CO) phase transition coupled to the localization of D in H-bonds occurs in H/D isotope substituted analogue.[2)] The CO transition temperature varies upon the S/Se substitution in the π-electron framework and the application of physical pressure;[3,4)] however, the mechanism had not been revealed. In this study, to investigate the impact of electron correlation on the π-electron–proton coupled CO transition, the author evaluated the bandwidth *W*, on-site Coulomb repulsion *U*, and inter-site Coulomb repulsion *V* of the H-TTF analogues by first-principles DFT calculations based on the experimental X-ray structures.

All the calculations were performed on the ISSP Supercomputer System B (ohtaka). The electronic band structures were calculated by using Quantum Espresso (version 6.8), where the half-filled HOMO–HOMO antibonding band crosses the Fermi level. The maximally localized Wannier functions (MLWFs) with the shapes consistent with HOMO–HOMO antibonding orbitals were successfully obtained from the band crossing the Fermi level using RESPACK software. Then, *U* and *V* for each analogue were evaluated by the screened direct integrals between two MLWFs in the crystals. Based on the comparison of the obtained electronic parameters and CO transition temperature ($T_{CO}$), *W* and *V* were found to be correlated with $T_{CO}$. Considering that the CO transition occurs between CO and Mott insulating states, the author concluded that V plays important role to determine $T_{CO}$ although previously H(D) in the H-bonds governs and triggers the CO transition.

## References

1) H. Mori, S. Yokomori, S. Dekura, and A. Ueda, Chem. Commun. **58**, 5668 (2022).
2) A. Ueda, S. Yamada, T. Isono, H. Kamo, A. Nakao, R. Kumai, H. Nakao, Y. Murakami, K. Yamamoto, Y. Nishio, and H. Mori, J. Am. Chem. Soc. **136**, 12184 (2014).
3) A. Ueda, A. Hatakeyama, M. Enomoto, R. Kumai, Y. Murakami, and H. Mori, Chem. Eur. J. **21**, 15020 (2015).
4) A. Ueda, K. Kishimoto, T. Isono, S. Yamada, H. Kamo, K. Kobayashi, R. Kumai, Y. Murakami, J. Gouchi, Y. Uwatoko, Y. Nishio, and H. Mori, RSC Adv. **9**, 18353 (2019).

†Current address: Institute of Multidisciplinary Research for Advanced Materials (IMRAM), Tohoku University, 2-1-1 Katahira, Aoba-ku, Sendai 980-8577

# Structural analysis on twist grain-boundaries

Kazutoshi INOUE[1], Mitsuhiro SAITO[2], and Yuichi IKUHARA[1,2,*]
[1] *Advanced Institute for Materials Research, Tohoku University, Sendai, Miyagi, 980-8577*
[2] *Institute of Engineering Innovation, The University of Tokyo, Yayoi, Tokyo, 113-8656*

Revealing the relationship between atomic structure and macroscopic properties is one of the most important issues in materials science. Grain boundaries (GBs) are especially important for their complex atomic structures and contribution to the properties. Historically, atomic structures of tilt GBs have been discussed by structural unit model. However, it is essential to consider the 3D atomic structure for twist GBs. The polyhedral unit model, which is an updated version of the structural unit model, rigorously describes the 3D GB atomic structure using a combination of atomic polyhedra. In this study, atomic models for [001] twist GBs in metals with $\Sigma \leq 53$ were built with a 3D periodic boundary condition. The translation models are systematically constructed by the 0.1 Å steps within the Displacement-Complete-Shift lattice to screen the stable atomic structures. Each model was firstly calculated to obtain GB energy without relaxation to screen the translation states. We applied the first-principles DFT calculations with the plane-wave basis projector-augmented wave method included in VASP to screen and determine the stable atomic structure by using cpu nodes in System B. The generalized gradient approximation was used for the exchange-correlation potentials in the Perdew-Burke-Ernzerhof form, employing an ultrasoft pseudopotential. The cutoff energy was set 400 eV for all plane-wave basis sets. The Brillouin-zone integrations were performed over a $4 \times 4 \times 1$ k-point mesh generated by the Monkhorst-Pack scheme. The GB energy is the interfacial excess free energy calculated by

$$\Delta E = \frac{1}{2A} \left( E_{\text{total}} - N\sigma_i \right),$$

where $E_{\text{total}}$ is the total energy of the system including GBs, $\sigma_i$ is the energy of the unit cell of the bulk crystal, $N$ is the number of unit cells contained in the supercell, and $A$ is the area of the GB. The GB energies for a fixed intergrain separation are within 0.1 J/m$^2$, indicating the energy landscape is almost flat. Then, atomic positions as well as the supercell volume of the most stable structure were relaxed such that all forces were $< 1.0 \times 10^{-5}$ eV/Å, and the residual force on each relaxed atom was 0.05 eV/Åunder the constant pressure of 0 Pa and constant temperature of 0 K. Then, interstitial voids in each model are calculated by Voronoi analysis, placing the sphere of maximal radius at the Voronoi vertex. The maximum diameter for each void center can be calculated within the hard sphere model and their maximum values vary from 0.30 to 0.50 in the unit of the lattice constant $a_0$. We show that the GB energies and the maximum void volumes have relatively high correlation, suggesting that the maximum void volume can be used to screen low energy translation states for twist GBs [1].

## References

[1] K. Inoue, K. Kawahara, M. Saito, M. Kotani, Y. Ikuhara: preprint (2022).

# First-Principles Lattice-Dynamics Calculations and Thermal Expansion Behavior for NASICONs

Yasuhide MOCHIZUKI[1], Takayuki NAGAI[2], Suguru YOSHIDA[3], Tsuyoshi KIMURA[2]

[1] *Department of Materials Science and Engineering, Tokyo Institute of Technology, 2-12-1 O-okayama, Meguro-ku, Tokyo*

[2] *Department of Advanced Materials Science, University of Tokyo, Kashiwa 277-8561 Chiba, Japan*

[3] *Materials Research Institute, Pennsylvania State University, University Park, Pennsylvania 16802, United States*

Negative-thermal-expansion materials have attracted considerable attention because they contribute to sustain the lifespan of largely expanding materials and also because of their fascinating and counter-intuitive thermal properties. The well-known and representative NTE materials are Si [1], $ReO_3$ [2], $ScF_3$ [3] $ZrW_2O_8$ [4] and $KZr_2P_3O_{12}$ (NASICON) [5]. Since the reports of NTE in various materials in the past few decades, it has been widely known that the mechanism for NTE is the transverse acoustic phonon modes, which have negative Grüneisen parameters. However, the detailed mechanisms for the NTE properties are uncovered ever since now. Here, we report our progress for elucidating the microscopic origin of NTE in $KZr_2P_3O_{12}$ and the relevant compounds.

Our first-principles calculations were performed by using the projector augmented-wave method [6], and the PBEsol functional within the generalized gradient approximation [7] as implemented in VASP [8]. The phonon band structures were derived from the calculated force constants using PHONOPY [9].

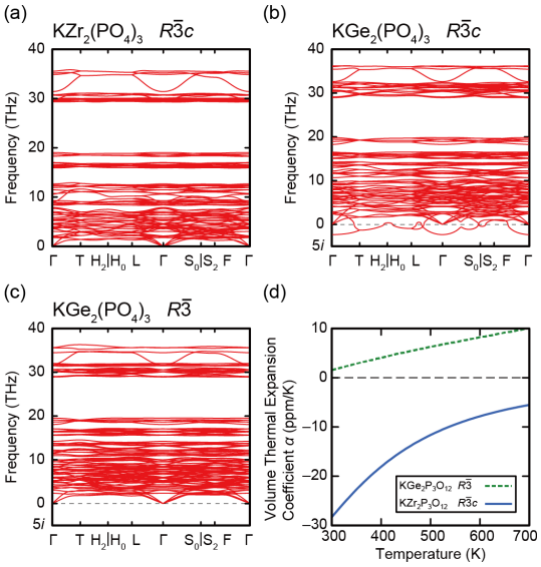


Fig. 1: Calculated phonon bands for the $R\bar{3}c$ phases of (a) $KZr_2(PO_4)_3$, (b) $KGe_2(PO_4)_3$, and the $R\bar{3}$ phase of (c) $KGe_2(PO_4)_3$. Calculated thermal expansion coefficients of $KZr_2(PO_4)_3$ and $KGe_2(PO_4)_3$ are also shown.

We present the calculation results of phonon bands for the $R\bar{3}c$ phases of $KZr_2(PO_4)_3$ (KZP) and $KGe_2(PO_4)_3$ (KGP) as shown in Fig. 1(a, b).

We can see that KZP is dynamically stable, whereas KGP is dynamically unstable. We found that the imaginary phonon mode in the $R\bar{3}c$ phase of KGP is $\Gamma_2^+$ ($A_{2g}$) phonon mode leading to dynamically stable $R\bar{3}$ phase, which is shown in Fig. 1(c). In our previous report, we found that the $\Gamma_2^+$ phonon mode (the rotational modes of $ZrO_6$ octahedra and $PO_4$ tetrahedra) is the most important for realizing negative thermal expansion in KZP [10] since the $\Gamma_2^+$ phonon mode has the largest negative value of Grüneisen parameter. By substituting *d*-block element Zr with *p*-block element Ge, the $\Gamma_2^+$ phonon mode became unstable because the rotational $\Gamma_2^+$ mode of $GeO_6$ octahedra and $PO_4$ tetrahedra trigger second-order Jahn-Teller effect, which lowers the electrons energy [11]. Here, as shown in Fig. 1(d), we have calculated the thermal expansion coefficients for KZP ($R\bar{3}c$ phase) and KGP ($R\bar{3}$ phase) by using quasi-harmonic approximation. We found that the $R\bar{3}$ phase of KGP has positive thermal expansion coefficients above room temperature because the $\Gamma_2^+$ phonon mode was transformed into $\Gamma_1^+$ ($A_g$) phonon in $R\bar{3}$, the negative Grüneisen parameter value of which was weakened.

In conclusion, we have shown that substituting Zr site with *p*-block element Ge makes the $R\bar{3}c$ phase (NASICON structure) dynamically unstable because the rotational phonon mode transforming as irreducible representation $\Gamma_2^+$ triggers second-order Jahn-Teller effect which lowers the electrons energy. Further, because the $\Gamma_2^+$ phonon mode is crucial for realizing negative thermal expansion, the lowered symmetry structure of KGP ($R\bar{3}$ phase) was transformed into a positive thermal expansion material.

## References

[1] S. Biernacki and M. Scheffler, *Phys. Rev. Lett.* **63**, 290 (1989).

[2] T. Chatterji *et al.*, *Phys. Rev. B* **78**, 134105 (2008).

[3] B. K. Greve *et al.*, *J. Am. Chem. Soc.* **132**, 15496 (2010).

[4] C. Martinek and F. Hummel, *J. Am. Ceram. Soc.* **51**, 227 (1968); T. A. Mary *et al*., *Science* **272**, 90 (1996).

[5] W. Miller et al., J. Mater. Sci. 44, 5441 (2009).

[6] P. E. Blöchl, *Phys. Rev. B* **50**, 17953 (1994).

[7] J. P. Perdew *et al.*, *Phys. Rev. Lett.* **100**, 136406 (2008).

[8] G. Kresse and J. Furthmüller, *Phys. Rev. B* **54**, 11169 (1996); G. Kresse and D. Joubert, *ibid* **59**, 1758 (1999).

[9] A. Togo and I. Tanaka, *Scr. Mater.* **108**, 1 (2015).

[10] Y. Mochizuki, S. Bae, and H. Raebiger, Activity Report of Supercomputer Center Institute for Solid State Physics 2021.

[11] T. Nagai, Y. Mochizuki, S. Yoshida, and T. Kimura, *J. Am. Chem. Soc.* **145**, 8090 (2023).

# Prediction of CO Adsorption Energy on Single Atom Catalysts Embedded in $TiO_2$ by Machine Learning

Kyoichi SAWABE
*Graduate School of Engineering, Nagoya University, Chikusa, Nagoya 464-8603*

This year, we conducted a feature analysis for machine learning (ML) prediction of CO adsorption energy on single-atom catalysts (SAC) using $TiO_2$ substrates.

We used the VASP program for spin polarization DFT calculations. Slab units with $n$ ($n = 2 - 6$) layers were used as models of $TiO_2$ surfaces. The electronic states of the SAC were modulated by changing both the thickness of the slab unit and the single metals embedded in $TiO_2$.

Good features for ML would require parameters of a chemically meaningful nature sufficient to describe the adsorption. In the case of CO adsorption on the SAC, $\sigma$ donation, $\pi$ back donation, and structural relaxation due to the adsorption are involved in the adsorption strength. Therefore, ML should use features that can describe these properties. Furthermore, data with a sufficient variation of these features must be used for ML. The $\sigma$ donation is related to the Lewis acidity of the adsorption site. The strength of $CH_3CN$ adsorption is often used experimentally and theoretically in order to measure the strength of Lewis acidity. Therefore, we calculated the strength of $CH_3CN$ adsorption on SACs. A linear regression of CO adsorption energy, $E_{ads}(CO)$, on r-$TiO_2$ (rutile type $TiO_2$) with respect to $E_{ads}(CH_3CN)$ was obtained with good accuracy, as shown in Fig. 1a. This means that $\sigma$ donation is dominant for the CO adsorption on r-$TiO_2$. In other words, information on $\pi$ back donation and structural relaxation was not available in the CO adsorption data on r-$TiO_2$. Applying the learning model obtained with the CO/r-$TiO_2$ data to the case of CO/a-$TiO_2$ (anatase type $TiO_2$), we obtained Figure 1b, in which the deviation of data points from the straight line of the prediction model appears as CO adsorption becomes stronger. Thus, the features of $\pi$ back donation and structural relaxation for the CO adsorption can be extracted from the additional data for a-$TiO_2$.

By eliminating the parameters that are highly correlated with each other using a Lasso regression, etc., a multiple linear regression (MR) model shown in Figure 1c was obtained. We used six parameters: $E_{ads}(CH_3CN)$, Charge, melting point, the heat of melting, crystalline system, and RMO, which is the distance between the embedded metal and the horizontally neighboring oxygen. Although the melting point and the heat of melting do not appear to have any chemical significance for CO adsorption, the above analysis indicated that they relate to the $\pi$ back donation and/or the structural relaxation.

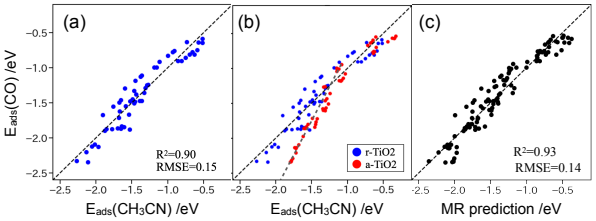


Figure 1: Linear regression model for $E_{ads}(CO)$ on (a) r-$TiO_2$ and (b) both r-$TiO_2$ and a-$TiO_2$ using $E_{ads}(CH_3CN)$. (c) Multiple linear regression model.

# Quantum transport theory based on large-scale first-principles electron transport calculations

NOBUHIKO KOBAYASHI
*Department of Applied Physics, University of Tsukuba*
*1-1-1 Tennodai Tsukuba Ibaraki 305-8573*

Analysis of transport properties from the atomistic level is an important issue from the viewpoint of materials science and technology. The purpose of this project is to analyze and predict the transport properties of materials from first-principles. We have developed the nonequilibrium Green's function (NEGF) method and the O(N) time dependent wave-packet diffusion (TD-WPD) method on the basis of the density functional theory (DFT). By using these methods, we have investigated charge, head and spin transport properties of materials. [1]

We have developed a Simulation code for Atomistic Kohn-sham Equation (SAKE) for the ab-initio electron transport calculation based on the DFT and NEGF formalism. [2] We have applied the method to analysis of thermoelectricity of Heusler compounds, chalcopyrite, and skutterudites. High performance systems are designed based on analysis of electronic structures and thermoelectric properties.

Organic semiconductors have attracted much attention for their applications to flexible, printable, lightweight, and low-cost electronic devices. They are crystals that are assemblies of $\pi$-conjugated molecules weakly bonded by van der Waals interactions, and electron transport properties are significantly influenced by electron-phonon interactions. We developed the O(N) TD-WPD method for the quantum transport calculation of huge systems of up to 100 million atoms a decade ago, and have been applied organic semiconductors. [3] It is possible to calculate the conductivity and the mobility of the system with micron-order lengths at room temperature at the atomistic levels, and also to analyze the transport properties of materials weakly bonded by van der Waals interactions. The electron and hole mobilities of the pentacene thin-film are calculated taking the effect of intramolecular vibrations on both the partially dressed polaron and the dynamic disorder into consideration by using TD-WPD method. It is demonstrate that electron mobility in high-mobility organic semiconductors is indeed limited by polaron formation. [4]

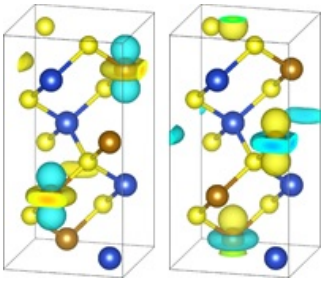

Figure 1: Wavefunctions of chalcopyrite CuFeS2.

## References

[1] N. Kobayashi, H. Ishii, K. Hirose, in *3D Local Structure and Functionality Design of Materials* eds H. Daimon, Y. C. Sasaki (World Scientific, 2018) p133.

[2] H.Takaki, N.Kobayashi, K.Hirose, *J. Phys.: Condens. Matter.* 32 325901(2020)

[3] H. Ishii, S. Obata, N. Niitsu, S. Watanabe, H. Goto, K. Hirose, N. Kobayashi, T. Okamoto, and J. Takeya, *Sci. Rep.* 10, 2524 (2020)

[4] H. Sato, S. A. Abd. Rahman, Y. Yamada, H. Ishii and H. Yoshida *Nat. Mater.* 21, 910 (2022).

# First-principles simulation of interfacial reactions using density functional theory and classical liquid theory

Minoru OTANI
*Center for Computational Sciences, University of Tsukuba*
*1-1-1, Tenno-dai, Tsukuba, Ibaraki 305-8577, Japan*

The electrochemical properties at the interface between electrode and electrolyte have much attention to improving the electrochemical performances of rechargeable batteries, fuel cells, and electrochemical catalysts. Because the electrochemical properties depend on the material properties constructing the electrochemical interface and environmental parameters such as the bias voltage, an exhaustive study is indispensable to understand the details of physical phenomena at the electrochemical interfaces.

To simulate the physical phenomena at the electrochemical interface, we have continuously developed the ESM-RISM method [1] that combines density functional theory using the effective screening medium technique (ESM) [2] and reference interaction site model (RISM) [3]. In this method, we treat the electrode surface and the reactants using the quantum mechanical theory and the solvation system using the classical solution theory. The electrostatic and van der Waals-type potentials describe the interaction between the quantum mechanical particles and classical solution. Because ESM-RISM is formulated under the grand-canonical ensemble, we can naturally address the formation of an electric double layer at the electrochemical interface using the half-cell system.

Although the modeling of the ESM-RISM method is physically reasonable, there is a well-known drawback of the RISM theory that underestimates the dielectric constant of a solution with dipolar solvent molecules. The dielectrically consistent RISM (DRISM) is one of the solutions to overcome the drawback of the RISM theory. This year, we have combined DRISM with the ESM-RISM framework to increase the accuracy of electrochemical interface simulations and applied it to the Pt(111)/aqueous water interface as a benchmark calculation [4].

First, to check the results of DRISM, we calculated the salt-concentration dependence of the activity coefficients for the bulk NaCl aqueous solution. The results of the conventional RISM underestimate the activity coefficients compared to the experiment, but DRISM well reproduces the experiment. Thus, DRISM improves the dielectric properties of the bulk solution. The results of electrochemical properties at the interface, such as the potential of zero charges, standard hydrogen electrode potential, double-layer capacitance, and thickness of the contact layer, are improved by DRISM and in reasonable agreement with the previous experiments and theories.

Further application results such as the theoretical analysis of oxide electrode degradations and the electrochemical catalysts will be reported elsewhere.

## References

[1] S. Nishihara and M. Otani: Phys. Rev. B **96**, 115429 (2017).

[2] M. Otani and O. Sugino: Phys. Rev. B **72**, 115407 (2006).

[3] A. Kovalenko and F. Hirata: Chem. Phys. Lett. **290**, 237 (1998).

[4] S Hagiwara, S Nishihara, F Kuroda, and M Otani: Phys. Rev. Mater. **6**, 093802 (2022).

# Theory of tunneling currents at semiconductor pn junctions in electric fields based on first-principles calculation

Takashi NAKAYAMA
*Department of Physics, Chiba University*
*1-33 Yayoi, Inage, Chiba 263-8522*

The tunnel field-effect transistor (TFET) is one of promising candidates for future energy-saving devices, due to its much steeper on-off switching features compared to conventional MOS FETs. Recently, we showed by the first-principles and one-dimensional wave-packet model calculations that the cooping of Al and N atoms around the Si-pn junctions produces impurity states in Si band gap and such states make the resonance with conduction-band states under the electric field of pn-junction, which shortens the tunneling length between p- and n-Si layers and markedly increases tunneling currents, in agreement with experiments.

The purposes of this work are to study (i) the tunneling current at Al-N co-doped Si-pn junctions by the three-dimensional more realistic calculations and (ii) how such tunneling current changes by the N-atom doping into the pn junctions made of direct band-gap semiconductors such as InP.

We consider the (100)-directed 2x2 pn junctions with 104 atom-layers of 5 typical semiconductors like Si and InP, as shown in Fig.1. The N-atom impurity is inserted in this junction. To simulate electronic structures of pn junctions, we adopt the conventional $sp^3d^5s^*$ tight-binding model, whose parameters are determined so as to reproduce electronic structures by the first- principles hybrid-DFT calculation. The calculation of the tunneling currents are performed using the non-equilibrium Green's function (NEGF) method, where the semi-infinite electrodes are attached to the left and right sides of the present junction in Fig.1.

Figures 2(a)-(b) show calculated tunneling currents as a function of the electric field, for Si, Ge, and GaP, and for InP and GaAs, respectively.

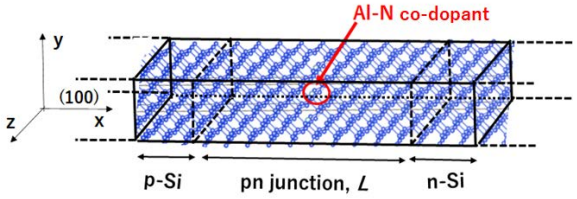


Fig.1. Schematic view of Al-N doped (100) Si-pn junction employed in this work.

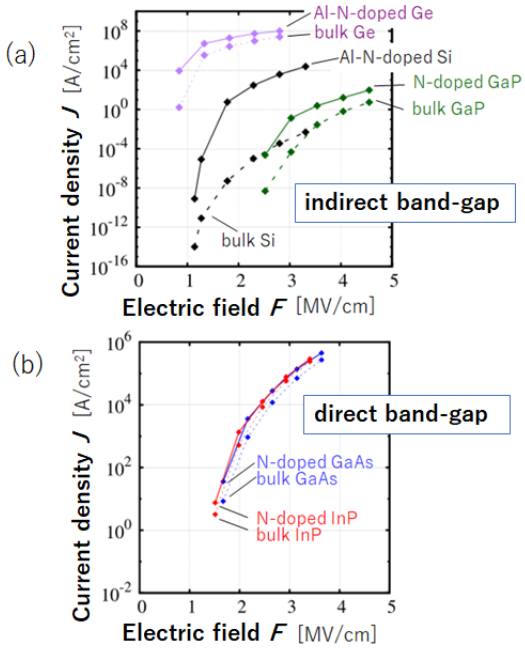


Fig.2. Calculated tunneling current as a function of electric field in pn junctions made of (a) Al-N-doped Si and Ge and N-doped GaP, and (b) N-doped GaAs and InP. The results for non-doped cases are also shown by dashed lines.

Here, both the currents in the cases with and without Al-N/N impurity atoms are shown. It is clearly seen that the Al-N/N-atom doping markedly increases the current by about $10^2$-$10^7$ times for the former indirect band-gap systems, while induces a slight current change for the latter

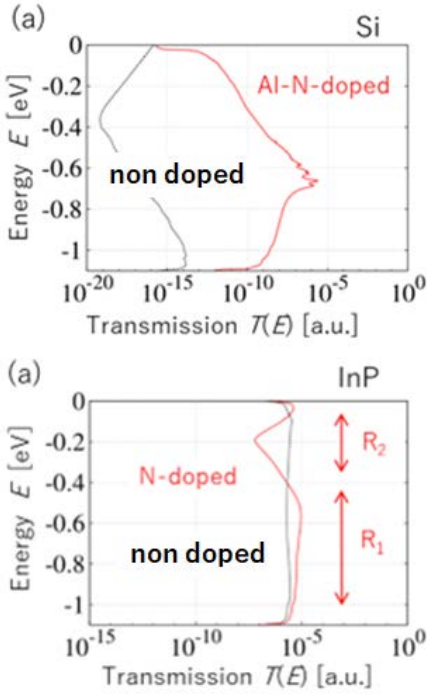


Fig.3. Calculated transmission spectra across pn junctions with and without Al-N/N impurity atoms by red and black lines, respectively, as a function of the energy in the tunneling energy window, for (a) Si and (b) InP.

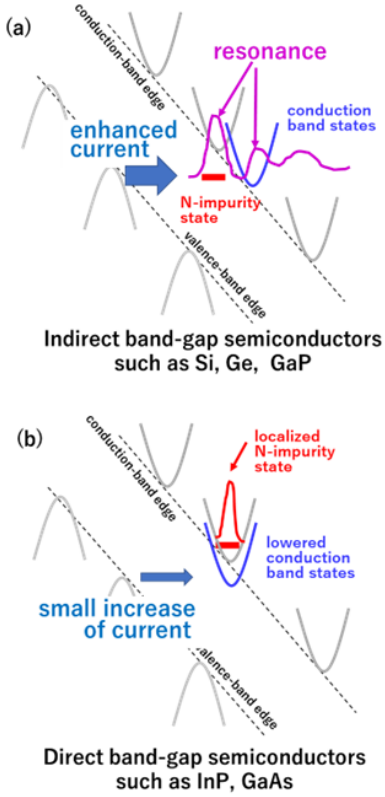


Fig.4. Schematic pictures to explain the effects of Al-N/N-atom doping on tunneling currents at pn junctions made of (a) indirect band-gap semiconductors like Si, Ge, and GaP, and (b) direct band-gap ones like InP and GaP.

direct band-gap systems.

To clarify the origin of current enhancement, we show in Fig.3(a) the transmission spectra of electrons for Si. It is seen that the transmission becomes much larger when impurity atoms are present, and its spectra have an extremely large peak around E=-0.66. By analyzing the local density of states around the pn junction, as shown in Fig.4(a), we found that the electric field in pn junctions produces the resonance between isolated Al-N/N states in the band gap and conduction-band states. These resonance states shorten the tunneling length and markedly enhances the tunneling current, which is in good agreement with experiments.

With respect to direct band-gap systems, we show in Fig.3(b) the transmission spectra for InP. It is seen that the transmission spectra have flat shape not depending on the energy without impurities, while they show small modulation around E=-0.4eV for the N-doped junctions. We found that, since the N-impurity states are located in the conduction bands for the direct band-gap systems as shown in Fig.4(b), the impurity doping only modulates the bands of host semiconductors, resulting in the slight change of tunneling currents.

All these calculations were performed using the xTAPP, VASP, and our original pspwf and NEGF codes. In order to realize the calculations for the present pn-junction systems, because the system is made of a large number of atoms (1000-2000 atoms), the advanced computing facility having multi-task and higher-speed CPU (more than 1280 cores × 2.0G Hz), larger-size memory (around 256GB), and larger-size strange (more than 2 TB) is indispensable. These conditions are realized only by the present ISSP supercomputing systems.

# Data-driven materials development using anharmonic phonon database

Masato OHNISHI

*Department of Mechanical Engineering, The University of Tokyo, Japan*

In recent years, Materials Informatics (MI) technology, which integrates informatics and materials science, has been rapidly developing. However, there is still a lack of databases for anharmonic phonon properties, which are crucial for the development of thermal functional materials, such as thermal insulators, thermoelectric materials, and thermal interface materials. In addition, because mechanical properties are closely linked to phonon properties, atomic vibrations, the availability of an anharmonic phonon property database would be valuable also for the design and development of various structural materials.

In this project, we have been developing an anharmonic phonon property database (APDB) for data-driven materials development. During the previous fiscal year (April 2022 to March 2023), we focused on establishing an automated workflow for calculating the thermal conductivity of the stable materials, those without negative (imaginary) phonon frequencies, in Phonondb[1]. We also generated thermal conductivity data for many materials using the developed automation code.

The developed automation code, written in Python, efficiently handles crystal structures and calls first-principles software (VASP[2]) and phonon analysis software (ALAMODE[3]). The established workflow is illustrated in Figure 1. Although multiple processes are involved in the entire calculation, the most computationally expensive one is calculating forces using the first-principles approach. As we aim to analyze

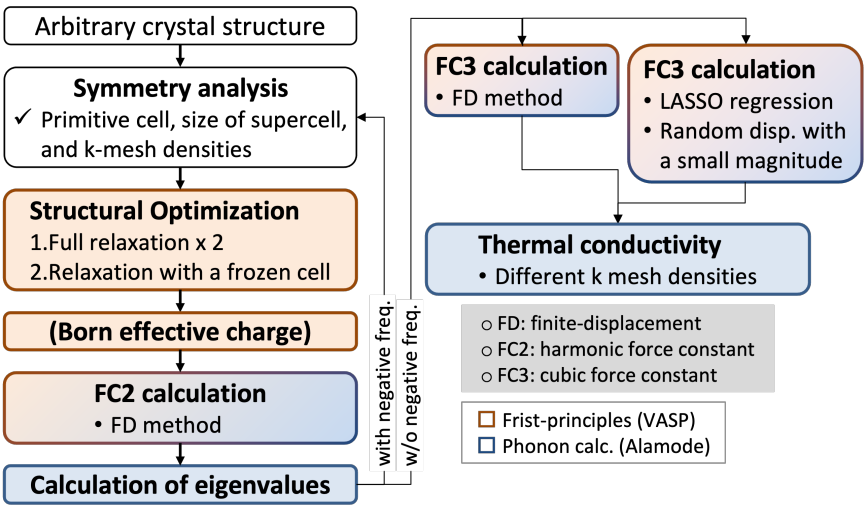


**Fig. 1** Workflow for the automation calculation of anharmonic phonon properties

many materials, parallelizing the calculation for each material is unnecessary. Instead, the "bulk" job, which allows the submission of numerous similar jobs as a single job, is optimal for our simulation. Using the "bulk" job, we can analyze up to 144 materials simultaneously in ISSP supercomputer. As a result, we have calculated thermal conductivities for approximately 2,000 materials using the ISSP supercomputer as well as HPCI supercomputers. Moreover, we have shared the developed automation code with collaborators worldwide so that they can also work on data generation.

After finishing the calculation for the stable materials in Phonondb in the fiscal year of 2023, we will release the developed database with computational details. The released database should allow easy accessibility to anharmonic phonon properties, enabling accurate prediction of material properties as well as material design for target properties.

## References

[1] Togo, http://phonondb.mtl.kyoto-u.ac.jp.

[2] G. Kresse and J. Hafner, Phys. Rev. B 47 , 558 (1993); ibid. 49 , 14 251 (1994).

[3] T. Tadano, Y. Gohda, and S. Tsuneyuki, J. Phys.: Condens. Matter 26, 225402 (2014)

# Impurity effects on $TiO_2$ and X-ray emission spectra of molecules by all-electron *GW* calculations using TOMBO

Kaoru OHNO

*Graduate School of Engineering, Yokohama National University*

*79-5 Tokiwadai, Hodogaya-ku, Yokohama 240-8501*

We found a new stable phase of anatase $TiO_2$ codoped with C and N having a relatively small band gap in our *GW* calculations [1] using the all-electron mixed basis program, TOMBO, which uses both plane waves and numerical atomic orbitals as basis functions [2]. Under intermediate oxygen pressure, the band gap of $TiO_2$ codoped with C and N was found to be 2.28 eV. Therefore, this phase can be used as a visible-light-response photocatalyst.

The initial state of X-ray emission spectroscopy (XES) and resonant inelastic X-ray scattering (RIXS) is an excited eigenstate with a deep core hole after the X-ray photoelectron spectroscopy (XPS) and X-ray photoabsorption spectroscopy (XAS), so that their calculations offer a good example of extended quasiparticle theory (EQPT) [3] in many-body perturbation theory (MBPT). Moreover, to overcome the basis set incompleteness problem, we adopt the all-electron mixed basis program, TOMBO. Here we applied the one-shot *GW* + Bethe--Salpeter equation (BSE) approach in MBPT to this problem on the basis of EQPT and analyze XES and RIXS energies for $CH_4$, $NH_3$, $H_2O$, and $CH_3OH$ molecules [4]. Figure 1 shows the RIXS spectra of a $CH_3OH$ molecule calculated by our method together with the experimental data [5]. The agreement is excellent without introducing any empirical fitting parameter.

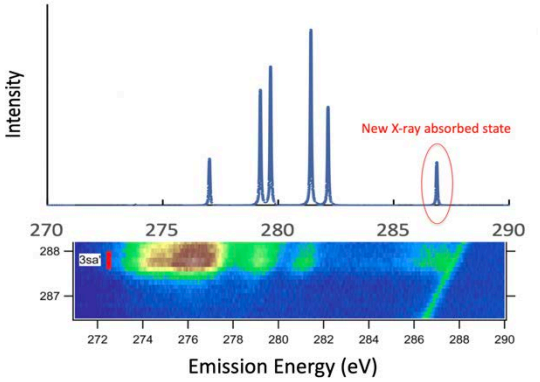


Fig. 1: Calculated [4] (above) and experimental [5] (below) RIXS spectra of a $CH_3OH$ molecule.

## References

[1] T. Ishikawa, R. Sahara, K. Ohno, K. Ueda, & T. Narushima: Comp. Mat. Sci. **220** (2023) 112059.

[2] S. Ono, Y. Noguchi, R. Sahara, Y. Kawazoe, & K. Ohno, Comp. Phys. Comm. **189** (2015) 20.

[3] K. Ohno, S. Ono, & T. Isobe: J. Chem. Phys. **146** (2017) 084108.

[4] K. Ohno & T. Aoki: PCCP **24** (2022) 16586.

[5] A. Benkert, F. Meyer, D. Hauschild, M. Blum, W. Yang, R. G. Wilks, M. Bär, F. Reinert, C. Heske & L. Weinhardt,: J. Phys. Chem. A **120** (2016) 2260.

# Development of a first-principles calculation software for a many-body wave function theory

Masayuki OCHI
*Forefront Research Center, Osaka University*
*1-1 Machikaneyama-cho, Toyonaka, Osaka 560-0043*

We have developed a first-principles electronic structure calculation software using the transcorrelated (TC) method [1, 2]. The TC method is a many-body wave function theory, where Hamiltonian is similarity-transformed with the Jastrow correlation factor. By this transformation, electron correlation effects are efficiently considered. In particular, one-electron orbitals in the Jastrow-Slater-type wave function can be optimized in the same manner as the Hartree–Fock (HF) method, to say, by solving a one-body self-consistent-field (SCF) equation. It is advantageous that the computational cost for this process is the same order as that for the HF method [3].

In this year, we have published our computational code TC++ on github [4] together with its technical details [5], including efficient treatment of the three-body interactions included in the similarity-transformed Hamiltonian and accurate correction terms for the divergence of the effective potentials in the reciprocal space. One can perform the TC calculation using TC++ by reading some output files dumped by DFT calculation using the Quantum-Espresso package [6]. TC++ supports the following functionalities: HF, TC, and biorthogonal TC (BITC) calculations, SCF and band calculations, solids and homogeneous electron gas, a plane-wave-basis set, and norm-conserving pseudopotentials. At present, the Jastrow factor has a simple random-phase-approximation-type form, but TC++ will support more general types of the Jastrow factor soon. Calculation is MPI-parallelized for the k-point and band indices. Using supercomputers of ISSP, we have performed several test calculations on several kinds of solids, to check the applicability of our code and verify the accuracy of calculated quantities, e.g., a band structure and a total energy. As reported in our previous studies (e.g., [3]), calculated band gaps are more accurate than LDA and GGA, but the total energy is at present less accurate. Now we have tested the accuracy using a polynomial-type Jastrow factor including a larger number of optimizable parameters.

## References

[1] S. F. Boys and N. C. Handy, Proc. R. Soc. London Ser. A **309**, 209 (1969); *ibid.* **310**, 43 (1969); *ibid.* **310**, 63 (1969); *ibid.* **311**, 309 (1969).

[2] N. C. Handy, Mol. Phys. **21**, 817 (1971).

[3] M. Ochi, K. Sodeyama, R. Sakuma, and S. Tsuneyuki, J. Chem. Phys. **136**, 094108 (2012).

[4] https://github.com/masaochi/TC

[5] M. Ochi, Comput. Phys. Commun. **287**, 108687 (2023).

[6] https://www.quantum-espresso.org/

# Development of Polymer Electret Materials for Energy Harvesting Using Machine Learning

Yucheng ZHANG, Zeitan MAO, Kuniko SUZUKI, and Yuji SUZUKI

*Department of Mechanical Engineering*

*The University of Tokyo, Hongo, Bunkyo-ku, Tokyo 113-8656*

Electret is a dielectric material with quasi-permanent charges and can trap charges stably for decades. Vibrational electret energy harvester (VEEH) can generate electricity efficiently from kinetic energy via the electrostatic induction. The VEEH with bipolar (both positively and negatively charged) electret leads to four times output power theoretically, thus specifying the importance of designing high-performance bipolar polymer electrets.

CYTOP (Cyclic Transparent Optical Polymer, AGC Chemicals) is one of the best polymer electret materials as shown in Fig. 1. Recently, we utilized quantum chemical analysis for evaluating the charge trap of CYTOP electrets [1]. It is found that although the repeat-unit-number of CTX-A is above 1000, the trapped charge is localized at the amide bond, which is formed by dehydration reaction between the carboxyl end group and the amine introduced.

Recently, by employing the de novo molecule generation and the functional group enrichment analysis, we successfully proposed the electret CTX-A/APDEA with high bipolar charging performance via combining CTX-A with N-(3-aminopropyl) diethanolamine [2].

This result encouraged us to move further to search new amines in the open-source database PubChem, aimed at designing better bipolar polymer electret based on CYTOP CTX-A after the dehydration reaction. It is also shown that the ionization potentials (IPs) computed by the density functional theory (DFT) with polarizable continuum model (PCM) correction agree well with the trends of the surface charge density and charge stability measured by the wet experiments [3,4].

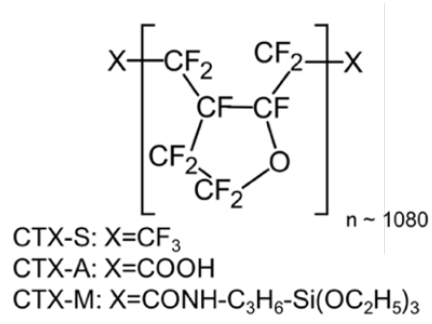


**Fig. 1.** Chemical structure of CYTOP series.

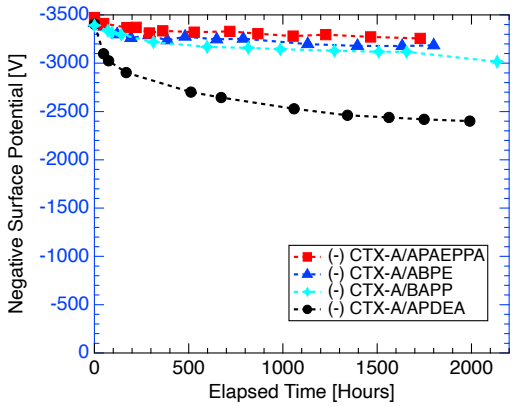


Figure 2. Surface potential decay versus elapsed time for negatively-charged with -3.5 kV, stored under room temperature.

To prepare the labeled data, 5522 amines were initially sampled from the PubChem. Thereafter, the virtual dehydration reaction was conducted and PCM-DFT computation was automatically made. Subsequently, 80% of the data for solid-state IPs and the information on molecules and bonds was employed to teach the deep learning model named MEGNet [5]. Two sets of the data (10 % each) were used as the validation/test sets. As a result, the mean absolute error (MAE) of solid-state IP is found to be as small as 0.326 eV. The computational cost with this approach is significantly lower than PCM-DFT, enabling rapid screening of huge databases to find candidates for new high-performance bipolar polymer electrets.

We also made another MEGNet to predict the boiling point, because the amines should not be evaporated at the thermal curing temperature of the CYTOP polymer.

Candidates are re-examined with PCM-DFT to get accurate solid-state IP. Three amines APAEPPA, ABPE, and BAPP have finally been selected. Figure 2 shows the surface potential for those films (15 μm in thickness) after charging to -3.5 kV. It is found that the materials obtained in this study are superior to our previous CTX-A/APDEA in terms of charge stability [4].

All the quantum chemical calculations are made with the software GAUSSIAN [5] at the DFT level with the CAM-B3LYP functional and 6-31+G(d,p) basis set, while PCM is combined for solid-state analysis due to the solvation effect correction.

This work was partially supported by JST CREST Grant Number JPMJCR15Q3 and JPMJCR19Q1. The calculations are performed with SGI ICE XA ISSP system B with 1 node (24 CPUs).

## References

[1] Kim S., et al., J. Phys. Chem. B, Vol. 124, No. 46, pp. 10507-10513 (2020).

[2] Zhang, Y., et al., Appl. Phy. Lett., 118, 223904 (2021).

[3] Mao, Z., et al., IEEE Conf. Electr. Insul. Dielectr. Phenom., pp. 667-670 (2021).

[4] Mao, Z., et al., Adv. Mater., submitted.

[5] M. Frisch et al., “Gaussian 09, Rev. A. 1,” Gaussian, Inc. Wellingford, CT, (2009).

# Design and Understanding of Catalysts Realized by Theory and Machine Learning

Hao Li

*Advanced Institute for Materials Research (WPI-AIMR),*

*Tohoku University, Sendai 980-8577, Japan*

## 1. Introduction

Catalyst design is essential for realizing a sustainable society. However, it is sometimes challenging due to the complicated reaction networks and surface phases under reaction conditions. To address this challenge, *ab initio* calculations, molecular dynamics, and microkinetic modeling can help better understand the reaction and make predictions.

## 2. Computational Methods

In this project, DFT calculations were performed using VASP with the exchange–correlation energetics described by the Perdew, Burke, and Ernzerhof (PBE) or the revised PBE (RPBE) functional. The generalized gradient approximation was employed. Ion–electron interactions were described by the framework of projector-augmented plane-wave method. The energy cutoff was set to at least 400 eV. Spin-polarization was included when necessary. Brillouin zone was sampled by the Monkhorst-Pack method. Transition states were located by the climbing-image nudged elastic band.

## 3. Results and Discussion

### 3.1. Surface state analysis

Due to the equilibrium between water and adsorbate, the surface state of an electrocatalyst is usually different from its pristine form at operating conditions. Meanwhile, the electrochemical surface state of a catalyst is essential in determining the catalyst activity. In this project, we analyzed the surface states of typical transition metal X-ides (TMXs) and emerging M-N-C catalysts, and found that their catalytic surfaces generally differ from their stoichiometric forms [1-2]. A typical example is shown in Fig. 1, where the surfaces of dual-atom M-N-C are usually pre-covered [1]. These show that we should probe the surface state before analyzing the electrocatalytic activity.

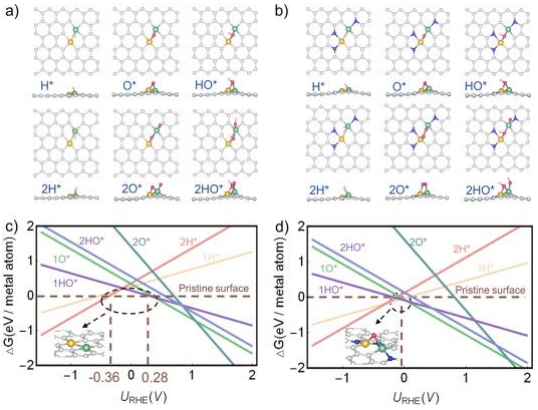


Fig. 1: Examples of the calculated surface Pourbaix diagrams of dual-atom M-N-C catalysts. (a-b) Optimized structures. (c-d) Surface Pourbaix diagrams. Reprinted with

permission from Ref. [1].

### 3.2. Catalysis theory development

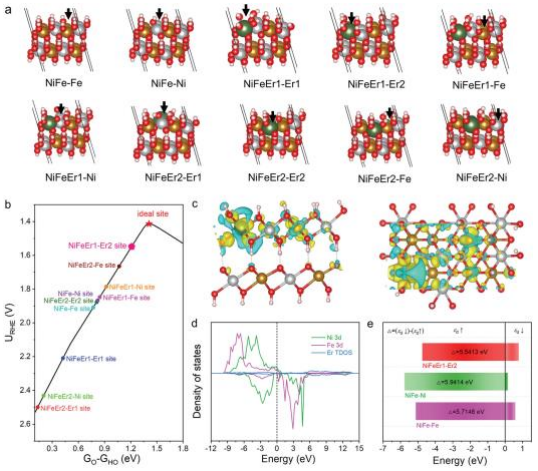


Fig. 2: (a) The Er-NiFe-LDH considered for simulations. (b) Microkinetic modeling to analyze OER activities of various sites at Er-NiFe-LDH. (c) Charge density differences. (d) Projected density of states. (e) Calculated spin-polarized *d*-band centers of different systems. Reprinted with permission from Ref. [3].

We also analyzed various catalysts and their performances based on catalysis modeling. The analyzed catalyst systems include TMXs and single-atom catalysts. The analyzed reactions include oxygen evolution (OER) [3], oxygen reduction [4], and nitrogen reduction [5]. An example is shown in Fig. 2 [3], in which we analyzed the OER activities of Er-doped NiFe layered double-hydroxide (LDH). Besides, we also studied thermal catalysis, such as $Hg^0$ oxidation.

### 3.3. Machine learning (ML) analysis

In addition to DFT-based analysis, this project performed explainable ML modeling to identify the role of element La as the active center of ORR in alkaline media [6]. Based on ~7800 experimental data, we derived the key role of La and found that those materials with La could possess good ORR performance. These show that ML can not only provide prediction, but also unravel the structure-performance relation of electrocatalysts.

## 4. Conclusion

Through this ISSP project, we performed comprehensive analyses to understand some promising electrocatalytic materials. We found that surface state is an essential factor in electrocatalysis that should not be dismissed before the activity analyses of many catalysts. Also, explainable ML can help identify the critical factor of a material in electrocatalysis.

## References

[1] W. Yang, J. He, B. Zhou, L. Wei, Z. Gao*, H. Li, Commun. Chem. **6**, 6 (2023).

[2] H. Liu, X. Jia, A. Cao, L. Wei, C. D'agostino, H. Li, J. Chem. Phys. **158** (2023).

[3] Y. Zhu, X. Wang, X. Zhu, Z. Wu, D. Zhao, F. Wang, D. Sun, Y. Tang, H. Li, G. Fu, Small, **19**, 5 (2023).

[4] C. Liu, Z. Yu, F. She, J. Chen, F. Liu, J. Qu, J. M. Cairney, C. Wu, K. Liu, W. Yang, H. Zheng, Y. Chen, H. Li, L. Wei, Energy Environ. Sci. **16**, 446 (2023).

[5] Y. Zhang, Z. Yu, F. She, L. Wei, Z. Zeng, H. Li, J. Colloid Inter. Sci. **640**, 15 (2023).

[6] R. Zhao, Z. Chen, Q. Li, X. Wang; Y. Tang, G. Fu, H. Li, J-M. Lee, S. Huang, Chem. Catal. **2**, 3590 (2022).

# First principles study of the adsorption structure of helicene on the Ag(111) surface

Yuji HAMAMOTO

*Department of Precision Engineering, Graduate School of Engineering*

*Osaka University, Yamada-oka, Suita, Osaka 565-0871*

Molecular chiral recognition has drawn growing attention due to its importance in biochemistry and pharmacology, and has been studied using a model system composed of chiral molecules adsorbed on a solid surface. The molecular adsorption structure provides a key to the origin of chiral recognition, whereas its detail is beyond the reach of experimental techniques such as scanning tunneling microscopy.

Here we resort to density functional theory (DFT) calculations to investigate the adsorption structure of 7-thiaheterohelicene (7TH) on the Ag(111) surface. Although 7TH forms a one-dimensional chain on Ag(111), we focus on single molecule adsorption to clarify the interaction of the S atoms of 7TH with the Ag surface. The van der Waals interaction between 7TH and Ag(111) is considered by using the van der Waals density functional (vdW-DF) method [1] and the rev-vdW-DF2 functional [2].

We first estimate the adsorption site and orientation of a 3TH molecule on Ag(111). The optimal site and orientation for 3TH are used to make an initial guess on the local structure of 7TH near Ag(111). We then optimize the adsorption height and relax the whole system to determine the adsorption structure of 7TH on Ag(111). The adsorption structure shown in Fig. 1 indicates that 7TH physisorbs on Ag(111), i.e., the S atoms play a minor role in the molecular adsorption. This allows us to use classical molecular dynamics (MD), which is computationally much cheaper than DFT, to investigate the formation of a 7TH chain on Ag(111). The results for the MD simulations will be discussed in more detail elsewhere [3].

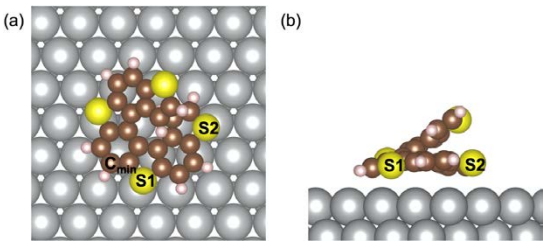


Fig. 1: Adsorption structure of 7TH on Ag(111). Top (a) and side (b) views are shown.

## References

[1] M. Dion, H. Rydberg, E. Schröder, D. C. Langreth, and B. I. Lundqvist, Phys. Rev. Lett. **92**, 246401 (2004).

[2] I. Hamada, Phys. Rev. B **89**, 121103(R) (2014).

[3] C. Ye et al., in preparation.

# Global search for metastable structures of silicene on the Ag(111) surface by Gaussian process regression

Yuji HAMAMOTO

*Department of Precision Engineering, Graduate School of Engineering*

*Osaka University, Yamada-oka, Suita, Osaka 565-0871*

Silicene, a silicon analog of graphene, has been intensively studied in the last decade, because of its peculiar phenomena, as well as its better compatibility with the silicon-based electronics than graphene. Density functional theory (DFT) calculations reveal that freestanding silicene is characterized by the alternately buckled honeycomb lattice, whereas silicene grown on the Ag(111) surface exhibits a variety of nontrivial buckling patterns, which makes it difficult to theoretically predict stable structures of silicene on Ag(111). To overcome the difficulty, we here adopt a structure search method based on an evolutionary algorithm (EA) and the Gaussian process (GP) regression [2]. This method accelerates the structure search by relaxing the structures generated with EA, using the energy landscape predicted with GP instead of that obtained by computationally expensive DFT calculations.

Our results demonstrate that the method not only reproduces the well-known buckled structures of silicene on Ag(111), but also predict new structures that have never been reported as far as we know. For example, our results predict at least seven phases for the $\sqrt{13} \times \sqrt{13}R19.1°$ unit cell relative to Ag(111), which are classified into type-II [Figs. 1(a)-1(c)] and type-I [Figs. 1(d)-(g)] phases based on the angle between the Ag[110] and Si[110] directions. The type-I phases are characterized by one, two, or three protruded Si atoms, and are energetically comparable with each other. These behaviors are analogous to the so-called T phase, whose structures is hard to identify experimentally and still under discussion.

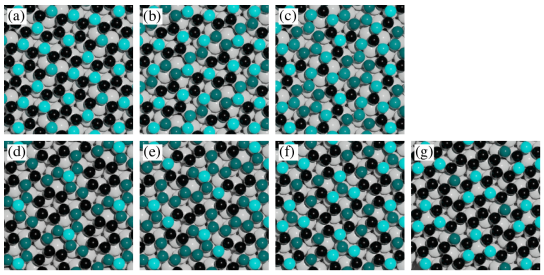


Fig. 1: $\sqrt{13} \times \sqrt{13}R19.1°$ phases obtained with the structure search method. The bright (dark) cyan balls denote higher (lower) Si atoms.

## References

[1] K. Takeda and K. Shiraishi, Phys. Rev. B **50**, 14916 (1994).

[2] M. K. Bisbo and B. Hammer, Phys. Rev. Lett. **124**, 086102 (2020).

# High-accuracy machine-learning interatomic potential and massively large-scale molecular simulation for microscopic mechanisms of grain-boundary-dislocation interactions

Tatsuya YOKOI

*Department of Materials Physics*

*Nagoya University, Furo-cho, Chikusa-ku, Nagoya, Aichi, 464-8601*

In polycrystalline metals and alloys, grain boundaries (GBs) exist and generally interact with dislocations, thereby having great impacts on mechanical properties though GB strengthening. It is thus essential to understand the relationship between GB structures, their interaction with dislocations and mechanical properties at various length scales, with the goal of optimal design of polycrystalline microstructure in metals and alloys.

For this purpose, previous theoretical studies performed large-scale molecular simulations based on classical empirical interatomic potentials, in order to determine atomic structure and energetics at GBs. However, their adjustable parameters are fitted only to bulk properties without consideration of atomic environments of GBs. This often leads to critical errors in predicting atomic structures and energetics of these lattice defects. In addition, classical empirical potentials are typically based on simple analytic functions and thus show limited transferability to various atomic environments for lattice defects.

To tackle the above issue, this work constructed an artificial-neural-network (ANN) interatomic potential and combined it with molecular simulations. For a preliminary analysis, aluminum was chosen as a model system [1,2]. The ANN potential was used to predict favorable atomic structures and energetics for symmetric tilt GBs. The predicted results were then validated by performing density-functional-theory (DFT) calculations.

As illustrated by Fig. 1, the ANN potential was constructed by following the architecture reported by Behler and Parinello [3] and Behler [4], with two hidden layers each having 48 nodes.

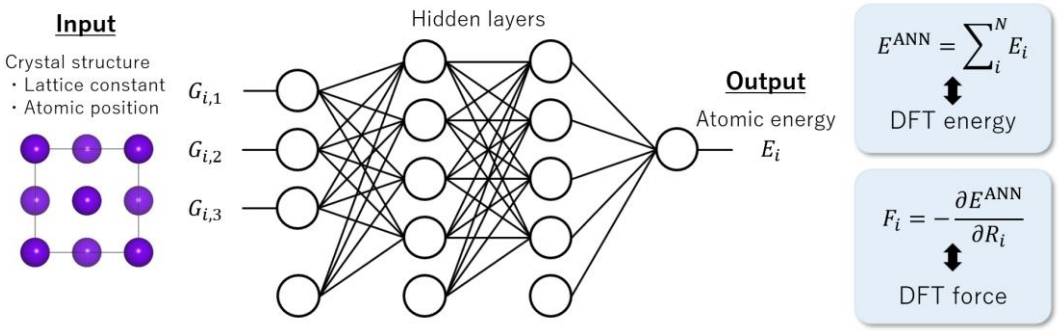


Fig. 1 Schematic illustration of an ANN potential.

Two- and three-body symmetry functions were employed to encode the atomic environment of each atom and to provide the input value for the ANN potential. In order to generate training datasets, DFT calculations were performed using the projector augmented wave (PAW) method in the VASP [5,6]. The exchange-correlation energy was calculated using a revised version of the generalized gradient approximation parameterized by Perdew, Burke and Ernzerhof (GGA-PBEsol) [7].

In order to cover a wide range of atomic environments, not only single crystals but also lattice defects including point defects, surfaces and GBs were used as references for generating the training datasets. With those reference structures, structural relaxation and molecular dynamic simulations were performed, and snapshots were extracted from the calculated results. The total potential energy and atomic force were used as the training datasets. The ANN potential was trained using an extended Kalman filter and then combined with structural relaxation and molecular dynamics.

It was found that all training datasets exhibit sufficient small errors, including the GBs in the training datasets. The mean absolute errors (MAEs) were evaluated to be 1.46 meV/atom and 17.1 meV/Å for the total energies and atomic forces, respectively, which are comparable to previous studies. It is thus expected that the present ANN potential exhibits an excellent accuracy to predict GBs.

Then structural relaxation calculations with the ANN potential were performed to predict the relationship between atomic structures and GB energies for symmetric tilt GBs with the $[001]$ and $[\bar{1}10]$ rotational axes. The predicted atomic structures were used to perform DFT calculations and to calculate their GB energies in the DFT level. As a result, the ANN potential is found to accurately predict GB energies from low to high energy states for all the GBs examined. In addition, the lowest-energy structures predicted by the ANN potential were the same as those for DFT calculations. These results suggest that the ANN potential can be used to predict the lowest-energy structures and their GB energies prior to DFT validation, which will greatly reduce computational cost for searching for energetically favorable atomic structures for GBs.

In future research, the ANN potential will be applied to dislocations, in order to evaluate its ability to predict core structures and formation energies for dislocations.

**References**

[1] T. Yokoi et al., submitted.

[2] T. Yokoi et al., prepared.

[3] J. Behler, M. Parrinello, Phys. Rev. Lett. 98, 146401 (2007).

[4] J. Behler, Int. J. Quantum Chem. 115, 1032-1050 (2015).

[5] G. Kresse, D. Joubert, Phys. Rev. B **59**, 1758-1775 (1999).

[6] G. Kresse, J. Furthmüller, Comput. Mater. Sci. **6**, 15-50 (1996).

[7] J. P. Perdew et al., Phys. Rev. Lett. **100**, 136406 (2008).

# Development of crystal structure prediction method and material search

Tomoki YAMASHITA
*Top Runner Incubation Center for Academia-Industry Fusion, Nagaoka University of Technology*
*1603-1 Kamitomioka-machi, Nagaoka, Niigata, 940-218*

We have studied the structural stability of SrO on MgO substrates since SrO with unknown crystal structure synthesized on MgO substrate has been reported [1]. There is an approximately 20 percent mismatch between the lattice parameters of SrO (5.16 Å) and MgO (4.22 Å), which could affect the structural stability of SrO We performed crystal structure prediction (CSP) simulations for $Sr_4O_4$ using CrySPY [2]. Four hundred structures of tetragonal $Sr_4O_4$ were randomly generated with the lattice constant of the MgO(100) substrate. Only the lattice constant $c$ was relaxed during structural optimization using Quantum ESPRESSO. Here, GGA is used for the exchange-correlation functional. The results of the search showed that the rocksalt-type structure was not the most stable under the constraint on the lattice constant $a$. The four-coordinated structures were more stable than others. Alhough the predicted structure differs from that obtained experimentally, we found that the lattice constraints make the rocksalt structure unstable.

We have also searched for solid electrolyte materials that can be synthesized in the systems of Li-Mg-$P_2O_7$ using CSP with CrySPY [2]. We perfromed randam search simulations for $LiMg_{1.5}P_2O_7$, $Li_2MgP_2O_7$, and $Li_3Mg_{0.5}P_2O_7$. In each composition, 1000 random structures were locally optimized using the VASP code. The CSP simulations were conducted using GGA-PBE, and PBEsol was also used for the structures with low energy. We obtained a structure with a hull distance of 2 meV/atom for $Li_2MgP_2O_7$, and structures with a hull distance of about 20 meV/atom for $LiMg_{1.5}P_2O_7$ and $Li_3Mg_{0.5}P_2O_7$. In addition to the randam search simulations, DFT calculations were also performed to evaluate the energy of $Li_2MgP_2O_7$ with the $P_2O_7$ framework in the $Li_{2.2}Zn_{0.8}P_2O_7$ (LZ) structure [3]. From a vast number of combinations of cation sites in the LZ structure, the top 10 structures with the lowest Mardelung energy were adopted for DFT calculations. The lowest energy of the LZ structure was only a few meV higher than the energy of the structure found in RS simulations (RS structure). The RS structure become unstable when the cationic site changes, which increases the energy. On the other hand, the LZ structure have almost no change in energy when the cation site was exchanged.

## References

[1] K. Komatsu, T. Shirai, A. Nakamura, A. Kato, S. Ohshio, N. Nambu, I. Toda, H. Muramatsu, H. Saitoh, Ceramics International **39**, 7115 (2013).

[2] T. Yamashita, S. Kanehira, N. Sato, H. Kino, H. Sawahata, T. Sato, F. Utsuno, K. Tsuda, T. Miyake, and T. Oguchi, Sci. Technol. Adv. Mater. Meth. **1** (2021) 87.

[3] A. E. Lapshin and M. A. Petrova, Glass Physics and Chemistry, **36**,75 (2010).

# Study of the Principle of Photothermal Conversion by *Ab Initio* Calculations

Mizuho ONO[1], Hiroki GONOME[2]

[1]*Graduate School of Engineering,*

*Tohoku University, Aoba-ku, Sendai, Miyagi 980-0845*

[2]*Graduate School of Science and Engineering,*

*Yamagata University, Jonan, Yonezawa, Yamagata 992-8510*

In light-matter interactions, the electrons and nuclei that composes matter interact with each other, but the physical processes are extremely complex and fast. In simulations of matter that reproduce this situation, the Born-Oppenheimer approximation is typically applied and the motion of the electrons is decoupled from that of the nucleus. On the other hand, it has been reported that non-negligible non-adiabatic effects between the electrons and the nucleus can act on molecules moving under a strong external field [1]. The objective of this work is to evaluate the effect of the external field on the energy of the system by performing coupled calculations of the electron and lattice (nuclear) systems without applying the Born-Oppenheimer approximation. The coupled calculations treat non-adiabatic motion by applying Ehrenfest dynamics with time-dependent density functional theory and classical molecular dynamics (TDDFT-MD) for the electron and lattice. The time waveform of the incident electric field in the simulation is shown in Figure 1. The light intensity is $10^{13}$ W/cm$^2$ and the central frequency is 3.10 eV. Figure 2 shows the total energy excluding the kinetic energy of the lattice and the kinetic energy of the lattice in the TDDFT-MD simulation results for the silicon crystal. During the application of an electric field, the energy of the system increases rapidly, while the kinetic energy of the lattice remains almost unchanged. In other words, the energy increase of the system is dominated by the interaction between the electromagnetic waves and the electrons. The kinetic energy of the lattice then begins to fluctuate after 300 fs due to electron-lattice interactions. The numerical analysis therefore shows that the lattice system is hardly displaced

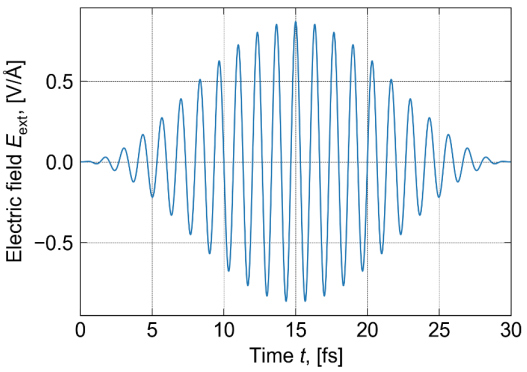


Fig. 1: Incident electric field

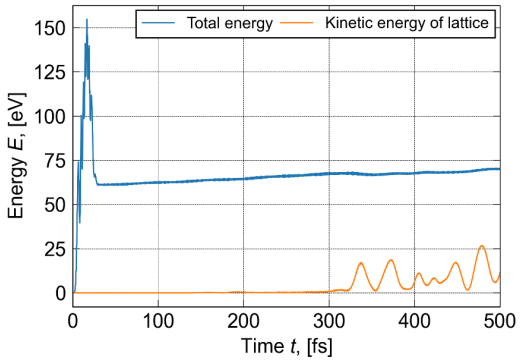


Fig. 2: Total energy and kinetic energy of lattice.

directly by the applied electric field but receives energy through the interaction with the electron system.

## References

[1] C. Lian, S.B. Zhang and S. Meng, Phys. Rev. B. **94**, 184310 (2016).

# Development of a full *GW* electron-hole interaction kernel for the Bethe-Salpeter equation

Yoshifumi NOGUCHI

*Department of Applied Chemistry and Biochemical Engineering, Graduate School of Engineering, Shizuoka University, Johoku 3-5-1, Hamamatsu, Shizuoka 432-8561, Japan*

In 1995, Onida, et al., initiated the first-principles *GW*+Bethe-Salpeter simulations for a $Na_4$ cluster [1]. Since then, the method has been applied to a wide-range of materials in which it has demonstrated its accuracy and reliability. However, the conventional simulations need to employ an additional approximation to a *GW* electron-hole interaction kernel ($\Xi^{GW}$) without exception solving the equation. Specifically, the employed approximation neglects the two second-order exchange terms in the *GW* electron-hole interaction kernel based on an unconfirmed assumption that the second-order terms have a negligibly small contribution. Therefore, it is evident that the conventional *GW*+Bethe-Salpeter method does not satisfy the Baym-Kadanoff conservation low [2].

Considering not only the first-order direct and exchange terms but also the two second-order exchange terms, we have developed a *GW*+Bethe-Salpeter method with a full *GW* electron-hole interaction kernel and implemented it into our original all-electron mixed basis program [3]. Figure 1 shows the Feynman diagrams of the full *GW* electron-hole interaction kernel. We simulated the $S_1$ optical gap of 28 typical organic molecules in Thiel's set [4] and revealed the contributions of the two second-order exchange terms. The effects of the method with a full *GW* electron-hole interaction kernel are 0.2 eV maximum for the $n \rightarrow \pi^*$ excitations and negligibly small for the $\pi \rightarrow \pi^*$

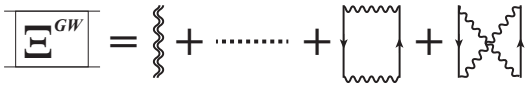


**Figure 1. Full *GW* electron-hole interaction kernel.**

and $\pi \rightarrow$Rydberg excitations compared with the those of the conventional method. The results of our exciton analysis method suggest that the contribution of the second-order exchange terms tends to be larger for higher exciton binding energies.

## References

[1] G. Onida, et al., Phys. Rev. Lett. **75**, 818 (1995).

[2] G. Baym and P. Kadanoff, Phys. Rev. **124**, 287 (1961).

[3] S. Yamada, et al., Phys. Rev. B. **105**, 045113 (2022).

[4] M. R. Silva-Junior and W. Thiel, J. Chem. Theory Comput. **6**, 1546 (2010).

# Ab-initio research on nano structures of magnetic nano particles

Yasutomi TATETSU

*Meio University, Biimata, Nago, Okinawa 905-8585*

The search for advanced materials that possess both thermodynamic stability and instability for different applications has become a hot topic in recent years. With the advancements in technology, chemical synthesis techniques are being developed to control nanoparticles with precision, allowing the discovery of new functional materials with unique properties. Teranishi's team at Kyoto University has recently made an important breakthrough by discovering a new behavior of crystal structure transformation in an ionic nanocrystal [1]. Moreover, the team was able to synthesize a new $Z3$-type Fe(Pd, In)$_3$ crystal structure by introducing indium as a third element into $L1_2$-FePd$_3$, which could have significant implications for the development of new technologies [2]. The discovery of these new materials is critical for advancements in various fields such as medicine, energy, electronics, etc.

In this report, we have conducted first-principles calculations to explore the stability of compounds with $Z3$-type structures. Our research aimed to estimate the formation energies for various $Z3$-Fe(Pd, $M$)$_3$ structures, where $M$ represents different transition metals. To perform these calculations, we utilized the ab-initio code, OpenMX [3], to compute the ground states of $L1_2$-(Fe, $M$)Pd$_3$ and $L1_2$-(Fe, $M$)Pd$_3$ structures. We compared the energies obtained to analyze the stability of these structures. Our results indicated that some $Z3$-type structures exhibit lower energies compared to the $L1_2$-type structures, indicating that they could be synthesized experimentally. Further theoretical investigations are required to explain the coercivity mechanism in the $Z3$-Fe(Pd, $M$)$_3$ structures.

## References

[1] Z. Li, M. Saruyama, T. Asaka, Y. Tatetsu, and T. Teranishi, Science, **373**, 332 (2021).

[2] K. Matsumoto *et al.*, Nat. Commun., **13**, 1047 (2022).

[3] http://www.openmx-square.org

# Machine Learning Based Optimized Polymer for Thermal Function Materials

Bin XU

*Department of Mechanical Engineering,*

*The University of Tokyo, 7-3-1, Hongo, Bunkyo-ku, Tokyo 113-8656*

Polymer informatic is an emerging filed where the AI and machine learning are being used in the efficient discovery and design of polymer with target properties and has large impact on several aspect of human life, science, and technology. Cellulose is an organic compound with the formula $(C_6H_{10}O_5)_n$, a polysaccharide consisting of a linear chain of several hundred to many thousands of β linked D-glucose units. Cellulose is an important structural component of the primary cell wall of green plants, many forms of algae and the oomycetes. In this work, we applied the molecular dynamics simulation in combination with the machine learning to explore the effect of strain, hydrogen bonds, and structure ordering on thermal transport in cellulose. The structure for the simulation is shown in Fig. 1.

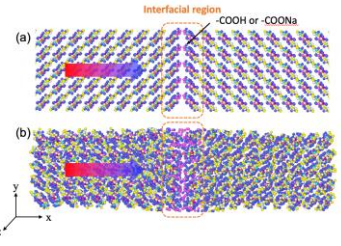


Figure 1 Schematic illustration of structure used for non-equilibrium molecular dynamics simulation.

The temperature dependent thermal conductivity of cellulose polymer with the temperature up to 300 K is shown in Fig. 2. The thermal conductivity of filaments with lower crystallinity index (CI) also increases with a similar slope until 240 K, but then saturates to a constant value until 300 K. Temperature-dependence thermal conductivity reveal that the filaments exhibit phonon transport at effective dimension between 2D and 3D.

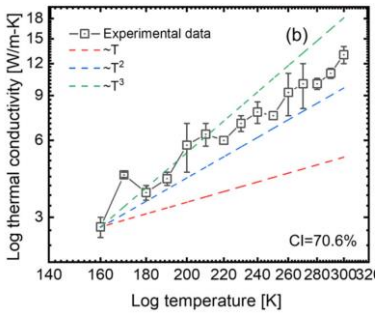


Figure 2 temperature dependent thermal conductivity of cellulose nanofiber.

## References

[1] Mu, Fengwen, **Bin Xu**, Xinhua Wang, Runhua Gao, Sen Huang, Ke Wei, Kai Takeuchi et al. Journal of Alloys and Compounds **905** 164076 (2022).

[2] Wang, G., Kudo, M., Daicho, K., Harish, S., **Xu, B**., Shao, C., Lee, Y., Liao, Y., Matsushima, N., Kodama, T. and Lundell, F., Nano Letters, **22**, 8406-8412 (2021).

# Theoretical study of quantum effects in nanographene devices

Koichi KUSAKABE
*Graduate School of Science, University of Hyogo*
*Kouto, Kamigori, Hyogo 5-8581*

## 1 Introduction

New quantum devices for quantum information and quantum electronics are being developed by exploring various quantum effects. We are studying graphene-based quantum computation resources,[1] and graphene-based spin-electronic devices.[2, 3] We have developed theoretical approaches to study stubility of adsorbed molecules on graphene in solvents,[4] acceleration methods utilizing evolutionary algorithms,[5] and light-induced structural transformation of nanomaterials.[6]

## 2 Quantum computation resources by poly-PTM

The design of a hydrogenated poly-PTM measurement-based quantum computation resources was promoted by evaluating decice behavior based on proton NMR simulations on adsorbed hydrogen on the poly-PTM. The design of a two-dimensional $S = 3/2$ antiferromagnetic Heisenberg system was promoted based on the design of a two-dimensional honeycomb poly-PTM network. We concluded that possible computational resource states in a two-dimensional hydrogenated nanographene requires control of the effective many-body interaction between localized spins.

## 3 Stability and functions of nanographene devices

The structural stability of hydrogenated nanograpehe structures was evaluated, as well as the activation energy barrier heights on the hydrogen diffusion path. To evaluate decoherence, which is the central concern of quantum information operation, we developed a theory of spin-current-rotation coupling and the effect of inserting insulating hBN between metallic Ni substrate and graphene. We concluded that control of the decoherence process requires the control of the interaction between electron spins and current rotation.

## Acknowledgement

The author acknowledges the big contributions of Dr. N. Morishita, Mr. K. Komatsu, and Prof. M. Kitatani on nanographene quantum computation resorces. He also thanks Dr. Y. Wicaksono, Ms. H. Harfah, Dr. G. K. Sunnardianto, and Prof. M. A. Majidi for collaboration on graphene quantum spintronics devices, and all collaborators for theoretical approaches to nanomaterial device structures.

## References

[1] N. Morishita, Y. Oishi, T. Yamaguchi, K. Kusakabe, Appl. Phys. Express **14**, 121005 (2021).

[2] Y. Wicaksono, H. Harfah, G. K. Sunnardianto, M. A. Majidi, and K. Kusakabe, RSC Adv., **12**, 13985 (2022).

[3] Y. Wicaksono, H. Harfah, G. K. Sunnardianto, M. A. Majidi, and K. Kusakabe, Magnetochem. **9**, 113 (2023).

[4] Y. Oishi, H. Ogi, S. Hagiwara, M. Otani, and K. Kusakabe, ACS Omega, **7**, 35, 31120 (2022).

[5] T. Ishikawa, K. Kusakabe, Y. Makino, S. Sakamoto, N. Okuyama, J. Phys. Chem. A, **126**, 8082 (2022).

[6] M. Nagai, Y. Higashitani, M. Ashida, K. Kusakabe, H. Niioka, A. Hattori, H. Tanaka, G. Isoyama, N. Ozaki, Commun. Phys., in press (2023).

# Electrochemical reaction analysis using density functional calculation + implicit solvation model 3

Jun HARUYAMA

*Institute for Solid State Physics,*

*The University of Tokyo, Kashiwa-no-ha, Kashiwa, Chiba 277-8581*

We have studied $H_2O$ adsorption monolayer on Pt(111). The understanding of this metal/water interface system is important for basic electrochemical reactions such as the oxygen reduction reaction. This year, we focused on the calculation method for the second-order nonlinear susceptibility $\chi^{(2)}$ in this system.

Fig. 1a shows the most stable adsorption monolayer structure, √39×√39 cell including 5- and 7-membered rings on Pt(111). By employing the density functional perturbation theory combined with the effective screening medium [1] + explicit electric field approach, we obtained $\chi^{(2)}_{zzz}$ as shown in Fig. 1(b). [2] The negative and positive signs of Im $\chi^{(2)}_{zzz}$ in the high (3000–3500 $cm^{-1}$) and low (600 –2400 $cm^{-1}$) frequency regions, respectively, were obtained. The spectra show negative double peaks in the high-frequency region, consistent with those obtained by heterodyne-detected sum-frequency generation spectroscopy. [3] The peaks at approximately 2000–3500, 1600, and 600–1200 $cm^{-1}$ are composed of the OH stretching, $H_2O$ bending, and $H_2O$ libration modes, respectively. This study provides a fundamental basis for structure analysis of $H_2O$ adsorption on metal surfaces.

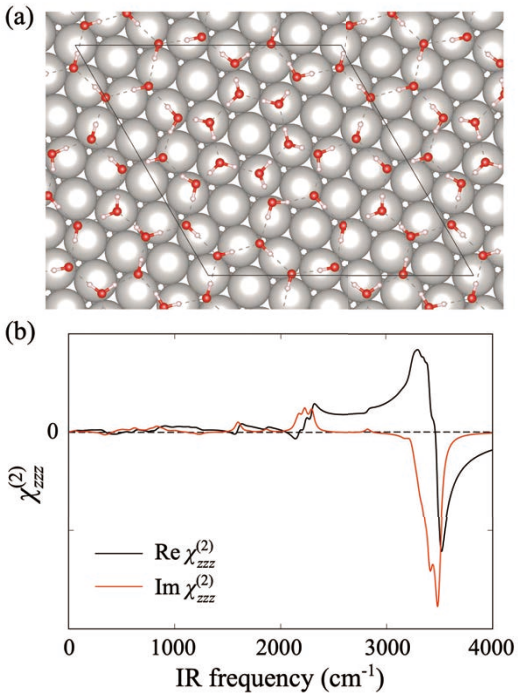


Fig. 1: (a) $H_2O$ adsorption monolayer structure. (b) Second-order nonlinear susceptibility $\chi^{(2)}_{zzz}$.

## References

[1] M. Otani and O. Sugino: Phys. Rev. B **73** (2006) 115407.

[2] J. Haruyama, T. Sugimoto, and O. Sugino, *submitted.*; https://isspns-gitlab.issp.u-tokyo.ac.jp/j-haruyama/Pt111_H2O-monolayer

[3] T. Sugimoto and Y. Matsumoto, Phys. Chem. Chem. Phys. 22, 16453 (2020).

# Discovery of Fast Anhydrous Proton Conduction in $\alpha$-$MoO_3$

Atsuo YAMADA

*Department of Chemical System Engineering,*

*The University of Tokyo, Bunkyo-ku, Hongo, Tokyo 113-8656*

Aqueous proton batteries show potential as high-power energy storage devices because of the small size of the protons and their high mobility in aqueous solutions. Among various transition metal oxides, orthorhombic $MoO_3$ ($\alpha$-$MoO_3$) is one of the most promising proton hosts with fast kinetics and large capacities. Herein, we investigated the mechanism of proton intercalation and transportation in $\alpha$-$MoO_3$ based on theoretical calculations [1].

The spin-polarized DFT calculation was adopted to trace the $H^+$ dynamics in $\alpha$-$MoO_3$ with VASP program. Based on a 2 × 1 × 2 supercell ($Mo_{16}O_{48}$), a series of H-intercalated structures of $H_xMoO_3$ ($0 \le x \le 3.0$) was calculated. The CI-NEB method was used to calculate proton diffusion pathways.

The energy profiles of $H^+$ diffusion in $MoO_3$ are shown in Fig. 1. At the early stages of protonation and deprotonation, the activation barriers for proton diffusion between the oxygen arrays of $MoO_3$ were below 0.4 eV, which is comparable to that of Grotthuss mechanism in water. Therefore, further exploration of other host materials with dense and continuous oxygen arrays capable of fast anhydrous proton conduction is an important challenge for the practical application of high-power aqueous proton batteries.

## References

[1] Z. Ma, X. M. Shi, S. Nishimura, S. Ko, M. Okubo, A. Yamada, *Adv. Mater.*, **34**, 2203335 (2022).

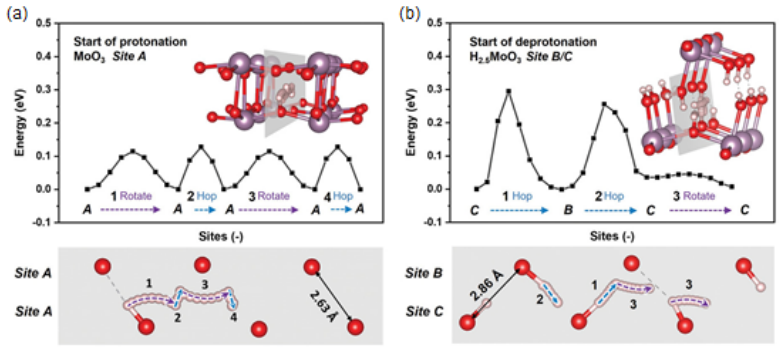


**Figure 1** Anhydrous proton transport via hydrogen bond network and corresponding energy barriers at the early stages of protonation (a) and deprotonation (b). The three most stable $H^+$ absorption sites in $MoO_3$ are labeled as A, B, and C, respectively.

# First-principles prediction of anomalous Hall effect in antiferromagnetic perovskites

Kunihiko Yamauchi

*Department of Precision Engineering, Graduate School of Engineering, Osaka University, 2-1 Yamadaoka, Suita, Osaka 565-0871*

Recently, large anomalous Hall conductivity in noncollinear antiferromagnetic (AFM) systems has been recently observed and attracted much attention while the anomalous Hall effect takes place typically in ferromagnetic (FM) materials with the finite magnetization.

In this study, by using DFT calculation, we predict the anomalous Hall effect (AHE) in perovskite $CaCrO_3$ as a representative of collinear antiferromagnetic materials [1]. We showed that the C-type AFM ordering (Fig. (a)) generates the sizable anomalous Hall conductivity and revealed two essential roles of the non-symmorphic *Pbnm* symmetry. (i) The screw and glide symmetry operations bind the AFM and FM order parameters in the same irreducible representation so that AHE is active in the AFM order. (ii) The band-sticking effect at the Brillouin-zone surface makes Cr-$t_{2g}$ state form the narrow bands near the Fermi energy; a couple of those bands cause anticrossing and enhancement of the Berry curvature (Fig. (b)).

In this year, we also studied 2D magnetism as reported in Ref. [2] and [3] in collaboration with theoretical and experimental groups in Italy and Germany.

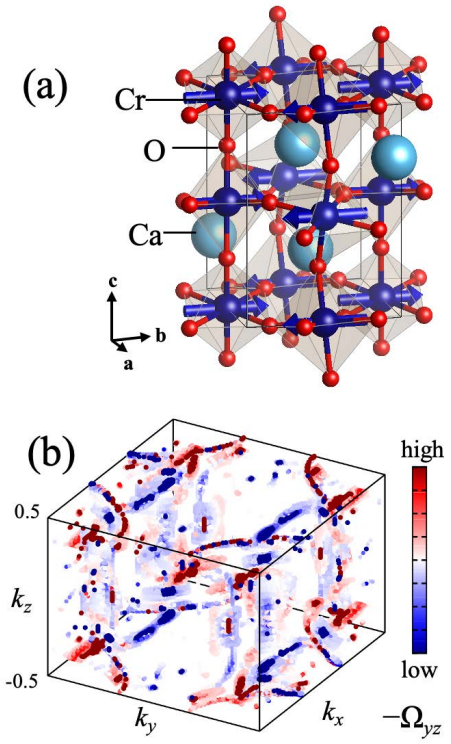


Figure: (a) C-type AFM ordering in *Pbnm* crystal structure of $CaCrO_3$. (b) Berry curvatures in the orthorhombic Brillouin zone.

## References

[1] Thi Phuong Thao Nguyen and Kunihiko Yamauchi, Phys. Rev. B. **107**, 155126 (2023).

[2] A. D. Vita, T. T. P. Nguyen, .., K. Yamauchi, *et al.*, Nano Letter **22**, 7034 (2022).

[3] K. Riedl, .., T. T. P. Nguyen, K. Yamauchi, *et al.*, Phys. Rev. B **106**, 035156 (2022).

# Ab-initio electron dynamics simulation for nonlinear optical phenomena in solids

Shunsuke SATO

*Center for Computational Sciences*

*University of Tsukuba, Tsukuba, Ibaraki 305-8577, Japan*

We have studied light-induced electron dynamics in solids based on the time-dependent density functional theory. This year, we focused on the development of a novel analysis technique for light-induced linear and nonlinear optical phenomena in solids based on the time-dependent current density [1]. Here, we first compute the time-dependent current density as

$$\boldsymbol{j}(\boldsymbol{r},t) = -\frac{e}{\Omega \mathrm{m_e}} \int_{FBZ} d\boldsymbol{k} \sum_b f_{b\boldsymbol{k}} \times \psi^*_{b\boldsymbol{k}(\boldsymbol{r},t)}\big(\boldsymbol{p}+\boldsymbol{A}(t)\big)\, \psi_{b\boldsymbol{k}}(\boldsymbol{r},t), \quad (1)$$

where $\psi_{b\boldsymbol{k}}(\boldsymbol{r},t)$ are time-dependent Kohn-Sham orbitals, and $\boldsymbol{A}(t)$ is the vector potential that is related to the applied external electric field as $\boldsymbol{A}(t) = -\int^t dt' \boldsymbol{E}(t')$. By applying Fourier transform to the computed current density in Eq. (1), we obtain the frequency-resolved microscopic current density as

$$\tilde{\boldsymbol{j}}(\boldsymbol{r},\omega) = \int dt\, e^{i\omega t} \boldsymbol{j}(\boldsymbol{r},t). \quad (2)$$

The frequency-resolved microscopic current density contains the atomic scale real-space information of light-induced linear and optical phenomena. In Ref. [1], we demonstrated that the developed current-density analysis captures microscopic insight into optical phenomena in both delocalized and bound electrons in solids. We further plan to apply the developed method for the investigation of nonlinear optical phenomena in solids in order to develop the microscopic interpretation of perturbative and nonperturbative nonlinear phenomena.

In addition to the development of the above theoretical scheme, we have studied transient optical properties of solids under the presence of intense femtosecond laser fields. For the investigation of nickel, we analyzed the light-induced spin-dynamics and transient absorption based on the pump-probe technique, and we found that the local spin-density dynamics causes the change of the photoabsorption around the absorption edge. Based on this finding, we further proposed the attosecond spin-dynamics spectroscopy to investigate the element-specific light-induced spin-dynamics in the attosecond time-scale.

## References

[1] Shunsuke A. Sato, “"Frequency-resolved microscopic current density analysis of linear and nonlinear optical phenomena in solids", arXiv:2302.05859 [cond-mat.mtrl-sci].

# First-principles study on the structure of water/graphene interfaces depending on the number of graphene layers

Tatsuhiko OHTO

*Graduate School of Engineering Science,*

*Osaka University, 1-3 Machikaneyama, Toyonaka, Osaka 560-8531*

Ab initio molecular dynamics (AIMD) simulation is a powerful tool to describe heterogeneous systems such as the water/solid interface. Although AIMD is computationally expensive, it describes electronic states beyond classical force fields,[1] which is important for interfacial structures.

We have simulated sum-frequency generation (SFG) spectra of isotopically diluted water at the water-graphene sheet interfaces using ab initio molecular dynamics simulations, with changing the number of the graphene layers from one to three. The simulation of water-single graphene interface has already been performed using ISSP.[2] A sharp 'dangling' O-D peak around ~2640 cm-1 appearing in simulated SFG spectra evidences that graphene is hydrophobic. Although the results obtained so far are still preliminary, the dangling O-D peak is blue-shifted by increasing the number of the graphene layer. This frequency difference manifests a weaker O-D…C intermolecular interaction between water and thicker graphene, indicating that graphite is more hydrophobic than graphene.

The simulations were performed using the CP2K code [3]. After obtaining the sufficient length of trajectories, we are going to construct machine learning force field to simulate larger scale interfaces between carbon/water.

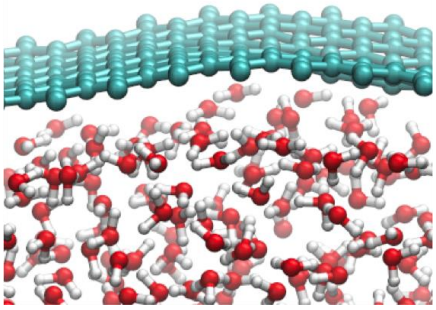

Fig. 1: Structures of the graphene-water interface.

## References

[1] T. Ohto et al. Phys. Chem. Chem. Phys. **19**, 6909 (2017).

[2] T. Ohto et al. Phys. Chem. Chem. Phys. **20**, 12979 (2018)

[3] The CP2K developers group, http://cp2k.berlios.de/

# Multiscale simulations for magnetic materials

Hung Ba TRAN
*Laboratory for Materials and Structures, Institute of Innovative Research, Tokyo Institute of Technology, Midori-ku, Yokohama 226-8503, Japan*

Our previous works have studied the magnetocaloric effect by multiscale simulations. The magnetic parameters, such as magnetic exchange coupling constants $J_{ij}$ and magnetic anisotropy energy, are calculated from first–principles calculations. Then, the Monte-Carlo simulations are performed to estimate the magnetic properties at thermal equilibrium, such as magnetization curves and isothermal magnetic entropy change. Several types of the magnetocaloric effect, such as conventional (direct) magnetocaloric effect, giant magnetocaloric effect, anisotropic magnetocaloric effect, and inverse magnetocaloric effect, can be considered using our in–house program[1, 2, 3, 4, 5, 6].

In our recent works, we consider the spin reorientation effect in $Nd_2Fe_{14}B$ material based on first–principles calculations[7]. $Nd_2Fe_{14}B$ is famous material for permanent magnets that are widely used in power generation, motors, and so on due to the high magnetic anisotropy energy, saturation magnetization, and Curie temperature. However, the material has a problem at low temperatures. It is spin reorientation from the easy axis ($z$–direction) to cone magnetization (where the magnetization is tilted). In previous theoretical works, the spin reorientation in $Nd_2Fe_{14}B$ is usually considered using empirical parameters as crystal–electric field term. In contrast, in this work, we calculate the Dzyaloshinskii–Moriya interactions (DMI) by first–principles calculations for the first time. We found that the DMI is the origin of spin reorientation in $Nd_2Fe_{14}B$. The spin reorientation in $Nd_2Fe_{14}B$ can be reproduced in Figure. 1 (a) by introducing the DMI. In addition, the peak like in magnetic anisotropy energy of experimental work can be

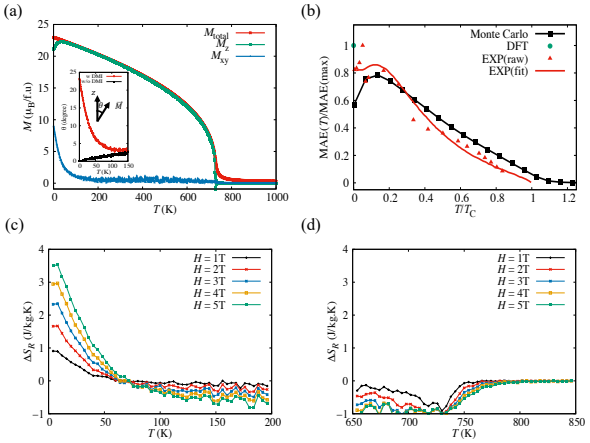


Figure 1: (a) Total (red) and projected spontaneous magnetization in the out–of–plane (green) and in–plane (blue) directions as a function of the temperature of $Nd_2Fe_{14}B$ (inset figure: Temperature dependence of the tilt angle between the magnetization direction and $z$–direction in the case of switching on (red) and switching off (black) the Dzyaloshinskii–Moriya interaction). (b) The magnetic anisotropy energy obtained is based on DFT (green) and Monte Carlo method by integrating the $M$–$H$ curves (black) and experimental raw data (red dots) and that derived from anisotropy constants (continuous red curves). (c) Rotating magnetic entropy change as a function of temperature and the magnetic field around the spin reorientation temperature and (d) Curie temperature.

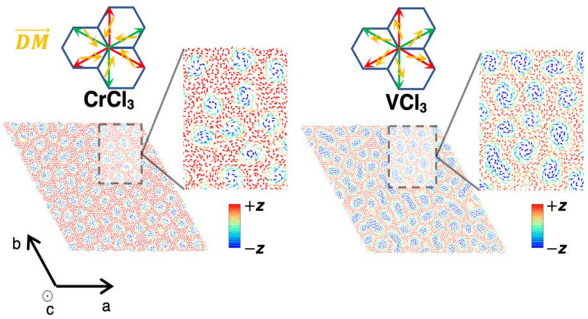


Figure 2: In–plane components of Dzyaloshinskii–Moriya vector for the second nearest neighbor of intra–layer of $CrCl_3$ and $VCl_3$, where the red and green arrows indicate pairs with different sub–lattices, and the yellow arrow indicates the direction of Dzyaloshinskii–Moriya vector. Snapshot of Monte Carlo simulation of $CrCl_3$ at 10 K with external magnetic field equal to 4 T along the positive $z$–direction. Snapshot of the Monte Carlo simulation of $VCl_3$ at 10 K with external magnetic field equal to 6 T along the positive $z$–direction.

reproduced quantitatively, as shown in Figure. 1 (b). The spin reorientation in the material is usually not desirable for the application of a permanent magnet. However, we found that the rotating entropy change around spin reorientation is almost four times higher than at the Curie temperature, as shown in Figure. 1 (c, d) due to the peculiar properties of spin reorientation.

On the other hand, we also consider the skyrmions in van der Waals centrosymmetric $MX_3$ (M: V, Cr, Mn, Fe, Co; X: Cl, Br, I) [8]. Skyrmions usually appear in non–centrosymmetric material due to the DMI lacking inversion symmetry. Although $MX_3$ has space group $R\bar{3}$ being centrosymmetric with honeycomb lattice, the broken local inversion symmetric of the second nearest neighbor of intra–layer stabilizes the finite DMI. It leads to ultra-small skyrmions with a diameter being 2.0 nm, as shown in Figure. 2. In addition, two types of helicity can be realized in $CrCl_3$ and $VCl_3$ due to the nearly opposite direction in Dzyaloshinskii–Moriya vector. Not only skyrmions but also antiferromagnetic skyrmions and meron are observed in $MX_3$.

## References

[1] H. B. Tran, T. Fukushima, K. Sato, Y. Makino, and T. Oguchi, J. Alloys Compd. **854**, 157063 (2021).

[2] H. B. Tran, T. Fukushima, Y. Makino, and T. Oguchi, Solid State Commun. **323**, 114077 (2021).

[3] H. B. Tran, T. Fukushima, H. Momida, K. Sato, Y. Makino, and T. Oguchi, Comput. Mater. Sci. **188**, 110227 (2021).

[4] H. B. Tran, T. Fukushima, H. Momida, K. Sato, Y. Makino, and T. Oguchi, J. Alloys Compd. **926**, 166718 (2022).

[5] H. B. Tran, H. Momida, Y. Matsushita, K. Sato, Y. Makino, K. Shirai, and T. Oguchi, Phys. Rev. B **105**, 134402 (2022).

[6] H. B. Tran, H. Momida, Y. Matsushita, K. Shirai, and T. Oguchi, Acta Mater. **231**, 117851 (2022).

[7] H. B. Tran, Y. Matsushita, Appl. Mater. Today **32**, 101825 (2023).

[8] H. B. Tran, Y. Matsushita, Skyrmions in van der Waals centrosymmetric materials with Dzyaloshinskii-Moriya interactions, arXiv:2209.02333 (2022) (under review).

# Theoretical design of novel functional materials based on abundant elements for energy conversion and storage.

Tetsuya TAKETSUGU
*Faculty of Science, Hokkaido University*
*N10W8, Sapporo, Hokkaido 060-0810*

DFT computations using QuantumEspresso and VASP packages are used to gain physical-chemical insights and to design novel functional materials with abundant elements for energy conversion and storage processes. This helps to reduce costs and dependences on precious metals in energy-related industrial applications.

We have demonstrated that oxygen-functionalized hexagonal boron nitride (h-BN) can be an efficient catalyst for oxidative dehydrogenation (ODH) of light alkanes, specifically ethane ($C_2H_6$), propane ($C_3H_8$), butane ($C_4H_{10}$), and isobutane ($HC(CH_3)_3$) [1]. This is particularly interesting because it is commonly accepted that hexagonal boron nitride is an inert material. However, we have demonstrated that h-BN can be functionalized and serve as an active catalyst. It has been found that the reaction pathway involves two H atom transfer steps with small activation energies. We demonstrate that the synergy of two active sites, *B-O-O-B* and *B-O-B* (Figure 1), is crucial for the first and second H-transfer, respectively. With the increase in molecular mass of the considered light alkanes, the ODH reaction temperature decreases. The charge redistribution during H-transfers and localized oxygen atomic states in the conduction band are explored to suggest possible descriptors for the rational design of new catalysts. The universal action of the *B-O-O-B* and *B-O-B* active sites for ODH of the light alkanes paves the way for metal-free BN-based materials for future catalytic applications.

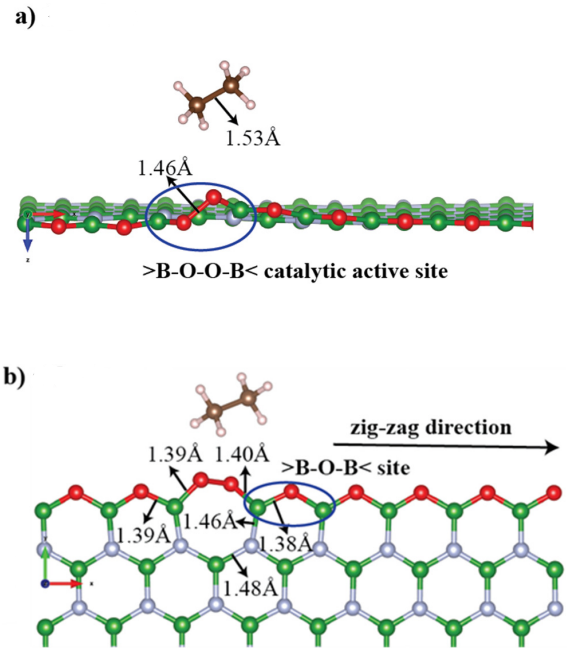


Figure 1: Catalyticaly active (a) *B-O-O-B* and (b) *B-O-B* sites [1].

The multielectron transfer is a key process being indispensable for a wide spectrum of modern electrochemical energy technology. Finding promising multielectron-transfer materials with abundant elements is especially important to advance the present rechargeable battery technology mainly relies on single electron transfer type electrodes. To date,

a few oxide-based materials can reach an electron-transfer number per metal-cation (e) larger than 2 upon a (de)intercalation mechanism. However, these oxide-based electrodes face challenges in improving electrochemical properties as they still suffer from considerable degradation during charge/discharge reactions due to irreversible rearrangements of bonds between metallic cation and anionic oxygen. Furthermore, these high-performance multielectron-transfer oxides are mainly constituted of precious metals. As it is well-known, these elements are limited, and therefore, electrode materials based on precious metals are inappropriate candidates to replace the present cathode materials.

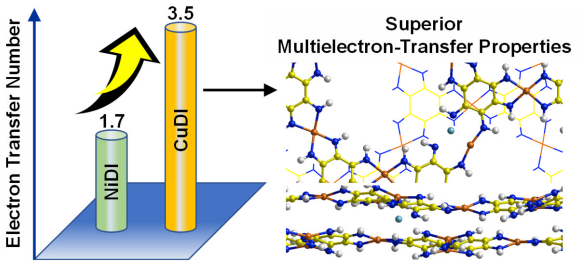


Figure 2: A significantly reversible multielectron-transfer is demonstrated by using only abundant elements [2].

We have demonstrated that the non-oxide electrode based on the bis(diimino)copper framework can show e = 3.5 with cation/anion co-redox mechanism together with a dual-ion mechanism (Figure 2). In this study, the role of the cation-anion interactions has been unveiled by using an experiment/theory collaboration applied to a series of the model non-oxide abundant electrode systems based on different metal-nitrogen bonds. These models provide a route for the design of the multielectron transfer materials based on the tunable $\pi$-d conjugated electronic structures. It is found that the Cu-nitrogen bonds show a unique reversible rearrangement upon Li-intercalation, and this process responds to acquire a significant reversible multielectron-transfer. This work provides new insights into the affordable multielectron-transfer electrodes and uncovers an alternative strategy to advance the electrochemical energy storage reactions.

## References

[1] S. Kumar, A. Lyalin, Z. Huang, and T. Taketsugu, *Catalytic Oxidative Dehydrogenation of Light Alkanes over Oxygen Functionalized Hexagonal Boron Nitride*, ChemistrySelect **7**, e202103795 (2022).

[2] D. Xia, K. Sakaushi, A. Lyalin, K. Wada, S. Kumar, M. Amores, H. Maeda, S. Sasaki, T. Taketsugu and H. Nishihara, *Superior Multielectron-Transferring Energy Storage by $\pi$-d Conjugated Frameworks*, Small **18**, 2202861 (2022).

# Microscopic structure of water/$CeO_2$ interface

Akira NAKAYAMA

*Department of Chemical System Engineering,*

*The University of Tokyo, Tokyo 113-8656, JAPAN*

The structural properties and dynamical behaviors of the interface between water and cerium oxide ($CeO_2$) are investigated by reactive molecular dynamics (MD) simulations employing the neural network potentials (NNP)[1][2] that are trained to reproduce density functional theory (DFT) results. In the construction of the neural network potentials, DFT-based MD (DFT-MD) simulations with enhanced sampling schemes[3] are employed to efficiently acquire training data that include diverse hydrogen-bonding configurations caused by proton hopping events. The water interfaces with three low-index surfaces of (111), (110), and (100) are explored with these neural network potentials, and structure and long-range proton and hydroxide ion transfer dynamics are examined with unprecedented system sizes and long simulation times.

The time step for DFT-MD simulations was set to 1 fs and the temperature was controlled at 360 K. RPBE was used for the DFT functional. The DFT-D3[4] and DFT+U methods was used to incorporate dispersion interaction and electron correlations for Ce 4f electrons, respectively. *k*-point sampling was performed at Γ points only. CP2K was used for DFT-MD calculations. For each interface, a slab model was created with a surface size of $p(4\times4)$ and a water thickness of 30 Å. The conventional and enhanced sampling DFT-MD methods were performed for 20 ps, yielding a total of 8000 configurations as training data.

We mainly discuss the results for the water/$CeO_2$(110) interface. The *z*-axis projection of the density distribution of O and H atoms on the $CeO_2$ surface and in the first hydration layer obtained from the NNP-MD simulations is shown in Figure 1. Note that the average position of the topmost Ce atoms is set to $z$ = 0 Å. The large-scale and long-time simulations provide sufficient statistics to analyze the interface structure in more detail compared to previous studies.

The mechanism of proton transfer occurring at the water/$CeO_2$(110) interface is then analyzed. Proton transfer can be roughly divided into surface proton transfer (SPT), in which proton transfer occurs between a water molecule coordinated on a Ce atom and a surface $O_S$ atom, and adlayer proton transfer (APT), in which proton transfer occurs between a water molecule and hydroxide ion coordinated on a Ce atom. The proton transfer

between surface species is further classified into direct and indirect transfer that involves neighboring water molecules.

At the water/$CeO_2$(110) interface, a total of 863 proton transfers were observed during 4 ns of trajectory, when thermal equilibrium is considered to have been reached. Table 1 shows the observed ratio of each proton transfer. Since the structure of the $CeO_2$(110) surface is not symmetric with respect to the *x*-axis and *y*-axis directions, the APT were also classified according to whether the proton transfer occurred in the *x*- or *y*-axis direction.

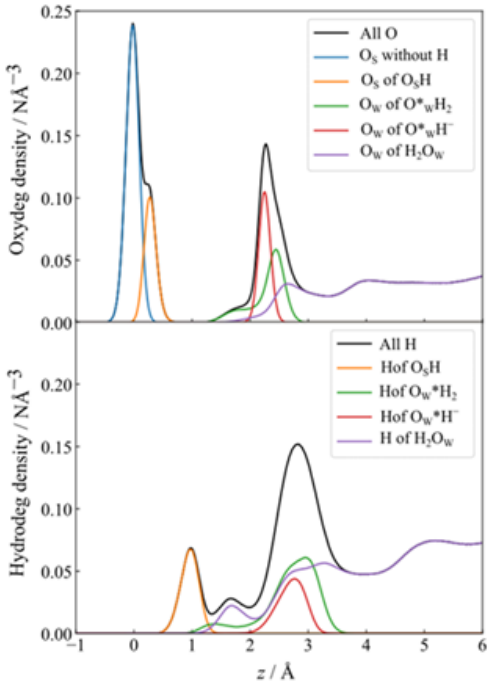


Fig. 1: Density profiles of oxygen and hydrogen at the water/$CeO_2$(110) interface.

As seen, APT occurred more frequently than SPT, possibly because the distance between surface O atoms is closer. H atoms bonded to surface O atoms are stabilized by forming hydrogen bonds with neighboring surface O atoms, thus making SPT less likely to occur. In addition, more migration was observed in the *y*-direction since the distance between surface Ce is closer.

In summary, we have generated training data using DFT-MD calculations with enhanced sampling scheme and constructed NNPs for the water/$CeO_2$ interface. Using the constructed NNPs, we performed large-scale and long-time simulations and obtained the detailed information on the structure and proton transfer mechanisms near the interface, which were difficult to obtain using the conventional DFT-MD simulations.

Table 1: Proton hopping machanims

| プロトン移動機構 | | 割合 |
|---|---|---|
| APT direct | x direction | 13.2% |
| | y direction | 25.6% |
| APT indirect | x direction | 6.3% |
| | y direction | 18.2% |
| SPT direct | Forward | 0.8% |
| | Backward | 0.9% |
| SPT direct | Forward | 13.0% |
| | Backward | 12.4% |
| Others | | 9.4% |

## References

[1] J. Behler and M. Parrinello, Phys. Rev. Lett. **98**, 146401 (2007).

[2] J. Behler, J. Chem. Phys. **145**, 170901 (2016).

[3] L. Maragliano and E. Vanden-Eijnden, Chem. Phys. Lett. **426**, 168 (2006).

[4] S. Grimme, J. Antony, S. Ehrlich, and H. Krieg, J. Chem. Phys. **132**, 154104 (2010).

# Prediction of properties of organic ferroelectrics and piezoelectrics by first-principles calculation

Shoji ISHIBASHI
*National Institute of Advanced Industrial Science and Technology (AIST)*
*Tsukuba, Ibaraki 305-8568*

Many azole compounds such as imidazoles and tetrazoles contain polar and bistable hydrogen-bonded molecular sequences suitable for ferroelectricity or antiferroelectricity. In this study, we have computationally investigated relative stabilities of possible ferroelectric (FE) and antiferroelectric (AFE) phases in eight azole compounds: 5-(4-aminophenyl)-1H-tetrazole (APHTZ), 5-(4-fluorophenyl)-1H-tetrazole (FPHTZ), 5-(4-chlorophenyl)-1H-tetrazole (CPHTZ), 5-(4-methylphenyl)-1H-tetrazole (MPHTZ), 5-phenyl-1H-tetrazole (PHTZ), 2-phenyl-1H-imidazole (PHIM), 2,4,5-tribromo-1H-imidazole (TBIM), and 2-bromo-4,5-dimethyl-1H-imidazole (DM-BIM) [1].

The Perdew-Burke-Ernzerhof (PBE) version of the generalized gradient approximation (GGA) [2] was used to describe the electronic exchange-correlation energy. Starting from the experimental structures, the atomic positions were optimized. The convergence criterion was set to $5 \times 10^{-5}$ Ha/bohr for the maximum force. All the calculations were performed using the QMAS code based on the projector augmented-wave method [3] and the plane-wave basis set.

The obtained results are shown in Fig. 1 together with schematic illustrations of various states in a zero field based on the polarization hysteresis experiments as well as the structural analyses. It is confirmed that the computational and experimetal results are consistent with each other.

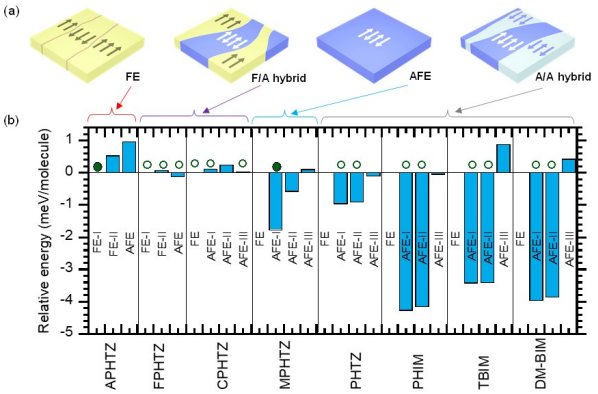


Figure 1: Ferroelectric (FE), antiferroelectric (AFE), and phase-coexisting (F/A hybrid and A/A hybrid) states in the PHTZs crystals. (a) Schematic illustrations of various states in a zero field. (b) Energy histogram of the candidate H-ordered states relative to each FE (or FE-I) form. Filled and open circles point to the non-degenerate and nearly degenerate ground states, respectively (S. Horiuchi, H. Minemawari, and S. Ishibashi, Mater. Horizons, Advance Article (2023), DOI: 10.1039/d2mh01530g).

## References

[1] S. Horiuchi, H. Minemawari, and S. Ishibashi, Mater. Horizons, Advance Article (2023).

[2] J.P. Perdew, K. Burke, and M. Ernzerhof, Phys. Rev. Lett. **77**, 3865 (1996).

[3] P. E. Blöchl, Phys. Rev. B **50**, 17953 (1994).

# Ab initio calculation for transition-metal-oxide interface

Kazuma NAKAMURA
*Quantum Physics Section, Kyushu Institute of Technology*
*1-1 Sensui-cho, Tobata, Kitakyushu, Fukuoka, 804-8550*

In the present study, we investigate electronic structures of interfaces and surfaces of transition-metal oxides using first-principles calculations based on density functional theory. In material science, important physical properties often occur at the surfaces and interfaces of materials. Currently, it is possible to predict physical and chemical properties of the surfaces and interfaces by using *ab initio* electronic structure calculations. On the other hand, since the size of systems including the surface and interface becomes large, and complicated problems such as the generation of an artificial electric field in the surface system are known to occur, so it is necessary to accumulate detailed know-how to perform stable *ab initio* calculations.

Here, we focus on a representative oxide interface system of $SrTiO_3/SrVO_3$ (STO/SVO) hetero structure, and study its microscopic electronic structure and optical properties in details. The STO/SVO system is a fascinating system realizing a metal-insulator transition at the interface [1, 2], especially small thickness of SVO block. In this study, we analyzed this system with *ab initio* calculations, particularly focusing on optical spectra.

We performed *ab initio* self-consistent pseudopotential calculations in which wavefunctions were expanded in a plane-wave basis [3]. We employed norm-conserving pseudopotentials, and the generalized-gradient approximation for exchange-correlation energy. The cutoff energies for the wavefunction and charge density are 100 Ry and 400 Ry, respectively. The atomic geometry was fully optimized with kept at inplane lattice constant $a = 3.9451$ Å, where the force on each ion were relaxed to less than 0.001 a.u. and a Monkhorst-Pack $k$-grid of $10\times10\times2$ was employed. Optical calculations were performed with using RESPACK [4]: The energy cutoff for the polarization function was set to 3 Ry. The total number of bands considered in the polarization calculation was determined to cover unoccupied states up to 10-15 eV above the Fermi level. The integral over the Brillouin zone was calculated with the generalized tetrahedron technique with a smearing of 0.01 eV.

Figure 1 shows our structure models to be analyzed, where we consider a multilayer model consisting of SVO and STO blocks [panel (a)] and a symmetric slab model [(b)]. The slab model includes a vacuum region with 20 Å, and has a mirror symmetry with respect to the central $TiO_2$ plane. Then, artificial electric fields due to asymmetry in the both ends of the slab do not occur. The structural models include several SVO blocks, where we specify the number of the blocks as $n$. In the present study, we consider the structural models until $n = 4$. The number of the STO blocks was fixed to 5 for the multilayer and 8.5 for the slab (0.5 indicates an additional central $TiO_2$ layer).

Figure 2 shows our calculated band structures of the multilayer (a) and slab (b), where the band diagrams for the $n = 2$ model are

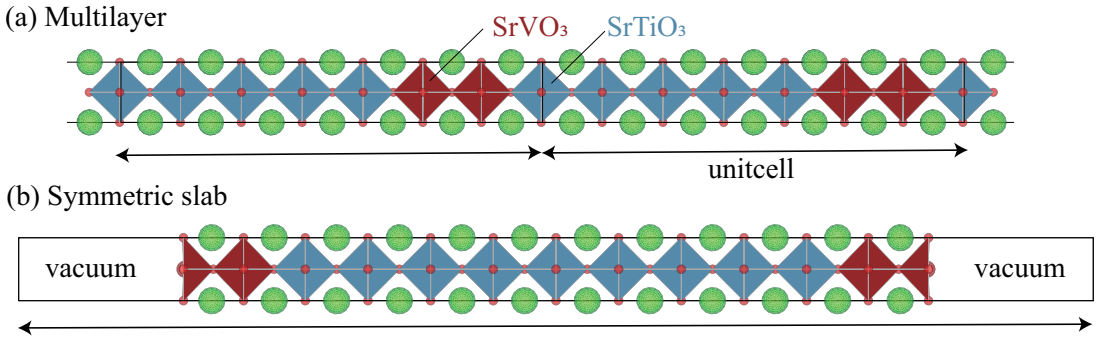


Figure 1: Two structural model: (a) Multilayer consisting of $SrTiO_3$ and $SrVO_3$ blocks. (b) Symmetric slab having a mirror symmetry with respect to the center $TiO_2$ plane.

displayed. From the band structures, we see that both two systems are metal; the SVO $t_{2g}$ bands cross the Fermi level, and the STO $t_{2g}$ band is about 1 eV above from the Fermi level.

Figures 2(c) and (d) show our calculated reflectance spectra for the multilayer and slab models, respectively. We see that the both spectra exhibit a lowering of the plasma edge compared to the bulk SVO one. We also see the appreciable $n$ dependence of the plasma edge. The difference between the multilayer and slab results seems to be small.

In summary, we have calculated electronic structures and reflectance spectra of the STO/SVO system from first principles. In the experiments, the system is insulator at small thickness of the SVO blocks, and this origin should be further investigated from view of strongly correlation physics. To this end, we need to perform *ab initio* derivations of the low-energy model of SVO-$t_{2g}$ bands near the interface, which leaves as a next step.

[1] D. H. Kim, *et al.*, Solid State Commun. 114, 473 (2000).

[2] K. Yoshimatsu, *et al.*, Phys. Rev. Lett. 104, 147601 (2010).

[3] P. Giannozzi, *et al.*, J. Phys. Condens. Matter 29, 465901 (2017).

[4] K. Nakamura, *et al.*, Comput. Phys. Commun. 261, 107781 (2021).

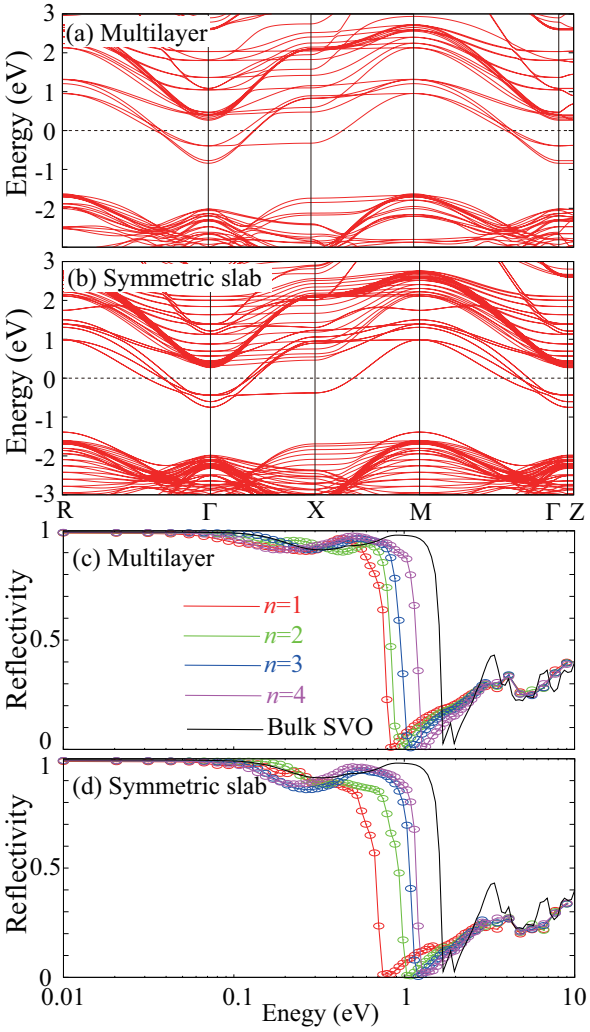


Figure 2: Our calculated band structures of (a) multilayer and (b) slab model where we show $n = 2$ case. Panels (c) and (d) show our calculated reflectance spectra of multilayer and slab models, respectively.

# Two-color mixing enhancement of nonlinear optical absorption for a semiconductor

Yasushi SHINOHARA[1,2], and Mizuki TANI[3]

[1]*Photon Science Center,*

*The University of Tokyo, Hongo, Bunkyo-ku, Tokyo 113-8656.*

[2]*NTT Basic Research Laboratories,*

*NTT Corporation, 3-1 Morinosato Wakamiya, Atsugi, Kanagawa 243-0198.*

[3]*Department of Nuclear Engineering and Management*

*The University of Tokyo, Hongo, Bunkyo-ku, Tokyo 113-8656.*

We have theoretically studied dielectrics exposed to strong laser fields using a first-principles theoretical framework based on time-dependent density-functional theory (TDDFT) within SALMON-TDDFT [1]. The real-time solution of the time-dependent quantum system is one of the most accurate schemes to evaluate nonlinear optical responses that perturbative expansions cannot describe.

One of the most prominent features of the nonpertubative response of the material is the complex mixing of multiple frequencies of an applied field. We do not have a simple formula to model the response written as a combination of amplitudes depending on the frequency of the field, i.e., the Fourier component of the field, in contrast to simple power expansion within the perturbation theory. We need a theoretical description capable of nonperturbative responses to evaluate the response.

We have performed TDDFT simulations for energy absorption of Si crystals exposed to strong laser field that has two color components, 1.6 eV, and 3.2 eV [2]:

$$E(t) = f(t)\left[E_{1.6\ \mathrm{eV}}\cos\left(\frac{1.6\ \mathrm{eV}}{\hbar}t\right) + E_{3.2\ \mathrm{eV}}\cos\left(\frac{3.2\ \mathrm{eV}}{\hbar}t\right)\right],$$

where $f(t)$ is an envelope function that has 14.4 fs full-width-half-maximum. The second color, 3.2 eV, is slightly above the direct gap of the crystal. To model an experimental setup of frequency conversion for 3.2 eV from 1.6 eV via second harmonic generation, we change the relative power ratio such that the sum of two components is kept constant:

$$I_{\mathrm{tot}} = I_{1.6\ \mathrm{eV}} + I_{3.2\ \mathrm{eV}},$$

$$I_i = \frac{1}{2}\epsilon_0 c|E_i|^2, i = 1.6\ \mathrm{eV}, 3.2\ \mathrm{eV},$$

where $\epsilon_0$ and $c$ are the vacuum permittivity and the speed of light. The criteria of nonperturbative response based on the Keldysh

parameter [3] is 6.91 TW/cm$^2$ and 27.2 TW/cm$^2$ for 1.6 eV and 3.2 eV. The absorbed energy is evaluated by the total work from the field to the system

$$E_{\mathrm{abs}} = \int_0^{\infty} \mathrm{d}t\, \boldsymbol{J}(t) \cdot \boldsymbol{E}(t)$$

where $\boldsymbol{J}(t)$ is the induced charge current evaluated by TDDFT.

Our simulation shows maximal energy absorption is realized by a condition $I_{1.6\ \mathrm{eV}}/I_{3.2\ \mathrm{eV}} \sim 1.0$, when we have $I_{\mathrm{tot}} = 1\ \mathrm{TW/cm^2}$. This fact is hardly explained by perturbative expansion because the lower-order nonlinear response is expected to dominate the dynamics for such weak intensity compared to the atomic unit value of 35 PW/cm$^2$. The perturbative expansion predicts $I_{1.6\ \mathrm{eV}}/I_{3.2\ \mathrm{eV}} \sim 0.0$ for the maximal absorption condition.

This nontrivial maximal energy absorption mixing ratio appears for other combinations (0.2 eV, 3.2 eV), (0.8 eV, 3.2 eV). This generic behavior is explained by energy detuning due to the lower frequency components with the strong resonant excitation due to the 3.2 eV component. When the lower frequency component does not exist, 3.2 eV component cause Rabi oscillation because of the strong field. Rabi oscillation leads to saturation of absorption in a pulse. By the lower frequency driving for intraband motion, a resonant point undergoes off-resonant condition by the detuning. Then another off-resonant state becomes resonant. This sequence avoids saturation, and the number of excited electrons increases with the two-color mixture for the driving field.

## References

[1] https://salmon-tddft.jp/, M. Noda, S.A. Sato, et al., Computer Physics Communications. **235**, 356 (2019).

[2] Mizuki Tani, Kakeru Sasaki, Yasushi Shinohara, and Kenichi L. Ishikawa, Phys. Rev. B **106**, 195141 (2022).

[3] L. V. Keldysh, Sov. Phys. JETP **20**, 1307 (1965).

# First-principles calculations of complex metallic alloy surfaces

Kazuki NOZAWA
*Department of Physics and Astronomy, Kagoshima University*
*1-21-35, Korimoto, Kagoshima 890-0065*

High-resolution transmission electron microscopy experiments observed the formation of small ZnO patches on the PdZn(111) surface during the methanol steam reforming reaction, indicating the ZnO patches plays an important role in the $CO_2$ selectivity of this catalyst [1]. Last year we obtained an oxidized PdZn(111) surface having a distorted hexagonal Zn-O structure at the top layer [2]. In this fiscal year, we studied the dehydrogenation of water on this oxidized PdZn(111) surface. Calculations are performed with VASP program package as flat MPI jobs on system B and C.

Because the obtained Zn-O layer on the oxidized PdZn(111) surface is corrugated as shown in the figure, first we calculated the potential energy surface (PES) of water with fixing atomic positions to find out promising candidates for the starting structure of the structural relaxation. We investigated the PES for water with its molecular plane parallel and perpendicular to the surface, keeping the distance to the nearest surface atom at 2.0 and 2.5 Å. Many of these calculations were done as bulk jobs on system B. Next, we performed structural relaxation from 20 stable starting structures obtained. We performed similar calculations for the hydroxyl and hydrogen on the same surface to determine the stable coadsorption structure. The stable adsorption site of water was found on a Zn atom forming the hexagonal Zn-O ring. The obtained adsorption energy of water was larger than that on the non-oxidized PdZn(111) surface but smaller than that on ZnO(0001) surface [3]. However, the coadsorption energy of hydroxyl and hydrogen obtained in this calculation was larger than that on the non-oxydized PdZn(111) surface [3]. It means this surface is not active for the hydrogenation of water.

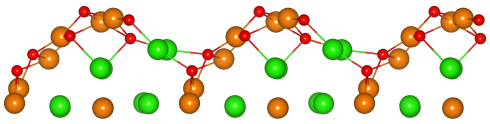

Figure 1: Side view of the oxidized PdZn(111) surface.

In addition to the above work, we studied pentacene adsorption on the twofold surface of the icosahedral Ag-In-Yb quasicrystal [4] and the electronic structure of trace (Pt, Ni, Pd)-doped $Al_{13}Fe_4$ intermetallic compounds.

## References

[1] M. Friedrich *et al.*, Angew. Chem. **52**, 4389 (2013).

[2] K. Iwamura, Master Thesis (Kagoshima University, 2023).

[3] G. K. Smith *et al.*, Surf. Sci. **605**, 750 (2011).

[4] M. Sato *et al.*, J. Phys.:Conf. Ser., **2461**, 012016(2023).

# Adsorption States of Oxygen on Pt Nanoparticles

Takehiko SASAKI and Yasumasa IMAI

*Department of Complexity Science and Engineering, Graduate School of Frontier Sciences, The University of Tokyo, Kashiwa-no-ha, Kashiwa, Chiba 277-8561*

The surface state of the catalyst platinum nanoparticles determines the performance of polymer electrolyte fuel cells (PEFC). Characterization of the electrochemical cycle and oxygen adsorption state on the surface of platinum nanoparticles, as well as the high-coverage oxygen adsorption state with subsurface oxygen generation, has been investigated using synchrotron radiation transient response XAFS and resonant inelastic X-ray scattering (RIXS). Although computational studies on oxygen species on Pt surfaces have been published [1,2], it is necessary to determine the oxygen adsorption structure on the Pt nanoparticles in order to conduct spectral analysis.

The Pt nanoparticles to be calculated are Pt nanoparticles composed of 586 atoms of the cuboctahedron type corresponding to the actual catalyst particle size range of 2.5 nm in order to study the high-coverage oxygen adsorption state where subsurface oxygen atoms also exist. The primary purpose is to obtain the adsorption structure by VASP calculation and provide the coordinates for FDMNES simulation. The unit cell has a volume of 22.13×44.26×33.19 ($Å^3$) and contains 215 Pt atoms and oxygen atoms. After optimization of this unit cell, cuboctahadral nanoparticle is obtained by symmetry operation. The structure optimization calculation was performed by allowing the relaxation of the first and second neighbors of oxygen atoms. The energy cutoff is 400 eV and the k-point mesh is 3x2x2. The representative models are shown in Fig. 1.

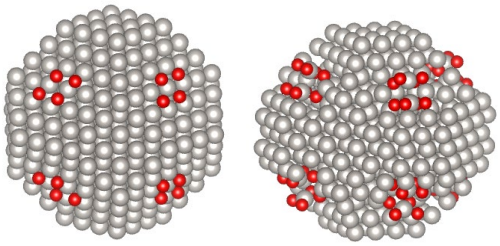

Fig. 1 Obtained models $Pt_{586}O_{32}$ and $Pt_{586}O_{64}$.

Now calculations to determine chemical potential for each species under electrochemical processes are in progress.

## References

[1] J.K. Norskov et al. , J. Phys. Chem. B **108**, 17886 (2004).

[2] R. Jinnouchi et al., Catal. Today **262**, 100 (2016).

# Modeling of the Ammonia Decomposition Reaction on Iron-based Material Surfaces

Peijie FENG, Minhyeok LEE, and Yuji SUZUKI

*Department of Mechanical Engineering, School of Engineering,*

*The University of Tokyo, 7-3-1 Hongo, Bunkyo-ku, Tokyo 113-8656*

Ammonia is expected as a next-generation green energy carrier due to its high hydrogen density and ease of liquifying for storage and transportation. However, the direct application of ammonia as a fuel suffers from its low flammability and potential NOx emission [1]. A fundamental understanding of ammonia reaction kinetics is necessary to overcome these issues. On the other hand, since ammonia-related reaction kinetics has been developed and validated mainly focusing on DeNOx applications, the kinetics model often loses its robustness in absence of oxygen, where thermal decomposition mainly occurs [2].

Therefore, we conducted density functional theory (DFT) calculations using the Vienna Ab initio Simulation Package (VASP) with the aid of the supercomputer system at ISSP to evaluate the rate-determining step of ammonia surface decomposition on iron-based materials.

It has been demonstrated that the nitrogen recombination reaction shows the largest activation energy on metal surfaces such as Fe, Co, and Ni [3], and accordingly, it can be assumed as the rate-determining step. Any surface offering a lower N-N recombination activation barrier would significantly facilitate ammonia decomposition. To estimate the reactivity of ammonia on iron nitride and compare it with that on iron, DFT calculations are performed that illustrate the activation barrier of the rate-determining step on iron and iron nitride. Firstly, the surface energy is calculated to identify the most common lattice surface where the reaction happens. Secondly, the adsorption conformation of $N_2$ and atomic N is calculated to obtain the system's total energy. Finally, the calculated conformation for the reactant and product is used to estimate the total energy of transition states. Based on a series of calculations, the activation energy can be estimated from the energy difference between the transition state and the initial reactant state.

The surface energy calculation on iron nitride (FeN) is performed on lattice surfaces 100, 110 (with Fe or N at the top layer), and 111 (with Fe or N at the top layer). The result shows the lattice surface 110 has the lowest surface energy at around $0.086 eV/Å^2$ as shown in Table 1. The lower the surface energy, the more stable the surface is and the more common it is on the catalyst surface as

experimentally prepared. On the other hand, a closed-packed surface (110) can be found on iron surfaces, which usually possess the lowest surface energy. Thus, FeN with lattice surface 110 and Fe with lattice surface 110 are used to estimate and compare the heterogeneous reaction of ammonia.

Table 1: Surface energy of iron nitride FeN.

| Lattice Surface | 110 | 100 | | 111 | |
|---|---|---|---|---|---|
| Top Element | - | Fe | N | Fe | N |
| Surface Energy [eV/Å$^2$] | **0.086** | 0.186 | 0.361 | 0.361 | 0.093 |

Since N-N recombination is the key rate-determining step of ammonia decomposition, the most stable adsorption site for N is found by placing N atoms at all possible adsorption sites (as shown in Fig. 1) on the surface both for FeN-110 and Fe-110. Among all possible adsorption sites, the Fe-top site on FeN-110 and the Hollow site on Fe-110 showed the lowest adsorption energy, indicating they are the most preferable active site to adsorb free N atoms.

By defining the product conformation for $N_2$ molecules on the surface, the climbing image

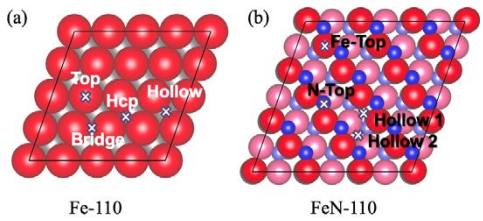


Fig. 1: Adsorption site of (a) Fe-110 and (b) FeN-110 surfaces.

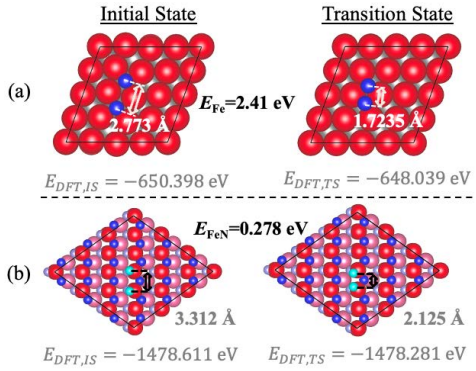


Fig. 2: Initial and transition states of N-N recombination for (a) Fe-110 and (b) FeN-110 surfaces.

nudged elastic band (CI-NEB) method [4] calculation can be performed first-principally, which yields the transition states and the total energies of the reaction between the given reactants and the products. As shown in Fig. 2, the FeN surface provides a lower activation energy (0.278 eV) than the Fe surface (2.41 eV), indicating a promising catalyst for ammonia decomposition reaction.

Further improvements in finding the reaction kinetics shall be made through the harmonic transition state method.

## References

[1] M.V. Manna, P. Sabia, R. Ragucci, and M. de Joannon, Fuel **264,** 116768 (2020).

[2] P. Glarborg, H. Hashemi, and P. Marshall, Fuel Commun. **10**, 100049 (2022).

[3] X. Duan *et al.*, J. Mol. Catal. A Chem. **357**, 81 (2012) .

[4] G. Henkelman and H. Jónsson, J. Chem. Phys. **111**, 7010 (1999).

# Study on the Catalytic Mechanism of RuTi Alloy in Catalyst-Referred Etching Method

Pho Van BUI, Daisetsu TOH, Kouji INAGAKI, Yoshitada MORIKAWA

*Grad. School of Engineering,*

*Osaka University, 2-1 Yamada-oka, Suita, Osaka 565-0871*

Polishing is an extremely important technique used in the finishing processes for optical and semiconductor surfaces and determines the performance of the final products. To produce smooth surface without introducing any crystallographically damaged surface, only pure chemical etching method is desired. Recently, catalyst-referred etching (CARE) method using Pt catalyst and water (as an etchant) has been proposed [1]. CARE can planarize SiC and various crystalline semiconductor materials to atomically smooth surfaces [2,3]. The main role of the catalyst is to dissociate water molecules and to stabilize the five-fold coordinated states. After a Si was removed from the material, silicic acid is formed and bonded to the catalyst surface.

To improve the removal rate (RR) and stability, many catalyst metals have tested their capability as a catalyst metal in CARE. Our recent studies found that Ni and Ru alloy are the best catalysts in terms of RR [4]. However, the RR is decayed in time due to poisoning by removal products. Our recent experimental results have shown that alloying Ru with Ti could effectively improve its stability for several hours of polishing compared to Ni or Ru itself [5]. The long-term stability of a catalyst could reduce the cost and increase the reliability of CARE to be a practical ultraprecision polishing method for next-generation optical devices. Therefore, purpose

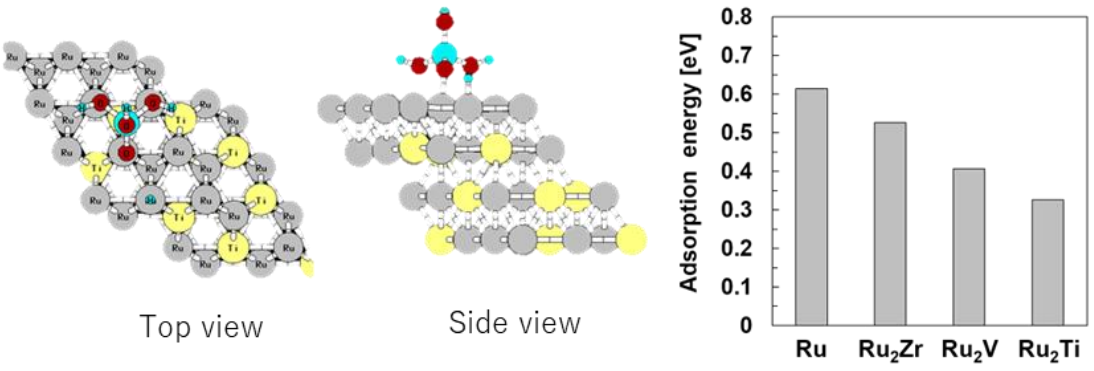


Fig. 1: Top and side views of the $Ru_2M$ slab model with silicic acid. Adsorption energy of silicic acid.

of the proposed research is to elucidate the catalytic mechanism of RuTi alloy and general understanding of the catalytic decay using first principles calculations.

The DFT calculations were performed using the Simulation Tool for Atom Technology package, which has clarified the adsorption and dissociative reaction on metal surfaces [6-8]. The electron–ion charge interactions were described by an ultra-soft pseudopotential. The wavefunction and charge density were expanded by a plane-wave basis set with 25 and 225 Ry cut-off energies, respectively. Optimization was iteratively performed until the residual forces acting on all atoms at the saddle point were reduced to below $10^{-3}$ $E_h/a_0$, where $E_h$ = 27.211 eV and $a_0$ = 0.529 Å.

In this study, we used the 3×4×4 supercell model of Ru with (0001) surface as the host metal catalyst model, as shown in Fig. 1. A few Ru atoms are substituted by a transition metal atom, such as Zr, V, and Ti, creating a Ru-based alloy catalyst model. The adsorption energy, $E_{adsorb}$, of silicic acid on Ru, Ru-V, Ru-Ti, and Ru-Zr alloy catalyst surfaces was calculated by,

$$E_{adsorb} = |E_{Ru+silicic\ acid} - (E_{Ru} + E_{silicic\ acid})|,$$

where $E_{Ru+silicic}$ acid, $E_{Ru}$, and $E_{sicilic\ acid}$ are the total energies of the Ru-based catalyst with adsorbed silicic acid, the Ru-based catalyst, and silicic acid, respectively.

The adsorption energies of silicic acid on the Ru catalyst and Ru-based alloy catalyst are shown in Fig. 1. The adsorption energy of silicic acid on RuTi alloy is the lowest among the investigated catalysts. DFT calculations showed that Ti doping to Ru reduces the adsorption energy of silicic acid on the Ru site from 0.61 to 0.32 eV and efficiently restores the active Ru sites.

## References

[1] H. Hara, Y. Sano, H. Mimura, K. Arima, K. Kubota, K. Yagi, J. Murata, and K. Yamauchi, J. Electron Mater. **35**, L11 (2006).

[2] D. Toh, P.V. Bui, N. Kidani, S. Matsuyama, Y. Sano, Y. Morikawa, and K. Yamauchi, K. Rev. Sci. Instrum. **90**, 045115 (2019).

[3] A. Isohashi, P.V. Bui, D. Toh, S. Matsuyama, Y. Sano, K. Inagaki, Y. Morikawa, and K. Yamauchi, Appl. Phys. Lett. **110**, 201601 (2017).

[4] D. Toh, P.V. Bui, A. Isohashi, S. Matsuyama, K. Yamauchi, and Y. Sano, Rev. Sci. Instrum. **91**, 045108 (2020).

[5] D. Toh, K. Kayao, P.V. Bui, K. Inagaki, Y. Morikawa, K. Yamauchi, and Y. Sano, Pre. Eng. submitted.

[6] T. Hayashi, Y. Morikawa, and H. Nozoya, J. Chem. Phys. **114**, 7615 (2001).

[7] Y. Hamamoto, I. Hamada, K. Inagaki, and Y. Morikawa, Phys. Rev. B **93**, 245440 (2016).

[8] J. Quan, F. Muttaqien, T. Kondo, T. Kozaeashi, T. Mogi, T. Imabayashi, Y. Hamamoto, K. Inagaki, I. Hamada, Y. Morikawa, and J. Nakamura, Nature Chem. **11**, 722 (2019).

# Proton Storage in Ruddlesden–Popper-type $Sr_3Fe_2O_7$

Kosuke Kawai, Masashi Okubo

*Department of Electrical Engineering and Bioscience, School of Advanced Science and Engineering, Waseda University, 3-4-1 Okubo, Shinjuku-ku, Tokyo 169-8555*

We investigated proton storage properties of Ruddlesden–Popper-type $Sr_3Fe_2O_7$ using density functional theory (DFT) calculations. This year, we focused on thermodynamically stable sites of proton in the lattice of $Sr_3Fe_2O_7$.

DFT calculations were performed with the Vienna ab initio simulation package (VASP). The projected augmented wave method and a plane basis set implemented in the VASP code were utilized with a cutoff energy of 520 eV and *k*-point sampling on a 6×6×2 grid.[1] The generalized gradient approximation of the Perdew–Burke–Ernzerhof exchange-correlation functional was used with Hubbard U = 4.0 eV for Fe to correct the self-interaction error of correlated d electrons.[2,3] An initial structure model of $Sr_3Fe_2O_7$ was obtained from the Materials Project (ID: mp-18820), and expanded to a superstructure of 2×2×1 ($Sr_{24}Fe_{16}O_{56}$, **Fig.1a**). Structure optimization was performed with a convergence condition of $\Delta F$ < 0.01 eV/Å. A H atom was located manually near an O atom with a H–O distance of < 1 Å, and then structure optimization was performed in the same way. Graphics of crystal structures were drawn by VESTA software.[4]

Three thermodynamically stable $H^+$ sites were identified around interlayer space after structure optimization. Site A is bridged to the nearest O atom in the same $FeO_6$ octahedron, and the most thermodynamically stable. Site B in the interlayer space is directed to an O atom in neighboring $Fe_2O_7$ layer. Site C is also in the interlayer space but directed to a Sr atom, resulting in high electrostatic energy.

## References

[1] G. Kresse and J. Furthmüller, *Phys. Rev. B* **54**, 11169−11186 (1996).

[2] J. P. Perdew, et al., *Phys. Rev. Lett.* **77**, 3865−3868 (1996).

[3] F. Zhou, et al., P*hys. Rev. B - Condens. Matter Mater. Phys.* **70**, 1–8 (2004).

[4] K. Momma and F. Izumi, *J. Appl. Crystallogr.* **41**, 653−658 (2008).

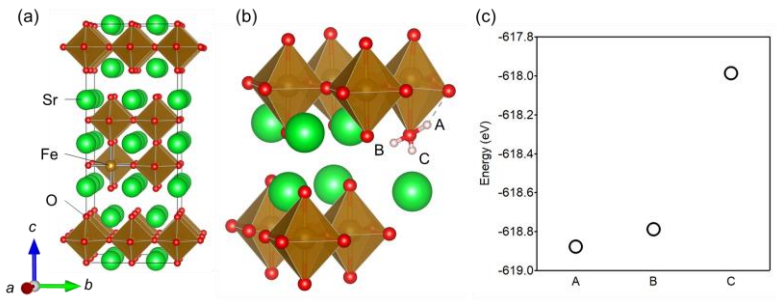


**Fig.1** (a) Crystal structure of Ruddlesden–Popper-type $Sr_3Fe_2O_7$, (b) typical $H^+$ sites, and (c) total energies of $HSr_{24}Fe_{16}O_{56}$.

# Ultrafast adsorption states of two-dimensional metal-organic-frameworks and semiconductors

Kenichi SHUDO

*Fac. of Eng/Sci, Yokohama Nat'l Univ.*

*The University of Tokyo, Kashiwa-no-ha, Kashiwa, Chiba 277-8581*

We performed calculation for elucidation of a nonlinear optical effect of a typical transition metal dichalcogenides, $MoSe_2$, using Vienna *ab initio* Simulation Package (VASP). Molecular dynamics produces well the atomic trajectories from an initial kick due to potential deformation caused by photo-transition. Hyperlinear components gives a sum frequency and harmonics of fundamental oscillation (Fig.1). These Fourier components are contrary to the linear normal modes reachable either *via* experimental cw-Raman spectroscopy and theoretical diagonalization of atomic potential along with the displacement of each atom. The nonlinear optical effect derived by atomic motion was thus clarified.

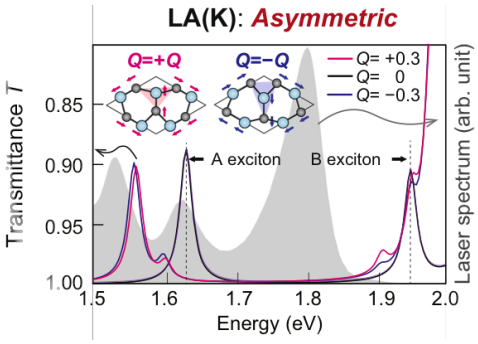


Fig. 1: Example of nonlinear vibronic modes of $MoSe_2$ simulated by means of molecular dynamics at femtosecond scale. See Ref [1] for detail.

Metastable-atom electron spectroscopy (MAES) reveals electric states of a surface, exclusively giving information of the electron cloud protrude into the vacuum. We measured the spectra of such electrons of a typical topological insulator, $Bi_2Se_3$. Our preliminary calculation of one to a few layers of this crystal, using VASP. The obtained results are analyzed based on the local density of state dependent on the distance from the top-most surface atoms. The spectral features of the MAES applied to the crystal are concluded to be originated from concurrent processes of resonance ionization and Auger neutralization.

Similar local electron distribution curves are obtained also for layler-by-layer structures of metal-organic framework (MOF) of 5,10,15,20-Tetrakis(4-carboxyphenyl)-porphyrin.

## References

[1] S. Bae, K. Matsumoto, H. Raebiger, K. Shudo, Y.-H. Kim, Ø.S. Handegård, T. Nagao, M. Kitajima, Y. Sakai, X. Zhang, R. Vajtai, P. Ajayan, J. Kono, J. Takeda, I. Katayama: Nature Communications 13, 4279 (2022)

# Analyzing Reaction Mechanism of Charge Transfer in Catalysis by Electronic Structure Calculations

Tatsuya JOUTSUKA

*Institute of Quantum Beam Science, Graduate School of Science and Engineering, Ibaraki University, Hitachi, 316-8511 Ibaraki, Japan.*

*Frontier Research Center for Applied Atomic Sciences, Ibaraki University, 162-1 Shirakata, Tokai, Ibaraki 319-1106, Japan.*

*Carbon Recycle Energy Research Center, Ibaraki University, Hitachi, 316-8511 Ibaraki, Japan.*

Focusing on the selectivity of zirconia-catalyzed methanol synthesis, we calculated adsorption and reaction energies to clarify the reaction mechanism. [1-2] In addition, polaron transfer rate constants in bulk titanium dioxide ($TiO_2$) and $SrTiO_3$ were calculated by the constrained density functional theory (CDFT) method. Then, the electronic structure calculation was used to elucidate the photocatalytic reaction mechanism and crystal plane selectivity in photocatalysts.

A zirconia-based solid solution catalyst $ZnZrO_x$ was prepared by substituting Zn with Zr, which has high catalytic activity. The correlation between the binding strength of the substituted elements and adsorbates (reactants, products, and intermediates) and methanol synthesis capacity was clarified. The DFT calculations using cp2k program package showed that the Zn species in the clusters are more likely to be exposed on the surface. This result is consistent with experimental results, suggesting that Zn species are unevenly distributed on the surface and deposited near the surface; by adding excess Zn to $ZrO_2$, both Zn-containing clusters and ZnO nanoparticles were formed. We also analyzed the dynamics in adsorption and chemical reactions by molecular dynamics simulation and develop a method to analyze charge transfer. In addition, we elucidated the mechanism of Cu nanoparticle formation with a size <10 nm using DFT calculations.[3] Furthermore, we analyzed theoretical methods for proton transfer in liquid water,[4] cross-coupling of arylboronic acid and imidazole on *t*-$ZrO_2$,[5] and Cu deposition by chemical vapor deposition using a CuI precursor[6] using VASP and cp2k program packages.

In addition, the polaron transfer rate constants in bulk $TiO_2$ and $SrTiO_3$ (Fig. 1) was calculated by the CDFT method along the several directions (such as [101] direction in $TiO_2$) using cp2k program package. We found

that the CDFT method can evaluate the potential energy profile more accurately than linear interpolation of structures that has been frequently employed for bulk $TiO_2$. We next moved on to the $SrTiO_3$ (001) and (110) surfaces to understand the porlaron transfer at the surface. We are now studying the relation with the oxygen vacancy and electron polaron to discuss the photocatalytic mechanism further using cp2k program package.

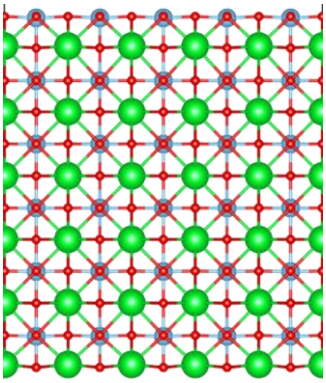

Fig. 1: Bulk $SrTiO_3$.

## References

[1] Shohei Tada, Nagomu Ochiai, Hiroka Kinoshita, Mitsuhiro Yoshida, Natsumi Shimada, Tatsuya Joutsuka, Masahiko Nishijima, Tetsuo Honma, Noriko Yamauchi, Yoshio Kobayashi, and Kenta Iyoki, ACS Catal., **12**, 7748–7759 (2022).

[2] Tatsuya Joutsuka and Shohei Tada,* J. Phys. Chem. C, **127**, 6998–7008 (2023)

[3] Tatsuya Joutsuka, Ryu Hamamura, Kakeru Fujiwara, Tetsuo Honma, Masahiko Nishijima, and Shohei Tada, Int. J. Hydrog. Energy, **47**, 21369–21374 (2022).

[4] Tatsuya Joutsuka, J. Phys. Chem. B, **126**, 24, 4565–4571 (2022).

[5] Masaru Kondo, Tatsuya Joutsuka, Kakeru Fujiwara, Tetsuo Honma, and Shohei Tada, Catal. Sci. Technol., **13**, 2247-2254 (2023).

[6] Gento Toyoda, Hikari Kikuchi, Satoshi Yamauchi, Tatsuya Joutsuka, Takashi Fuse, and Yusuke Kubota, Jpn. J. Appl. Phys., **62**, SH1002 (2023).

# First-principles calculation of oxygen defects on the surface of titanium dioxide $TiO_2$

Shoya Kawano

*Department of Electrical and Electronic Engineering, Kyushu Institute of Technology, Kitakyushu, Fukuoka, 804-8550*

We have studied stability of oxygen defects on $TiO_2$ surface by density functional calculations in this project. Oxygen defects in $TiO_2$ significantly changes its catalytic performance, carrier transport, hydrophilicity, and other functions. Therefore, if we can successfully control these oxygen defects, it will be possible to design the function of $TiO_2$. For this purpose, we have studied the configuration of oxygen defects on $TiO_2$ surface using scanning probe microscopy (SPM) image with template matching method. This SPM image analysis indicated typical configuration of oxygen defects. Therefore, we investigated stability of configuration of oxygen defects on $TiO_2$ surface by density functional calculations.

We performed density functional calculations for slab models of rutile $TiO_2$ (110) by using Quantum ESPRESSO code [1,2]. The slab models have two oxygen defects on surface and 1 nm vacuum gaps. The unit cell included 144, 240, 300 and 450 atoms are considered for slab models without defects. In Quantum ESPRESSO, we use the norm-conserving pseudo potentials generated by the code ONCVPSP (Optimized Norm Conserving Vanderbilt PSeudopotential), and are obtained them from the PseudoDojo [3]. The exchange-correlation function is used Perdew-Burke-Ernzerhof type. For example, Γ-point-centered 2×2×1 k-points sampling were used for 2×2×4 surface unit cell of $TiO_2$ (110) included 238 atoms. We use the energy cutoff of 96 Ry for the wave function, a convergence criterion for the electronic self-consistency loop of $10^{-10}$ Ry, and the Gaussian smearing method with a smearing width of 0.002 Ry. Lattice parameters of $TiO_2$ is referred to previous report [4].

Figure 1 shows calculated structure of $TiO_2$ surface model of 2×2×4 surface unit cell with two defects (238 atoms) and their defect energy $E_{\mathrm{vac}}$. $E_{\mathrm{vac}}$ is defined as follows

$$E_{vac} = E_{Ti_nO_{2n-1}} + E_{O_2} - E_{Ti_nO_{2n}} ,$$

where $E_{Ti_nO_{2n-1}}$, $E_{O_2}$ and $E_{Ti_nO_{2n}}$ are total energy of slab with defects, total energy of oxygen molecule and total energy of slab without defects. We considered five configurations for two defects introduced at bridge oxygen on the surface. The bridge oxygen is bonded with titanium along the parallel axis in Fig. 1. Configurations of defects like Fig. 1 (a)-(c) are more stable than defects along parallel axis in Fig.1 (d) and (e). This

trend of results is consistent with our STM image analysis.

We have used the L4cpu of system B with 512 parallel computing for 144 and 240 atoms unit cell, the L16cpu of system B with 2048 parallel computing for 300 and 450 atoms unit cell.

## References

[1] P. Giannozzi *et. al*. J. Phys. Condens. Matter. **21**, 395502 (2009).

[2] P. Giannozzi *et. al*. J. Phys. Condens. Matter. **29**, 465901 (2017)

[3] M. J. van Setten, M. Giantomassi, E. Bousquet, M. J. Verstraete, D. R. Hamann, X. Gonze, G.-M. Rignanese, Computer Physics Communications **226**, 39-54 (2018)

[4] X. W. Wang, B. H. Zhang, L. Y. Sun, W. N. Qiao, Y. D. Hao, Y. C. Hu, and X. E. Wang, Journal of Alloys and Compounds **745**, 856 (2018).

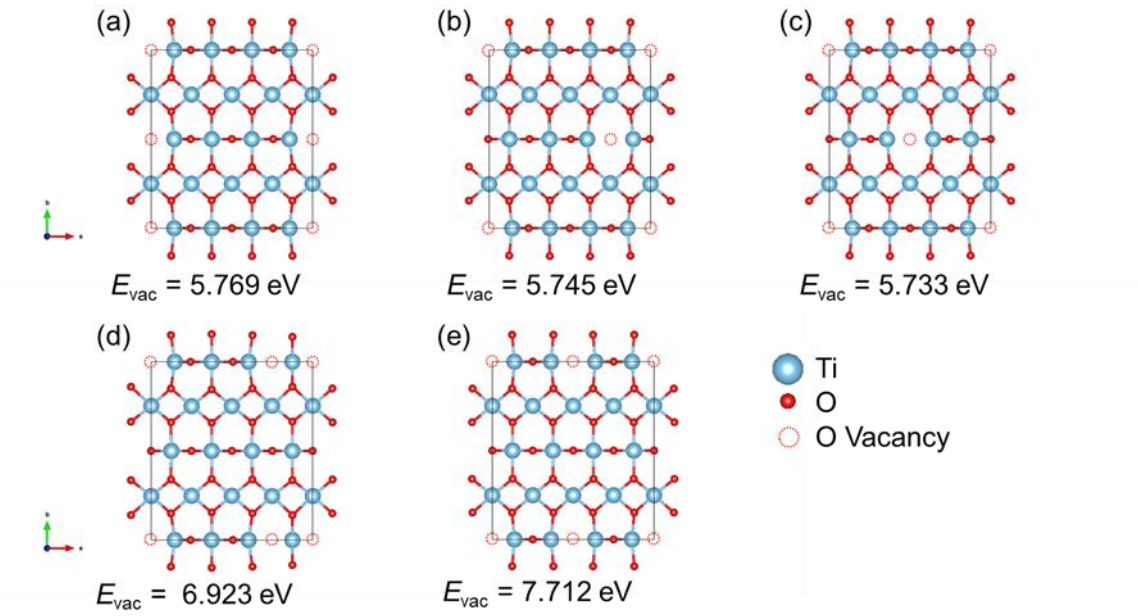


Fig. 1 Calculated structure of $TiO_2$ surface model and their defect energy.

# Thermal conductivity calculation for high thermal conductive insulator

Shoya Kawano

*Department of Electrical and Electronic Engineering, Kyushu Institute of Technology, Kitakyushu, Fukuoka, 804-8550*

We have computed the lattice thermal conductivity of several materials to create a database for the design of high thermal conductive insulators. High thermal conductivity insulators are essential for the substrate of power devices. To develop high-performance power devices, it is necessary to discover new substrate materials with high thermal conductivity insulators. In this project, we created a database of lattice thermal conductivity for materials informatics.

We performed density functional phonon calculations using the ALAMODE code [1] with the Quantum ESPRESSO code [2,3] to compute the lattice thermal conductivity. We calculated the second- and third-order force constants from density functional theory. The second-order force constants were calculated using the finite displacement method, while the third-order force constants were calculated using the random displacement method implemented in ALAMODE. In the density functional calculations, we used norm-conserving pseudo-potentials generated by the Optimized Norm Conserving Vanderbilt Pseudopotential code, obtained from PseudoDojo [4]. We used the Perdew-Burke-Ernzerhof type exchange-correlation function. For finite displacement and random displacement approaches, we used displacement distances of 0.02 and 0.04 Å, respectively.

We calculated the lattice thermal conductivity of AlAs, CaO, SrO, YN, $CeO_2$, AlN, $CaF_2$, $MgBe_2N_2$, $TaGaFe_2$, and BN. These structures were collected from the Materials Project [5]. For the random displacement approach, we used 20-500 structures and compared their thermal conductivity accuracy. We found that a set of 20 structures satisfied the accuracy for the lattice thermal conductivity database. We continue to calculate the lattice thermal conductivity with the obtained parameters in this project to create a database.

We used the F16CPU of system B with 2048 parallel computing by MPI for the density functional calculations for each displacement. For thermal conductivity calculation, MPI/OpenMP hybrid parallelization was used with the F16CPU of system B.

## References

[1] T. Tadano, Y. Gohda, and S. Tsuneyuki, J. Phys.: Condens. Matter **26**, 225402 (2014)

[2] P. Giannozzi *et*. *al*. J. Phys. Condens. Matter. **21**, 395502 (2009).

[3] P. Giannozzi *et*. *al*. J. Phys. Condens. Matter. **29**, 465901 (2017)

[4] M. J. van Setten, M. Giantomassi, E. Bousquet, M. J. Verstraete, D. R. Hamann, X. Gonze, G.-M. Rignanese, Computer Physics Communications **226**, 39-54 (2018)

[5] https://materialsproject.org/

# Stable structures of low-dimensional systems from first-principles

Shota ONO
*Department of Electrical, Electronic and Computer Engineering, Gifu University*
*Gifu 501-1193*

In this project, we have studied (i) stable structures of two-dimensional (2D) hexagonal materials [1], (ii) structural and electronic properties of 2D ionic crystals [2], and (iii) surface rippling on non-close-packed metal surfaces [3] using density functional theory (DFT) and machine-learning approaches.

For the case (i), we have explored the stable configurations of atomic species on a hexagonal plane in 2D binary systems. The configuration search was accelerated by using the Bayesian optimization (BO) approach. For the 2D copper-based systems of Cu-$X$, we have shown that the structures having a hexagonal or elongated ring of Cu (or $X$) atoms containing a $X$ (or Cu) cluster in the unit cell are relatively stable, in particular, for $X$ = Be, Pd, and Au (see Fig. 1(a)). The binary Lennard-Jones model was used to interpret the optimized structures predicted by DFT calculations.

For the case (ii), we have shown that 4 and 12 IA-VII alkali halides in the 2D hexagonal and tetragonal structures (see Fig. 1(b)) are dynamically stable, respectively. The electronic band gaps range from 6.8 eV for LiF to 3.9 eV for RbI and CsI in the tetragonal structure within the generalized gradient approximation. A hard sphere model that considers the Madelung energy and the core-core repulsion explains the nearest-neighbor bond length and the cohesive energy of 2D alkali halides.

For the case (iii), we have studied surface rippling of $X/A(100)$ (see Fig. 1(c)), assuming $X$ = H to Bi except for noble gases and $A$ = Cu, Ag, and Au. We have shown that small atoms (such as H, C, N, O and F) attract electrons from the substrate due to the large electronegativity, which prevent them from passing through voids in the (100) surface. We have also discussed a breakdown of the hard sphere model for predicting the surface rippling amplitude.

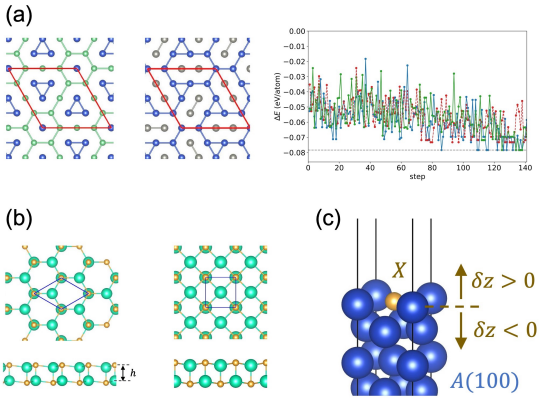


Figure 1: Stable structures (a), (b), and (c) studied in Refs [1], [2], and [3], respectively. The structures in (a) were found by using BO.

## References

[1] S. Ono: AIP Advances **12**, 085313 (2022).

[2] S. Ono: J. Phys. Soc. Jpn. **91**, 094606 (2022).

[3] S. Ono, H. Satomi, and J. Yuhara: Comp. Mater. Sci. **218**, 111959 (2023).

# Stable structure of vacancy cluster in tungsten and iron trapping multiple hydrogen atoms

Kazuhito Ohsawa

*Institute for Applied Mechanics, Kyushu University,*

*Kasuga-koen, Kasuga, Fukuoka 816-8580*

## Introduction

Tungsten (W) and Iron (Fe) are important materials for plasma facing materials (PFMs) used in fusion reactors. In particular, W shows promise as divertor armor tiles exposed to the most intense plasma particle irradiation. Vacancy (V) and vacancy clusters nucleated in the metals under the irradiation circumstance are considered to be a large amount of hydrogen (H) and hydrogen isotope trap sites. In particular, tritium (T) retention in the PFMs is a serious problem for safety operation of fusion reactor because T is radio isotope whose half-life is about 12 years. So, the investigation of the vacancy clusters in the metals and H trapping are important subjects in the field of PFMs. In the present work, stable structures of vacancy clusters and their interaction with multiple H atoms in W and Fe lattice are investigated by computational methods. A difference of vacancy clusters in W and Fe was clarified. Besides, positions of multiple H atoms trapped in the vacancy type lattice defects are examined. The effects of H were investigated on the stable structures of the vacancy clusters.

## Simulation method

Stable vacancy cluster structures and positions of multiple H atoms trapped in the vacancy clusters in W and Fe specimen were calculated in terms of first-principle calculations based on density functional theory (DFT). We used the Vienna ab-initio simulation package (VASP) for the DFT simulations. A large simulation cell, composed of 5x5x5 bcc lattice (250 atoms), were used in order to reduce the effects of periodic boundary condition imposed on the simulation cell. The cut-off energy of plane wave was 350eV.

The binding energy $E_b$ of di-vacancy $V_2$ was defined as

$$E_b(V_2) = 2E[V]-E[V_2]-E_{ref}, \qquad (1)$$

where $E$ is cohesive energy of the supercell and $E_{ref}$ indicates energy of perfect crystal. For example, $E[V]$ and $E[V_2]$ mean cohesive energies of supercells containing mono- and di-vacancy, respectively. Positive binding energy $E_b$ corresponds to attractive interaction of the two vacancies. Similarly, the binding energy of V-H complex $V_2H_2$ i.e., di-vacancy trapping two H atoms, is defined as

$$E_b(V_2H_2) = 2E[VH]-E[V_2H_2]-E_{ref},. \qquad (2)$$

## Results and discussion

Stable structures of di-vacancy in W and Fe are different, as shown in Fig.1. The most stable arrangements of two vacancies are <111> in W and <100> in Fe, respectively. Actually, binding energy between two vacancies arranged in <100> direction is larger than that of <111> in Fe estimated in Eq. (1), according to Fig. 2. However, <111> arrangement of di-vacancy trapping two H are more stable than <100> one estimated in Eq. (2). Therefore, stable structure of di-vacancy in Fe is changed from <100> to <111> arrangement by the H trapping. By the way, the most stable structure of di-vacancy in W is <111> arrangement in both cases. Figure 3 shows two H atoms trapped in di-vacancy in W and Fe. H atoms trapped in the vacancy type lattice defects are allocated in the vicinity of octahedral interstitial (O-site). In addition to it, H atoms preferentially occupy O-sites located in the center of the di-vacancy where two vacancies are in contact with each other.

In the present work, H trapping are supposed to play important roles for stabilization of vacancy clusters. The binding energy of vacancy clusters increase and structure of di-vacancy are changed by the H trapping in Fe.

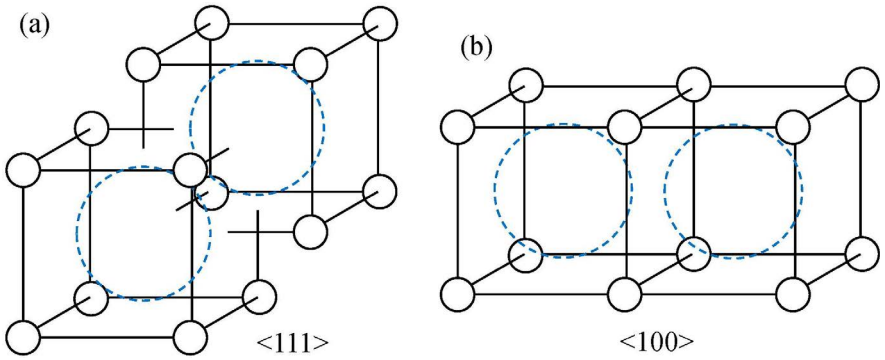


Fig. 1: Most stable structure of di-vacancy in bcc lattice. Arrangements of two vacancies are (a) <111> in W and (b) <100> in Fe, respectively.

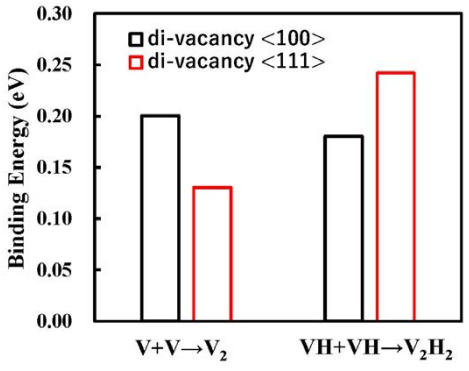


Fig. 2: Binding energy of di-vacancy and di-vacancy trapping two H atoms in Fe.

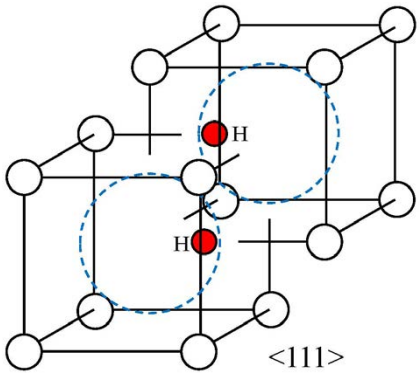


Fig. 3: Positions of two H atoms trapped in di-vacancy in W and Fe.

# Ab initio molecular-dynamics study of structural and transport properties of liquid mixtures containing hydrocarbon under ultra-high pressure

Satoshi OHMURA

*Department of Civil and Environmental Engineering,*

*Hiroshima Institute of Technology, Saeki-ku, Hiroshima 731-5193*

Understanding the structures and physical properties of the C-H system at higher pressures is essential to constrain the interiors of the ice giant planets (extrasolar planet). Therefore, it is important for planetary science to understand the behavior of this important material in extreme conditions. For this reason, we have performed ab initio molecular-dynamics (MD) simulations for liquid Methane ($CH_4$) under high pressures. We used a 500-atom system consisting of 400 hydrogen and 100 carbon atoms in a cubic supercell with periodic boundary conditions.

Figure 1 shows the pressure dependence of the pair distribution functions $g_{\alpha\beta}(r)$ of liquid $CH_4$ obtained from the MD simulation. Since methane molecules remain intact up to 100 GPa, the shape of $g_{CC}(r)$, $g_{CH}(r)$ and, $g_{HH}(r)$ at 55 and 100 GPa are almost the same. Above 150 GPa, in $g_{CC}(r)$, a new peak appears at approximately 1.4 Å and its position gradually shifts to a smaller $r$ with increasing pressure. Moreover, the first peak of $g_{CC}(r)$ is clearly separated from a second peak at pressures of 150 GPa, suggesting that the C-C bonds contributing to the first peak are highly stable and strong. The simulation found that the interaction remains even under ultrahigh pressure conditions of 1300 GPa. For hydrogen, molecular hydrogen is observed after methane dissociation (at 150 GPa). When the pressure becomes higher, hydrogen molecule becomes unstable.

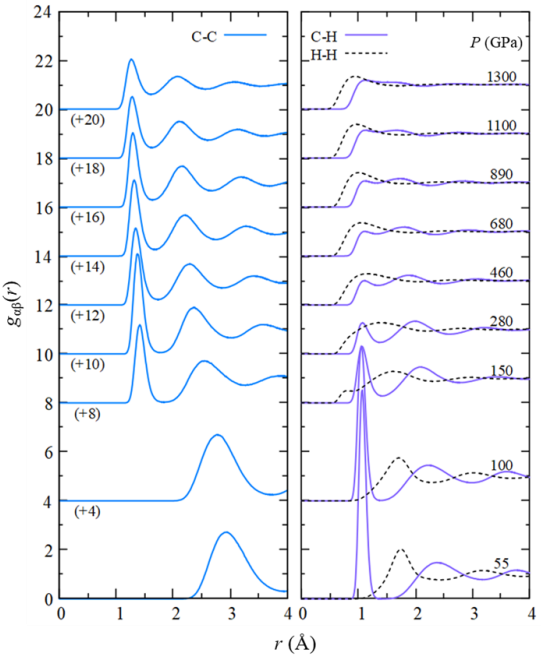


Fig. 1: Pressure dependence of the pair distribution functions $g_{\alpha\beta}(r)$ of liquid $CH_4$.

# Temperature dependence of structural and electronic properties of organic molecular thin film surfaces

**Kaori Niki**

*Graduate school of science*

*Chiba University, Yayoi-cho, Inage-ku, Chiba 263-8522*

In recent years, it has been reported that organic molecules' electronic and physical properties interact with the surface using Wave number space-resolved Photoelectron Spectroscopy. We have investigated the copper (Ⅱ) phthalocyanine (CuPc) - monolayer substrate system. This year, we investigated molecular motion depending on the terminal. Monolayer $TiSe_2$ has two typical phases depending on the temperature. A (1 × 1) structure (normal phase) is shown at room temperature, and a (2 × 2) superstructure (CDW phase) is realized under the 200 K. Each phase has a band gap of 83 meV and 153 meV, respectively [1, 2]. We have adopted this interesting thin film as the substrate and reported the structural changes depending on the temperature in the previous year and structure optimization, resulting in an adsorption distance of 3.16 Å.

This time, we performed Molecular dynamics (MD) simulation using these structures as the ground state, and clarified the structures after temperature change.

**MD calcuration of CuPc on $TiSe_2$**

We performed density functional theory (DFT) calculations using the Vienna Ab Initio Software Package (VASP) version 5.4.4 [3,4]. The Generalized Gradient Approximation (GGA) within the Perdew-Burke-Ernzerhof (PBE) formalism described the exchange-correlation effects. We used a unit cell with lattice constants a = b = 3.53 Å, c = 20.0 Å, α = β = 90° and γ = 120°, and plane-wave basis set with the projector augmented wave (PAW) approach with an energy cutoff of 380 eV. The Brillouin zone integration was performed on a Monkhorst-Pack of 18×18×1 grid of k-points. The energy convergence criterion chosen for the self-consistency cycle was $1\times10^{-7}$ eV. To account for Fermi surface broadening, temperature parameter σ for Methfessel-Paxton smearing was applied [5]. So far, we have found the parameter set (U = 3.9 eV and σ = 0.01 eV), which reproduces the experimental result [6]. We used these parameters for the MD simulation of the CuPc / $TiSe_2$ structure. After relaxing the geometries at 0 K, the systems were brought up to 654 K by repeated velocity rescaling using the spin-polarized PBE+U DFT-D3 functional at the Γ-point. Then 5 ps microcanonical MD trajectories were generated with a 1 fs time step.

**Molecural rotation of CuPc/$TiSe_2$**

Figure 1 shows the geometry of CuPc on

TiSe2 at 0 K. S1 and S2 indicate the axis of the surface. “Center, " one of the molecular axes, is tilted 30 degrees from the axis s2.

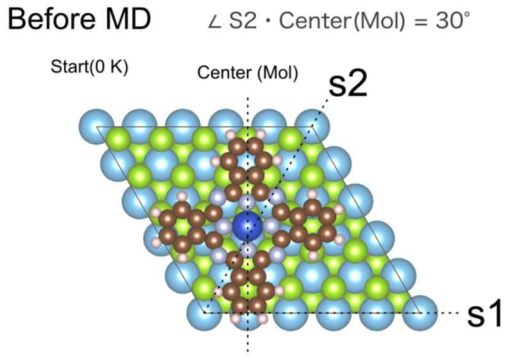


Figure 1. Geometry of CuPc/TiSe2

Figure 2 shows the geometry of CuPc/TiSe2 after MD. A temperature of 654 K is assumed. We can see the motion of the molecule to the lower left. The angle between the central and s2 is magnified to 60 degrees.

**After MD**

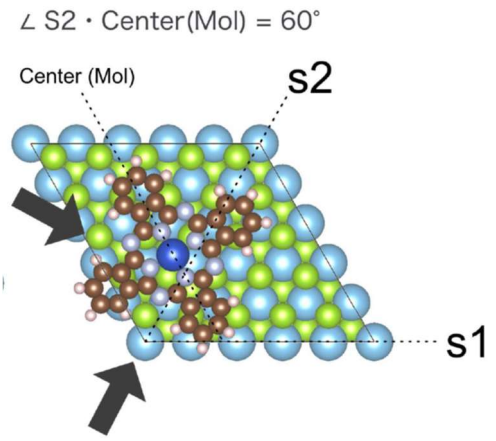


Figure 2. Geometry of CuPc/TiSe2

Cu is adsorbed between Ti and Se atoms before MD simulation. At this time, charge repulsion occurs between Cu and surrounding Se, and between carbon and Se near the center at lower temperatures.

On the other hand, after MD calculation, the number of Se electrons in TiSe2 is slightly larger than before calculation. On the other hand, the number of electrons in Cu atom decreases. A stable structure is due to the close distance between Cu and Ti creates. Nitrogen closer to the center has additional electrons and approaches Ti atoms. This also creates a stable structure.

## Conclusion

By performing MD calculations using VASP, we clarified changes in the charge distribution of molecules and substrates and molecular motions with increasing temperature.

## References

[1] J.-P. Peng *et. al.*, Phys. Rev. B **91**, 121113 (2015).

[2] P. Chen *et. al.*, Nat. Commun **6**, 8943 (2015).

[3] G. Kresse and J. Furthmuller, Phys. Rev. B, **54**, 11169 (1996).

[4] G. Kresse and J. Hafner, Phys. Rev. B, 49 14251 (1994).

[5] M. Methfessel and A. T. Paxton, Phys. Rev. B **40**, 3616 (1989).

[6] R. Bianco *et.al.*, Phys. Rev. B **92**, 094107 (2015).

# Development of First Principles methods for Light-Matter Interaction

Hiroki KATOW

*Photon Science Center, Graduate School of Engineering,*

*The University of Tokyo, Bunkyo-ku, Tokyo 113-8656, Japan*

The electronic dipole moment calculation is a fundamental of the light-matter interaction. In isolated systems, the dipole moment is defined by an expectation value of dipole operator and no ambiguities in its definition. Contrarily in periodic systems, ambiguity of the choice of cell boundary leads to the indefiniteness of its definition. Modern understanding of this issue is that the ambiguity is rooted in the indefinite complex phase factor of one-particle orbitals, which is called gauge degrees of freedom. A solution is proposed for ground states by King-Smith and Vanderbilt where the dipole moment is reformulated to exclude explicit dependency on the gauge [1].

A same obstacle is present in excitonic systems. The author of this report and colleagues have developed a gauge-free method for excitonic systems [2] as an extension of King-Smith and Vanderbilt's formula. We demonstrated the validity of our gauge-free dipole calculation of Graphane exciton by using System B. We employed Quantum ESPRESSO [3] and BerkeleyGW [4] package to compute excitonic wave functions based on GW+BSE method. In this project we calculated excitonic states of monolayer (ML) and bulk hexagonal boron nitride (hBN) for further systematic study. Massively parallelized calculations using 2048 cpu in F16cpu class were conducted. We show the exciton energy spectrum of ML- and bulk-hBN in Figure 1. Due to the weak screening of two-dimensional system ML-hBN possesses larger GW gap (8.12 eV) than bulk-hBN (5.54 eV). We also confirmed huge exciton binding energy of ML-hBN. As a future prospect, we apply our gauge-free method to ML- and bulk-hBN by utilizing the excitonic wave functions computed in this project.

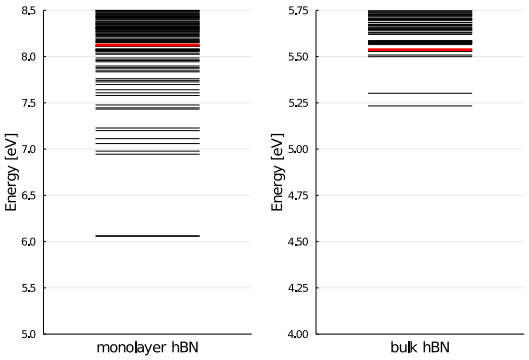


Fig. 1 Exciton energy spectrum of the monolayer hBN (left) and bulk hBN (right) calculated by using BerkeleyGW package [4] which is based on GW+BSE method. Red lines indicate GW gap.

## References

[1] R.D. King-Smith et al., Phys. Rev. B 47, 1651(R) (1993).

[2] H. Katow et al., Phys. Rev. Lett. **129**, 047401 (2022).

[3] P. Giannozzi et al., J. Phys. Condens. Matter 21, 395502 (2009).

[4] J. Deslippe et al., Comput. Phys. Commun. 183, 1269 (2012).

Fig. 1: Supercomputer System B at SCC-ISSP.

# Study on structural elementary excitations at semiconductor surfaces and interfaces

Hiroyuki KAGESHIMA
*Graduate School of Natural Science and Technology, Shimane University*
*1060 Nishi-Kawatsucho, Matsue, Shimane 690-8504*

In this project, we have been focused on physical properties of structural elementary excitations of semiconductor surfaces and interfaces. In this year, we have focused on the physical properties of SiO self-interstitial in $SiO_2$. [1] The calculations were performed based on the first-principles calculation. Program package PHASE/0 was employed. [2]

When Si is oxidized, a large volume expansion occurs at the interface, so Si is released into the oxide film in order to relax the generated strain. This is because a slightly denser and Si-rich region is formed near the interface, and a concentration gradient of excess Si is generated, which tends to promote the migration and diffusion of excess Si toward the oxide film side. Moreover, the presence of excess Si is thought to induce and to enhance structural deformation of the oxide film. Therefore, the behavior of excess Si in the near-interface oxide film governs strain relaxation in two ways. In this study, we traced the path of the migration and diffusion of excess Si at the atomic level, and investigated the energy profile by the first-principles calculations.

A quartz/Si(100) interface model with four Si layers and four $SiO_2$ layers was used for the calculation. The front and back surfaces are terminated by H, and superslab geometry with a sufficient vacuum layer is prepared. The in-plane periodicity is $2\sqrt{2} \times 2\sqrt{2}$, which is sufficiently large. The unit cell contains 142 atoms. We used plane wave bases with the cutoff of 30 Ry, and norm-conserving pseudopotentials for Si and H as well as an ultrasoft pseudopotential for O. We also used the exchange-correlation density functional of generalized gradient approximation (GGAPBE). We employed the Monkhorst-Pack k-point sampling of $4\times4\times1$. Using the structure with interstitial SiO placed at the interface as the initial structure (Fig. 1), we searched for migration diffusion paths. In the route search, the structure optimization calculation was performed by fixing one Si layer and H on the back surface. For comparison, a $SiO_2$ crystal model equivalent to one in which only the oxide film was taken out and arranged periodically was also used to investigate the characteristics of the interface.

We assumed that the excess Si is interstitial SiO in the oxide film, and that migration diffusion consists of three elementary processes. These are O vacancy transfer, Si coordination number conversion, and Si bond order conversion. All of these elementary processes are effective only for migration diffusion of interstitial SiO, and are not considered for other forms of excess Si. In particular, O vacancy transfer and Si coordination number conversion are essential. In order for Si coordination number conversion to occur, O vacancy transfer must be repeated to move O vacancies to appropriate positions. Si bond order conversion can be substituted by these two, but it has the effect of shortening several steps at once.

Based on these assumptions, we succeeded in constructing a transport diffusion path of the excess Si from the interface to the oxide film

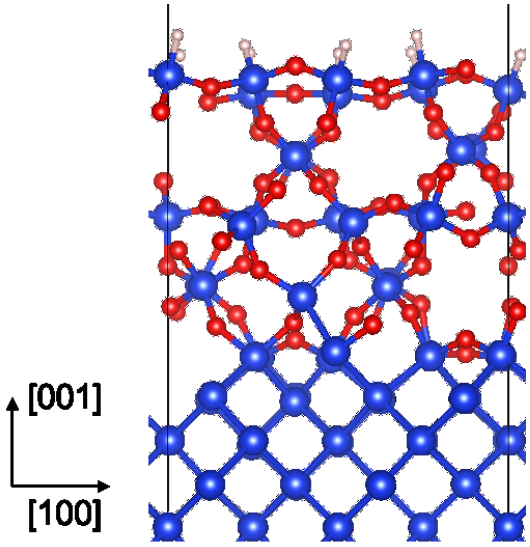


Figure 1: Starting atomic structure for the migration diffusion path of the SiO interstitial. Large, middle, and small spheres indicate Si, O, and H atoms, respectively.

surface. Moreover, the energy profile is numerically consistent with previous experimental results. It was also found that near the interface, migration diffusion is difficult due to strong structural constraint from the Si crystal side. The highest energy is 2.37 eV for the initial structure, and the energy drops to −1.47 eV when interstitial SiO reaches the surface. This diffusion path we found consists of 10 steps of O vacancy transfer, 15 steps of Si coordination number conversion, and 1 step of Si bond order conversion. It should be noted that Si and O belonging to SiO interstitaial at the final structure is different from those at the starting structure. SiO interstitial moves with sequentially kicking the neighboring Si and O like a billiards, and the kicked-out Si and O become new interstitial SiO, while Si and O belonging to the old intersititial SiO are absorbed as a part of the oxide.

So far, we have reported that, by the first-principles molecular dynamics method, the migration and diffusion of atoms in Si-rich $SiO_2$ is enhanced under compressive strain, [3] and by the first-principles nudged-elastic-band (NEB) method, the migration and diffusion of the O vacancies in $SiO_2$ is conversely reduced. [4] Therefore, we have speculated that the movement and diffusion of atoms in $SiO_2$, which has a large Si composition, is governed not by the movement and diffusion of O vacancies but by the Si coordination number conversion due to interstitial SiO. Our results are numerically consistent with these calculation results, which supports our speculation, and suggests the importance of the behavior of interstitial SiO in Si oxidation.

In this calculation, the barrier height in each elementary process is not calculated yet. For this reason, the comparison of our results with the experimental results and our previous computational results is unfortunately still insufficient. We are planning to calculate barrier heights by using the first-principles NEB method, and to compare numerical values much more in detail.

## References

[1] H. Kageshima, T. Akiyama, and K. Shiraishi, Matter. Sci. Semicon. Process. **162** (2023) 107527 (7 pages).

[2] https://azuma.nims.go.jp

[3] H. Kageshima, Y. Yajima, K. Shiraishi, and T. Endoh, Jpn. J. Appl. Phys. **58** (2019) 111004 (11 pages).

[4] K. Yata and H. Kageshima, Jpn. J. Appl. Phys., **60** (2021) 035504 (6 pages).

# Exponent puzzle for metal-insulator transition in doped semiconductors

Yosuke HARASHIMA
*Division of Materials Science, Nara Institute of Science and Technology*
*Takayama-cho, Ikoma, Nara 630-0192*

The zero temperature conductivity is zero at low impurity concentrations, and it becomes finite at high impurity concentrations. A metal-insulator transition occurs at concentrations in between. This metal-insulator transition is a general phenomenon of quantum transport and is known to occur in many semiconductors. Understanding the mechanism of the metal-insulator transition leads to an understanding of the general theory of quantum transport.

Here, electrons are scattered by randomly configurated impurities, and the phases of wavefunctions are randomly shifted out. Those waves interfere each other and propagation is inhibited, resulting in the appearance of localized states. This is called Anderson localization and a metal-insulator transition driven by disorder is called Anderson transition. Anderson transition is a continuous transition, and the correlation length $\xi$ diverges at the transition point as $\propto |n - n_{\rm c}|^{-\nu}$. The critical exponent, $\nu$, which characterizes this divergence, plays an important role in understanding the physical characteristics of the system. Since the critical exponent is universal and independent of the details of the system, the critical exponent can be used to classify systems. In other words, when two systems have different critical exponents, it means that they have different intrinsic physical features and are completely different physical phenomena.

Although there have been several experimental reports on the critical exponent of the metal-insulator transition, the proposed mechanism has not yet been clarified. There are two values of $\nu \simeq 0.5$ and $\simeq 1.0$–$1.3$ that have been reported experimentally. This problem is called the "exponent puzzle" and the origin of descripancy has been studied for long time. One possible origin is the effect of carrier compensation due to unintentionally introduced impurities or lattice defects, but this has not been confirmed theoretically. The purpose of this study is to elucidate the exponent puzzle by conducting a theoretical analysis considering the compensation effect in order to clarify the essential factor that causes the descripancy in the critical exponent.

Figure 1 is a calculated electronic density in a randomly distributed impurity system. The calculation is based on the density functional theory and local density approximation. We performed electronic structure calculations of compensated systems with spin configurations by using a program code used in our previous work. Positive ions and negative ions are randomly distributed in three dimensional space. They represent donors and acceptors. We solve the electronic states such that charge neutrality is satisfied, i.e., the number of electrons is equal to the difference between the number of donors and acceptors.

We also have examined stable impurity configurations in doped systems. The results are opened in Refs. [1, 2].

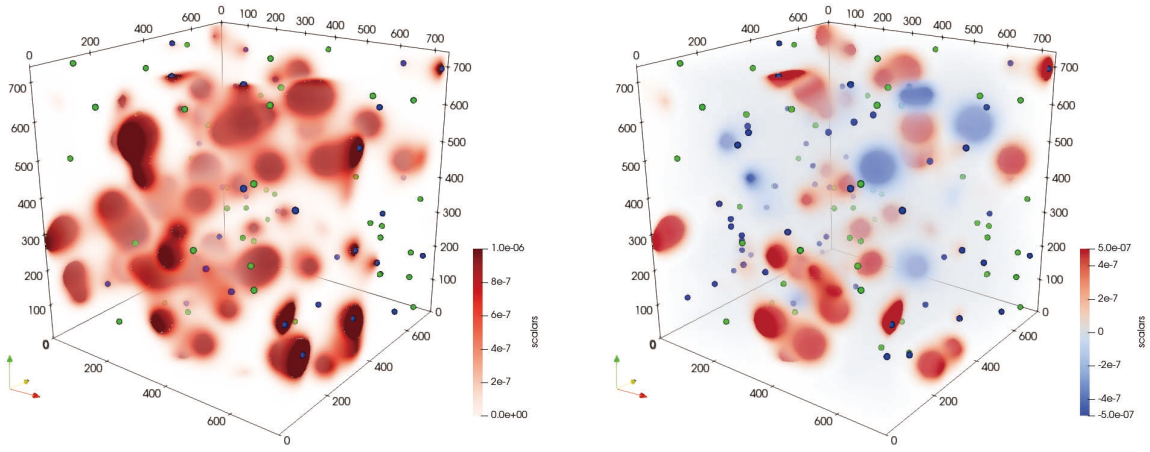


Figure 1: Total electronic density (left panel) and spin density (right panel) in a three dimensional system. Donor and acceptor ions are shown as blue and green points, respectively. In the right panel, positive and negative values denote up and down spin, respectively. The number of donor ions is 100, and that of acceptor ions is 50.

## References

[1] Y. Harashima, *et. al.*: IEEE Trans. Semicon. Man., accepted, DOI:10.1109/TSM.2023.3265658.

[2] Y. Harashima, *et. al.*: arXiv:2303.14891.

# Phase stability of high-entropy alloys

Yoko Yamabe-Mitarai

*Frontier Science Graduate School,*

*The University of Tokyo, Kashiwa-no-ha, Kashiwa, Chiba 277-8561*

High-entropy alloys (HEAs) comprise multiple elements with near-atomic composition and have high configurational entropy of constituent elements. HEAs have been attracted as new generation structural and functional materials since this new paradigm was proposed in 2004 [1]. Most of HEAs have a single face-center-cubic (fcc), body-center-cubic (bcc) structures or their mixtures. Due to limited slip system, hexagonal-close-pack (hcp) structure is expected to be high temperature materials. Large solid-solution hardening is also expected for HEAs. Then, we are applying to find HEAs with hcp structure experimentally and by using DFT calculation. Ti is focused on one of constituent element because Ti is used as high-temperature materials due to its small density and high specific strength. Phase stability of alloys was experimentally investigated, and a few alloys were found to be a hcp structure [2]. To investigate the effect of alloying elements and composition dependence on phase stability, phase stability change of bcc and hcp structures in Ti by 6 different alloying elements was calculated using DFT. Supercell model with 128 atoms was used to indicate solid solution phase. Special Quasirandom Structure was used to simulate random atomic position for ternary alloys as shown in Fig. 1. The internal coordinates was optimized using Quantum Expresso (QE). The total energy and density of states was calculated on the optimized coordinates. The formation energy calculated from the total energy indicated Al, Sn, Hf and Zr stabilized hcp structure, while Nb and Mo stabilized bcc structure.

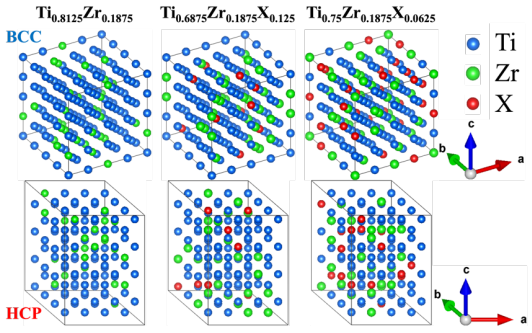


Fig. 1:BCC (top) and HCP (bottom) SQS model. X is alloying elements.

## References

[1] B. Cantor, I. T. H. Chang, P. Knight, A. J. B. Vincent, Mater. Sci. Eng. A, **375-377**, 213 (2004).

[2] Y, Yamabe-Mitarai, K. Yanao, Y. Toda, I. Ohnuma, T. Matsunaga, JALCOM, **911**, 164849 (2022).

# Analysis of the electronic structure of magnetic shape memory alloy by quasiparticle self-consistent *GW* approach

Masao OBATA[1,2]

[1]*Institute of Science and Engineering, Kanazawa University, Kanazawa, Ishikawa 920-1192*

[2]*Graduate School of Natural Science and Technology, Kanazawa University, Kanazawa, Ishikawa, 920-1192*

Magnetic shape memory (MSM) alloy of Ni-Mn-Ga [1] has attracted attention, showing an enormous magnetic field-induced strain (MFIS) effect of up to around 10%. This unique property comes from transitions among energetically close structures involving nanoscale-modulated structures attributed to magnetic and electronic stats. The MFIS effect is experimentally observed in the modulated structure of 10M or 14M, which has a long-period crystal structure in the *ab* plane. Although many investigations of the electronic structure based on density functional theory (DFT) within local density approximation or generalized gradient approximation (GGA) were reported, the results did not fully incorporate the experimental facts: for example, the stabilization mechanism of the modulated structures is still unclear. The importance of electron correlation effects in this material was recently indicated [2]. Thus, we employed one of the post-DFT methods, the quasiparticle self-consistent *GW* (QSGW) approach, to investigate the electronic structure beyond the GGA level. This study investigated the electronic and magnetic structure of the stoichiometric $Ni_2MnGa$ in austenite (cubic) and non-modulate martensite (tetragonal) phases by using the first-principles calculation package ecalj [3].

As the result of the QSGW calculation, the obtained energy level of the Ni $e_g$ orbital of the cubic phase is higher than that of GGA and almost coincided with the Fermi level. The state moves from the Fermi level in the tetragonal phase. This result strongly supports martensitic transformation due to the Jahn-Teller effect. Analysis of the Fermi surfaces nesting through generalized susceptibility revealed that its electronic state of cubic phase possesses intrinsic instabilities corresponding to 10M and 14M, which are not observed in the previous GGA calculation [4].

## References

[1] K. Ullakko et al, Appl. Phys. Lett. 69, 1966 (1996).

[2] M. Zelený et al., Mater. Des., **209**, 109917 (2021).

[3] https://github.com/tkotani/ecalj/

[4] M. Obata, T. Kotani, T. Oda, Phys. Rev. Materials 7, 024413 (2023)

# Calculation and comparison of adsorption energies of perfluoro molecules on Cu(111) and Cu(100) using first-principles calculation

Yuji Ohkubo, Misa Nishino, Hiroki Toujima, and Kouji Inagaki

*Graduate School of Engineering,*

*Osaka University, 2-1 Yamadaoka Suita, Osaka 565-0871*

Recently, increasing frequency of the digital signals is necessary because the amount of information communication is increasing. However, the higher the frequency is, the greater the transmission loss is. Therefore, polytetrafluoroethylene (PTFE) which has much low relative dielectric constant and dielectric loss tangent is considered as a suitable dielectric of high frequency printed wiring boards. However, PTFE has low adhesion property, so adhering PTFE to Cu is difficult. We have achieved generation of oxygen-containing functional groups and adhesion strength of 0.94 N/mm between PTFE and Cu when PTFE was He-plasma-treated at over 200℃ under atmospheric pressure[1]. Also, from the calculations of the adsorption energy between Cu(111) and fluorinated molecules, the functional groups containing COO˙ is possible to generate PTFE surface having high adhesion property. However, the calculations about Cu surface having different orientations are not performed. Therefore, in this study, the adsorption energy between Cu(100) and fluorinated molecules was calculated and the effect of orientation was investigated.

Our calculations were performed using the STATE (Simulation tool for atom technology) code with plane-wave basis and ultra-soft pseudopotential[2, 3]. The wave function and the charge density of cutoff energies were 36 and 400 Ry, respectively. Generalized gradient exchange-correlation functional based on Predew-Burke-Ernzerhof (PBE) was used for the exchange-correlation functional and DFT-D2 was used for the dispersion correction method[2, 3]. Cu surface was modeled Cu(100) 3×3 slab composed of 3 atomic layers. As the model of as-received PTFE, $CF_3$–$CF_3$ was calculated. In addition, $CF_3$–CF=O, $CF_3$–$CF_2$–OH, $CF_2$=$CF_2$, and $CF_3$–$CF_2$–OO˙ were calculated as the model of plasma-treated PTFE. These were the models of molecule containing oxygen-containing functional groups observed by C1s-XPS spectrum of the plasma-treated PTFE surface. Cu surface, fluorinated molecules, and adsorption systems were optimized then total energies were calculated. The adsorption energy was defined as the difference between the sum of total energy of Cu surface and fluorinated molecules and total energy of adsorption system.

**Fig. 1** shows the values of adsorption

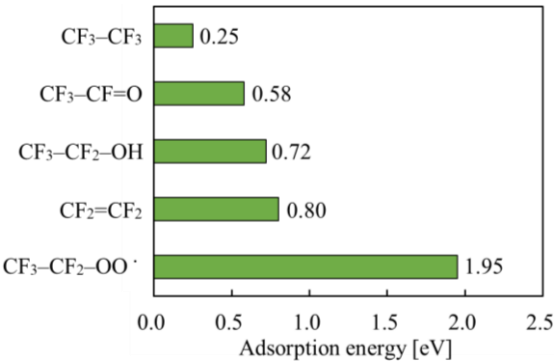


**Fig. 1** Values of adsorption energies.

energies by calculation. The values of adsorption energies of $CF_3$–$CF_3$, $CF_3$–CF=O, $CF_3$–$CF_2$–OH, $CF_2$=$CF_2$, and $CF_3$–$CF_2$–OO· was 0.25, 0.58, 0.72, 0.80, and 1.95 eV, respectively. In the case of molecules containing COO·, the adsorption energy was the highest and the molecule was stable as with Cu(100). However, in the case of Cu(111), the value of adsorption energy was 4.73 eV[2]. The value of Cu(100) was lower than that of Cu(111). **Fig. 2** shows the optimized atomic geometries for Cu(111) and Cu(100). In the case of Cu(111), $CF_3$–$CF_2$–OO· was dissociated to $CF_3$–$CF_2$–O· and O, then they adsorbed. However, in the case of Cu(100), $CF_3$–$CF_2$–OO· was adsorbed without dissociation. This is because the adsorption energy of Cu(100) was lower. The adsorption energy was calculated when $CF_3$–$CF_2$–OO· was dissociated and adsorbed on Cu(100) as shown in **Fig. 3**. The adsorption energy was 5.27 eV. This value was close to Cu(111). These results suggest that it is important to dissociate $CF_3$–$CF_2$–O· and O and adsorb to Cu surface, in order to further improve the adhesion property.

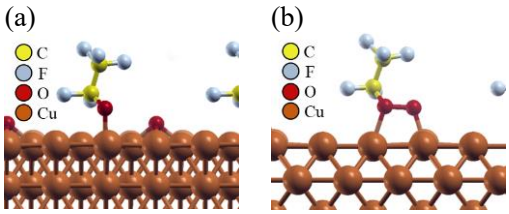


**Fig. 2** Atomic geometries for $CF_3$–$CF_2$OO· model (a) on Cu(111) and (b) on Cu(100).

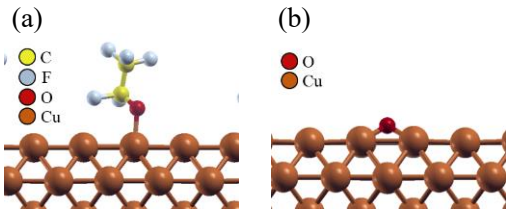


**Fig. 3** Atomic geometries for (a) $CF_3$–$CF_2$O· model and (b) O model.

In this study, the functional groups contributing to improvement in adhesion property were explored by calculating the adsorption energies between fluorinated molecules and Cu(100) and comparing the result of Cu(111). In the result of calculations, generating the functional groups containing COO· is possible to generate PTFE surface having high adhesion property, regardless of orientations. Also, in order to further improve the adhesion property, it is important to dissociate CO· and O and adsorb to Cu surface. On the other hands, the calculations of Cu(110) and copper oxide is not performed. Therefore, these calculations are needed in the future.

## References

[1] M. Nishino et al., INTERFINISH2020 Abstract, C-SEP06-004 (2021) 210.

[2] K. Toyoda et al., *J. Chem. Phys*. **132** (2010) 134703.

[3] K. Toyoda et al., *J. Nanosci. Nanotechnol*. **11** (2011) 2836–2843.

# Development of Efficient Evaluation Methods of Berry-phase-mediated Physical Properties for Large Scale Systems Using the First-principles LCPAO Method

Naoya YAMAGUCHI
*Nanomaterials Research Institute (NanoMaRi), Kanazawa University*
*Kakuma-machi, Kanazawa, Ishikawa 920-1192*

We did the following researches about the following topics in this subject: (i) development of a linear-combination-of-pseudo-atomic-orbital (LCPAO) scheme of a Berry phase method to apply electric fields [1] and (ii) development of a new scheme to the anomalous Hall and Nernst conductivity applicable to metallic systems [2].

For (i), we have developed a first-principles LCPAO scheme of a homogeneous and finite electric field method based on the modern theory of polarization and density functional theory (DFT), so that one can consider electric field effects even for periodic systems such as bulk insulators. We validated our scheme by calculating the electronic and static dielectric constants and Born effective charges of III-V and II-VI semiconductors and group IV insulating materials. The calculated values coincided with the reported computational values, and they were an agreement with the experimental values. For the Born effective charges, we confirmed that the values obtained from our scheme are consisted with those obtained from the finite difference method (i.e. numerical differentiation of electric polarization with respect to atomic positions.) The spin-orbit interaction (SOI) has a non-negligible influence on the dielectric constants of cases including the heavy elements. We applied our scheme with the SOI to evaluate the Born effective charges characterizing the bond properties, covalency and ionicity in new semi-stable phases of BiTeI including a wide-gap topological insulating phase [3]. Our LCPAO implementation will make it easy to investigate the electronic structures and physical properties under an electric field even for the large system including hundreds of atoms. In addition, we also developed the spin texture code for insulators under electric fields through the Berry phase scheme. We did test calculations by applying the spin texture code to bulk diamond. Bulk diamond is a system keeping the spatial inversion symmetry, but a strong electric field can break the symmetry to induce the spin splitting through the Rashba effect (see Fig. 1 and 2).

For (ii), we also developed the new evaluation scheme for the anomalous Hall and Nernst conductivity without constructing the Wannier functions or explicit evaluation of the Kubo formula [2]. We reproduced the intrinsic contribution of typical anomalous Hall systems such as body-centered-cubic iron. Our scheme has advantages of efficiency so that it is the non-iterative scheme unlike Wannierization. Therefore, our scheme can easily address not only large scale cases but also high-throughput calculations. We applied the scheme to evaluate the peculiar magnetic thermoelectricity in the ferrimagnetic phases of $MnBi_2Te_4$ layers [4]

and a ferromagnetic superlattice of tetragonal-$Fe_2Si$, that is, Hapkeite [5]. We also developed another version of the scheme based on the improved tetrahedron method. It is possible to directly evaluate the pure term of anomalous Nernst conductivity (ANC) even for systems with too low the Curie temperature to obtain the convergent values of the pure term through the numerical differentiation of the anomalous Hall conductivity with respect to the chemical potential.

We also improved the spin texture code by changing the eigenvalue solver so that k-space spin density matrices can be calculated more stably and efficiently. Through the code, we investigated a hydroxyl-terminated diamond surface and found the electronic structure with the persistent spin helix that is important to spintronic applications [6].

We implemented them to the OpenMX code [7], and they will be released in the future.

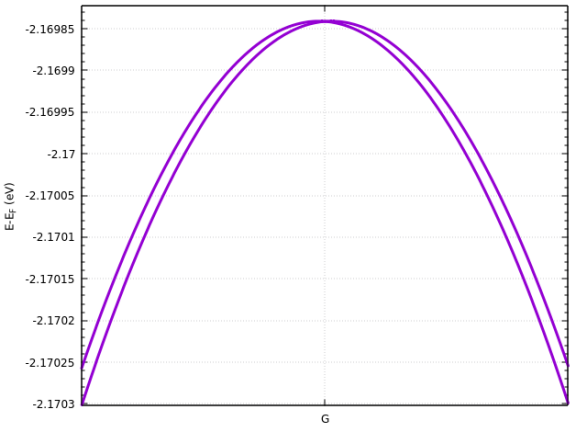


Figure 1: Band structure with the Rashba spin splitting around the valence band top at the Γ-point induced by an electric field of 3.5 GV/m perpendicular to one of the faces in bulk diamond. The momentum shift $\Delta k$ was $2.99 \times 10^{-4}$ Å$^{-1}$, and the induced electric polarization was 12.58 $\mu$C/cm$^2$.

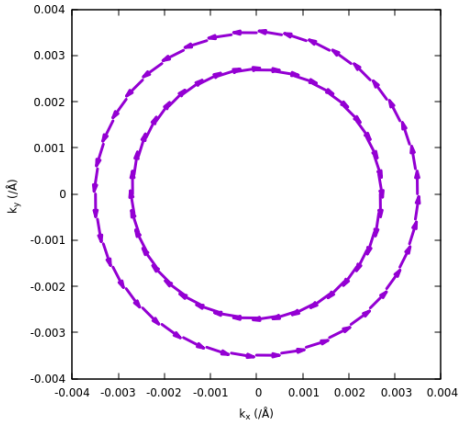


Figure 2: Spin texture for the Rashba spin splitting around the valence band top at the Γ-point induced by an electric field of 3.5 GV/m perpendicular to one of the faces in bulk diamond. The length and direction of arrows represent the magnitude and direction of the expectation values of the spin every k-point, respectively.

## References

[1] N. Yamaguchi, F. Ishii, Comput. Phys. Commun. **280**, 108487 (2022).

[2] H. Sawahata, N. Yamaguchi, S. Minami, F. Ishii, Phys. Rev. B **107**, 024404 (2023).

[3] Y. Zhang, N. Yamaguchi, H. Sawahata, F. Ishii, Appl. Phys. Express, in press, DOI: 10.35848/1882-0786/acccd3 (2023).

[4] Y. Morishima, N. Yamaguchi, H. Sawahata, F. Ishii, Appl. Phys. Express **16**, 043003 (2023).

[5] T. Tominaga, N. Yamaguchi, H. Sawahata, F. Ishii, Jpn. J. Appl. Phys. **62**, SD1019 (2023).

[6] H. P. Kadarisman, N. Yamaguchi, F. Ishii, Appl. Phys. Express **16**, 023001 (2023).

[7] http://openmx-square.org.

# Electronic structure investigation of the $Ba_2PrBiO_6$ photocatalyst

Kazume NISHIDATE
*Faculty of Science and Engineering, Iwate University*
*Ueda 4-3-5, Morioka, Iwate 020-8551*

A large number of double-perovskite oxides, $A_2B'^{\,III}B''^{\,V}O_6$, have been studied due to their intriguing physical and chemical properties originating in their mixed valence nature. Where the small cations occupy the $B$' and $B$" sites with the different valencies. Recently, it was found that the $Ba_2PrBiO_6$ double-perovskite has a photo catalytic activity in the visible light. However, theoretical analysis on the electronic properties of its surface has not been performed. In this work, we perfomed the first-principles density functional computation of the surface of $Ba_2PrBiO_6$. We used the **Quantum ESPRESSO** (QE) package. We applied the Heyd-Scuseria-Ernzerhof hybrid functional (HSE06) formalism for the exchange-correlation to evaluate the band gap as well as the work function.

The surface electronic states are calculated using a slab model, which consists of stacked three unit cells and the vacuum region of 16 Å . Where $Ba_2PrBiO_6$ has the Ba-O and the Pr-Bi polar planes alternately stacked in one direction. The top and the bottom planes are terminated with the same polar surface to prevent the artificial dipole-dipole interactions over the cyclic boundary. The work function $\phi$ is defined as the difference between the vacuum level ($\phi_{\mathrm{vac}}$) and the Fermi level $E_F$ (Figure. 1).

We also performed the Born-Oppenheimer Molecular Dynamics simulations of the slab to investigate its reactiveness to the water. In this stage, we used the PBE functional for the exchange-correlation and employed only the Γ

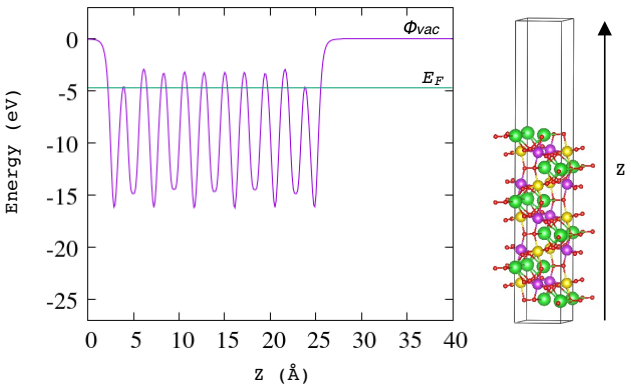


Figure 1: Averaged electronic potentials for the Ba-O polar plane along the $Z$ axis of the super-cell.

point for the reciprocal space integration to suppress the computational time. Temperature was regulated to be 300 K throughout the simulation time steps using the velocity scaling method. And $H_2O$ molecule was placed at 5 Å over the Ba-O surface. There are three stages in the adsorption process. First, a $H_2O$ molecule approaches the surface as the result of the Coulomb interaction between the oxygen and the surface Ba atoms (I). Then, the oxygen atom makes a bond with Ba by releasing its hydrogen atom and thereby forming a hydroxyl group. The released hydrogen atom also makes a bond with the oxygen atom of the slab (II). In this adsorption process, two hydroxyl groups were created. We have been focusing on the detailed analysis on the calculated results.

# Theoretical Study on Electronic Properties in New Nanoscale Surfaces and Interfaces

Katsuyoshi KOBAYASHI
*Department of Physics, Ochanomizu University*
*2-1-1 Otsuka, Bunkyo-ku, Tokyo 112-8610*

We theoretically studied the photoemission spectra of $V_5Se_8$ monolayers. $V_5Se_8$ is a layered material composed of $VSe_2$ layers and V intercalant layers. It is known that bulk $V_5Se_8$ has an antiferromagnetic structure at low temperatures. However, a recent experiment showed ferromagnetic behavior in $V_5Se_8$ thin films [1]. We studied the electronic structure of $V_5Se_8$ monolayers in 2022 [2].

It may be assumed that $V_5Se_8$ monolayers have a structure composed of two $VSe_2$ layers and a V intercalant layer as shown in Fig. 1(a). However, a recent experiment [3] showed a structure that the surfaces of $V_5Se_8$ monolayers are covered with the V intercalant layers. In order to investigate the surface structures of $V_5Se_8$ monolayers we performed a density-functional calculation. We used the program package VASP for density-functional calculations.

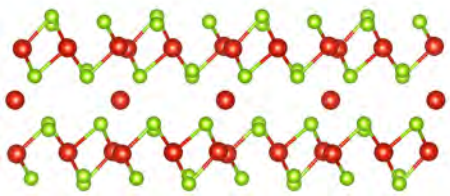

Figure 1: Side view of the atomic structure of a $V_5Se_8$ monolayer.

Figure 2 shows the photoemission intensity calculated for the structure shown in Fig. 1. The photoemission intensity is a calculated band structure weighted by the $\mathbf{G}_{\parallel} = 0$ component of wave functions, where $\mathbf{G}_{\parallel}$ are the components of reciprocal lattice vectors parallel to the surface. This is due to that the wave functions in vacuum regions are mainly connected to the $\mathbf{G}_{\parallel} = 0$ component in materials. The band structure is calculated in a nonmagnetic state because the photoemission experiment was performed at room temperatures. The energy bands are broadened with a width of 0.1 eV. The calculated intensity has good agreement with the experimental one [2]. The photoemission intensity calculated for the structure with a V-adsorbed surface is similar to Fig. 2. But, Fig. 2 better reproduces a characteristic feature of the experimental band dispersion. Therefore it is concluded that the $V_5Se_8$ monolayers in the experiment of Ref. [2] have the structure shown in Fig. 1.

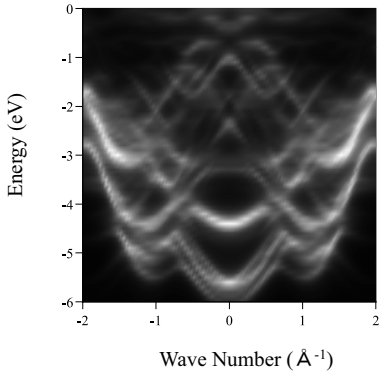


Figure 2: Calculated photoemission intensity of the $V_5Se_8$ monolayer. The origin of energy is the Fermi energy. The wave number is along the direction perpendicular to the side view plane in Fig. 1.

## References

[1] M. Nakano *et al.*: Nano Lett. **19** (2019) 8806.

[2] K. Sumida *et al.*: Phys. Rev. B **106** (2022) 195421.

[3] Q. Meng *et al.*: Phys. Status Solidi RRL **16** (2022) 2100601.

# Interaction of magnetic metal phthalocyanines with metal surfaces

Tetsuya ARUGA
*Department of Chemistry, Kyoto University*
*Kitashirakawa-Oiwakecho, Sakyo, Kyoto 606-8502*

Phthalocyanine ($C_{32}H_{18}N_8$) is a planar molecule with an extended $\pi$ electron system. Two hydrogen atoms in the central "hole" of the molecule can easily be substitutid by a 2+ transition metal ion, giving rise to metal phthalocyanine ($M$Pc), and thus the molecule has two significant electronic motifs, conjugated $\pi$ electrons of a Pc molecule and an open-shell $d$ orbital of the central transition metal ion.

In this work, we studied the interaction and interface structure of the metal phthalocyanine molecules adsorbed on bi-layer indium films fabricated on Si(111)-(1× 1) substrate [1] and studied the ordering and the interaction of the molecule with the indium substrate. Experimentally, the adsorbed molecules form a two-dimensional close-packed lattice. No second adsorption layer is formed at room temperature, suggesting that the energy gain associated with the planar stacking is weak. On the other hand, the interaction of phthalocyanine with In substrate appears to be strong, as implied by the formation of close-packed lattice and the stability against the temperature increase.

In order to clarify the origin of the molecule–surface interaction, we performed a computational work by using VASP [2, 3, 4, 5]. We used optB86b-vdW van der Waals density functional (vdW-DF) [6] in order to treat the interaction of the extended $\pi$-electron system of the molecule with the sp bands of the In substrate. We used DFT+U method in order to properly describe the electronic state of the $Fe^{2+}$ ion in the molecule. The value of $U$ was set so that the magnetic moment of the $Fe^{2+}$ ion in a free FePc molecule is reproduced.

The adsorption structure predicted by the calculation indicates that the adsorption is governed by two different molecule–surface interactions. The structure obtained by the minimization of the total energy indicated two significant characteristics that are not found in $H_2$Pc, which is only weakly bound to the surface by vdW-like interaction with the metallic substrate. Firstly, the Pc molecule is deformed to a bowl-like structure with the molecular center down and closest to the substrate. Secondly, the Fe ion in the center of the molecule protrude further downward and appears to be associatively interacting with the In atoms below. These characteristics are not found for $H_2$Pc and CuPc, suggesting that these are characteristic to $M$Pc molecules with open $d$-shell $M$ ions. The interaction between the molecule and the substrate may differ depending on the number of $d$ electrons. The effect of these interaction on the superconductivity of the In film[7, 8] is intriguing.

## References

[1] E. Rotenberg et al.: Phys. Rev. Lett. **91**, 246404 (2003).

[2] G. Kresse and J. Hafner, Phys. Rev. B **47**, 558 (1993); ibid. 49, 14251 (1994).

[3] G. Kresse and J. Furthmüller, Comput. Mat. Sci. **6**, 15 (1996).

[4] G. Kresse and J. Furthmüller, Phys. Rev. B **54**, 11169 (1996).

[5] G. Kresse and D. Joubert, Phys. Rev. **59**, 1758 (1999).

[6] J. Klimeš et al., Phys. Rev. B 83, 195131 (2011).

[7] T. Zhang et al., Nat. Phys. 6, 104 (2010).

[8] T. Uchihashi et al., Phys. Rev. Lett. 107, 207001 (2011).

# In-plane interaction of $\pi$-conjugated molecules

Tetsuya ARUGA
*Department of Chemistry, Kyoto University*
*Kitashirakawa-Oiwakecho, Sakyo, Kyoto 606-8502*

Phthalocyanine ($C_{32}H_{18}N_8$) is a planar molecule with a 2D extended $\pi$-conjugated electron system. Two hydrogen atoms in the central "hole" of the molecule can easily be substituted by a 2+ transition metal ion, giving rise to metal phthalocyanine ($M$Pc).

The adsorption of $M$Pc on single-crystalline metal surfaces has been studied by several groups. In these works, irrespective of the substrate, $M$Pc molecules form ordered two-dimensional lattice, which has common characteristics as below: (1) the molecule adsorbs with its molecular plane parallel to the surface, (2) the molecules form nearly square lattice that is commensurate with the substrate lattice, (3) the molecules are rotated in plane by $\sim 20^\circ$ from the symmetrical direction of the substrates and forms a staggered structure.

The first point is understood by the fact that the adsorption is mostly governed by the van der Waals interaction between the surface and the molecule. The second point is due to the shape of the molecule, which prefers square-like lattice to maximize the coverage. The third point is not obvious. Previous authors claimed that this is due to the direct chemical interaction of N atoms in the molecule with a particular atoms of the surface, which however has not been confirmed by quantitative methods.

In this work, we studied (1) the interaction among metal phthalocyanine molecules adsorbed on bi-layer indium films fabricated on Si(111)-(1$\times$ 1) substrate [1] and (2) the interaction among metal phthalocyanine molecules in the same geometry as in (1) but without the substrate.

The total energy was computed by using VASP code [2, 3, 4, 5] as a function of azimuthal rotation angle. The total energy for the case (1) shows decrease with increasing azimuthal angle from $0^\circ$ and get minimum at $\sim 20^\circ$. Further increase of the azimuthal angle leads to the divergence of the total energy due to the direct contact of the neighboring molecules. The energy minimum at $\sim 20^\circ$ is in good agreement with the observation. The case (2) gave rise to an almost the same angular dependence but with the amplitude 60% $\sim$ 70% of the case (1).

The results indicates that the rotation of the molecule is induced by the intermolecular interaction, which most probably is dipole-dipole interaction between C-H groups of the molecule. The energy minimum is achieved when the C-H bonds with opposite direction of neighboring molecules approach with each other most closely. Our calculation does not indicate any significant contribution of the direct interaction of molecular N atom with the substrate. The reduced interaction in the case (2) suggests that the image dipoles induced in the substrate (bilayer In) are smaller in strength, which is most probably due to the ultra-thinness of the substrate In bilayer, in which the metallicity of the lower In layer is mostly lost due to the bonding with substrate Si atoms.

## References

[1] E. Rotenberg et al.: Phys. Rev. Lett. **91**, 246404 (2003).

[2] G. Kresse and J. Hafner, Phys. Rev. B **47**, 558 (1993); ibid. 49, 14251 (1994).

[3] G. Kresse and J. Furthmüller, Comput. Mat. Sci. **6**, 15 (1996).

[4] G. Kresse and J. Furthmüller, Phys. Rev. B **54**, 11169 (1996).

[5] G. Kresse and D. Joubert, Phys. Rev. **59**, 1758 (1999).

# Atomic structures and electronic properties of nanocarbon-based materials

Yoshitaka FUJIMOTO
*School of Engineering, Kyushu University*
*Moto-oka, Fukuoka-city, Fukuoka 819-0395*

Graphene is one of the most promissing materials for electronics devices such as field effect transistors and molecular sensors. It has been reported that the boron atom in graphene could act as a reactive site for the adsorptions of environmetally polluting NO and $NO_2$ molecules. [1] Furthermore, the B atoms in bilayer graphenes are also reported to enhance the adsorption properties of several molecules, leading to the possibility to fabricate the highly sensitive $NO_x$ sensors. [2, 3, 4] However, it might be difficult to detect harmful CO molecules using B-doped graphene. Carbon nanotube (CNT) is also expected to be one of the most promising materials for development of sensors due to its high surface-to-volume ratio of one-dimensional nanostructures and its excellent electrical conductivity. Here, we report the adsorption properties of environmetally polluting $NO_x$ and harmful CO molecules on CNTs. [5]

We examine the atomic structures of B-doped and N-doped (10,0) CNTs without the adsorbed molecules. The zigzag nanotubes such as the (10,0) CNT have two kinds of C-C bonds around each atom. In the B-doped case, two kinds of the B-C bond lengths are found to be 1.47 Å and 1.50 Å. In the case of the N-doped case, the C-N bond lengths are 1.37 Å and 1.40 Å. The B-C bond lengths are much longer compared with two kinds of the C-C bond lengths (1.40 Å and 1.41 Å) in a pristine (10,0) CNT, while the two kinds of N-C bond lengths are slightly shorter than the corresponding C-C bond lengths. In addition, the B-C and N-C bond lengths are longer and shorter than those of B-doped graphene (1.47 Å) and N-doped graphene (1.40 Å), respectively.

We also examine the adsorption properties of various molecules including environmentally toxic molecules on the B-doped and N-doped (10,0) CNTs. Table I lists the adsorption energy and the distance between the molecule and the B (C) atom in the B (N)-doped (10,0) CNTs. For the B-doped cases, CO, NO, $NO_2$ and $O_2$ molecules are found to be strongly adsorbed with relatively large adsorption energies as well as the short binding distances, while $CO_2$ and $N_2$ molecules are weakly adsorbed. For the N-doped CNT, it is reported that the adsorption energy of a H atom at a neighboring C atom is larger than that at the dopant N atom itself. Here, we examine the adsorption of all six types of molecules at the C atom sites next to N-dopant atoms in the N-doped CNTs. It is found that only NO and $NO_2$ molecules are strongly adsorbed, while the adsorption energies of the remaining four molecules (CO, $CO_2$, $O_2$, and $N_2$) are relatively small and at the same time the binding distances between molecule and C atom are relatively long. It is interesting that the adsorption energies of these molecules on the B-doped and N-doped CNTs are overall larger than those on the B-doped and N-doped graphenes, respectively, due to the curvature effects of the nanotubes.

In summary, we have investigated the adsorption effects of environmentally toxic molecules on atomic structures and energetics of B-doped and N-doped (10,0) CNTs based on the first-principles electronic structure study. The B-doped CNTs can strongly bind with CO, NO, $NO_2$ and $O_2$ molecules, while $CO_2$ and $N_2$ molecules are not strongly but weakly

Table 1: Adsorption energy $E_a$ (eV) and distance $d$ (Å) from the B (C) atom for each molecule adsorbed on B (N)-doped (10,0) CNTs.

| | | NO | $NO_2$ | CO | $CO_2$ | $O_2$ | $N_2$ |
|---|---|---|---|---|---|---|---|
| B-doped | $E_a$ | −1.32 | −1.82 | −0.46 | −0.06 | −0.36 | −0.23 |
| | $d$ | 1.75 | 1.56 | 1.54 | 2.77 | 1.59 | 2.71 |
| N-doped | $E_a$ | −0.97 | −0.91 | −0.08 | −0.07 | −0.13 | −0.23 |
| | $d$ | 1.66 | 1.53 | 2.74 | 2.75 | 1.70 | 2.84 |

adsorbed. The N-doped CNTs can strongly bind with only NO and $NO_2$ molecules in air. The environmentally harmful NO and $NO_2$ and toxic CO molecules are individually detectable by using B-doped and/or N-doped CNTs.

## References

[1] Y. Fujimoto and S. Saito, Jpn. J. Appl. Phys. **58**, 015005 (2019).

[2] Y. Fujimoto and S. Saito, Chem. Phys. **478**, 55 (2016).

[3] Y. Fujimoto and S. Saito, Appl. Surf. Sci. Adv. **1**, 100028 (2020).

[4] Y. Fujimoto, Mod. Phys. Lett. B **35**, 2130001 (2021).

[5] Y. Fujimoto and S. Saito, J. Electrochem. Soc. **169**, 037512 (2022).

# Effects of Element Substitution on Molecular Packing and Band Structures in Single-component Molecular Conductors with Canted Antiferromagnetism

So YOKOMORI

*Department of Chemistry, College of Science*

*Rikkyo University, 3-34-1 Nishi-Ikebukuro, Toshima, Tokyo, 171-8501*

We have investigated the syntheses and electronic properties of single-component molecular conductors exhibiting canted antiferromagnetism (CAF). The occurrence of CAF in molecular conductors is exceedingly uncommon [1], and as a result, the corresponding structure-property relationships have yet to be fully disclosed. Recently, a single-component molecular conductor with CAF was produced through the use of a diethoxybenzene-fused gold dithiolene complex (see Fig. 1). In this investigation, we centered our attention on the high modulatory capability of substituting elements in the complex. To enable an effective evaluation of the systematic structure-property relationship in CAF molecular conductors, we computed the band structures of element-substituted complexes to aid in the synthesis of new compounds.

Band calculations for three kinds of element-substituted complexes (as depicted in Fig. 1) were executed using OpenMX 3.9 software. For these calculations, the crystal structures were optimized by means of the DFT-D3 method which involved vdW- and dispersion energy-correction, by exchanging the original elements in the crystal structure of the diethoxybenzene-fused gold dithiolene complex with other elements. As a result, the following findings were unveiled: substituting Se led to a reversal of the magnitude of $J_1$ and $J_2$, as well as a decrease in the bandwidth. This suggests that Se substitution would significantly affect the CAF behavior. In the S-substituted complex, an interaction appeared along the inter-conducting layer direction and the bandwidth increased. This outcome implies that the dimensionality of spin-spin interaction is stronger than that of the original complex, and thus, the transition temperature of CAF ordering transition could be expected. For the N-substituted complex, no significant changes were observed except for a slight decrease in the bandwidth. Therefore, it can be concluded that the priority of synthesizing this complex is low. Accordingly, in this investigation, we successfully gained insights into which complexes should be synthesized next.

## References

[1] R. Ishikawa *et al.*, *J. Phys. Soc. Jpn.*, **87**, 064701 (2018).

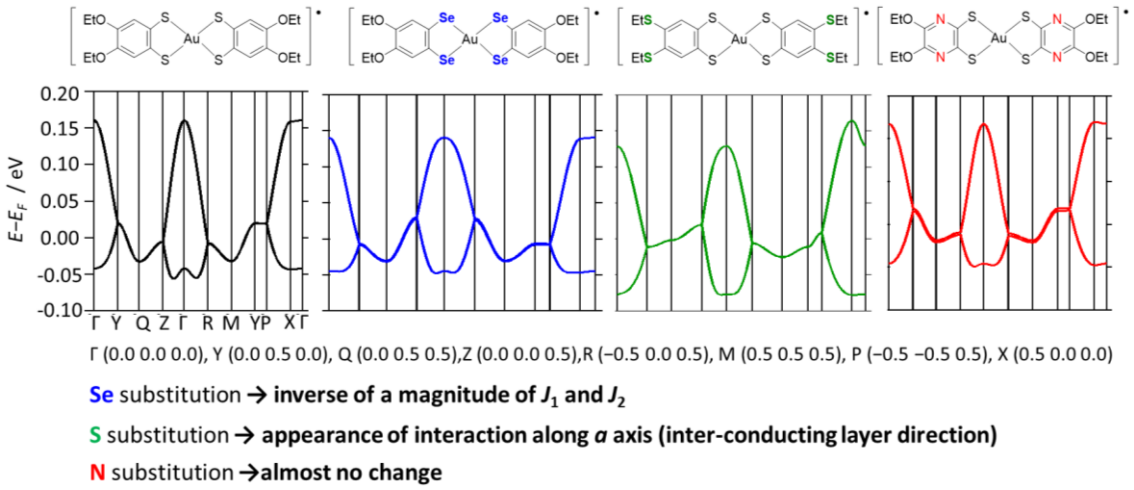


Fig. 1. Structural formula of the complex of CAF molecular conductor and newly designed element-substituted complexes, and calculated band structures. An explanation of band structure changes for each result are shown in the bottom.

# First principles study on the band structures of high entropy compounds

Hidetomo USUI

*Department of Physics and Materials Science,*

*Shimane University, Nishikawatsu-cho, Matsue, Shimane 690-8504*

High-entropy alloys are alloys containing five or more elements at one site. Recently, high-entropy compounds have attracted much attention not only from a mechanical point of view but also as functional materials such as thermoelectric and superconducting materials.[1,2] We have investigated the electronic structure of a high entropy compound *M*Te (*M* = Ag, In, Sn, Pb, Bi), which exhibits robustness of superconductivity to external pressure[3, 4]. This year, we calculated the electronic band structure of *M*Te in the rock salt typed crystal structure using the VASP package within the PBE-exchange correlation functional with spin-orbit coupling included. We used a 2×2×2 supercell of MTe ($Sn_{16}Pb_{16}Te_{32}$, $In_{11}Pb_{10}Bi_{11}Te_{32}$, $In_8Sn_8Pb_8Bi_8Te_{32}$, and $Ag_8In_6Bi_6Sn_6Pb_6Te_{32}$). We calculated the site arrangement of *M* atoms using the special-quasi random structure implemented in Alloy Theoretic Automated Toolkit. We took a *k*-mesh spacing of 0.1 $Å^{-1}$ and a cut-off energy of 330 Ry. The unfolded electronic band structure of *M*Te is shown in Fig. 1. It is found that the band structure for M=Sn, Pb exhibits sharp spectral lines, but for M = Ag, In, Sn, Pb, and Bi, due to a mixture of various elements, spectral weight is reduced. It can be understood that substitution by elements in other groups can suppress the quasiparticle lifetime but can control the band structure around the Fermi level.

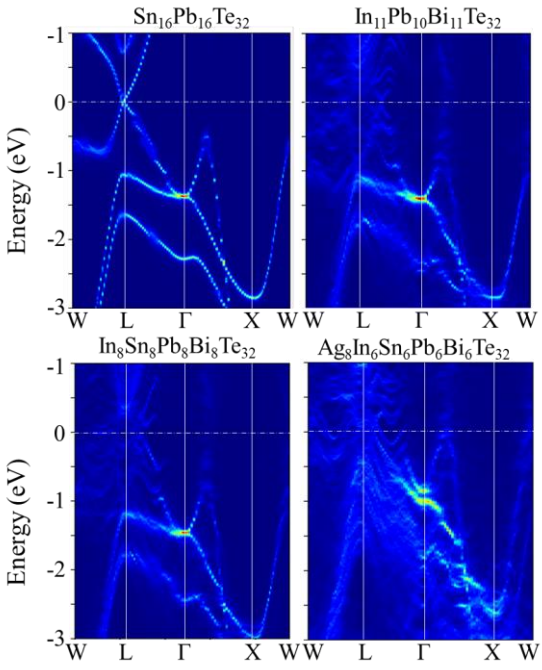


Fig. 1: Electronic band structure of MTe

## References

[1] B. Jiang et al., Science **371**, 830 (2021)

[2] P. Koželj *et al*., Phys. Rev. Lett., **113,** 107001 (2014).

[3] Md R. Kasem *et al*., Sci. Rep **12**, 7789 (2022)

[4] Y. Mizuguchi *et al*., Mater. Today Pnys. **32**, 101019 (2023)

# First-principles study of interfacial magnetic structure in topological magnets

Susumu MINAMI[†,‡], Yuta TOGA[†], Katsuhiro TANAKA[†]
[†]*Department of Physics, Univeristy of Tokyo, Hongo, Bunkyo-ku, Tokyo 113-0033*
[‡]*Department of Mechanical Engineering and Science, Kyoto University, Nishikyo-ku, Kyoto 615-8540*

Topological magnetic materials such as $Mn_3Sn$ and $Mn_3Ge$ exhibit unique properties due to their particular band structures (Berry phase) and have attracted attention as core elements for antiferromagnetic spintronics devices. Recently, finite tunneling magnetoresistance (TMR) effects have been observed at room temperature in the magnetic tunneling junctions (MTJs) with $Mn_3Sn$ [1] and $Mn_3Pt$ [2], increasing the demand for research on the interface in antiferromagnetic MTJs.

This research project employed the QUANTUM ESPRESSO, a first-principles calculation code, to analyze the $Mn_3Ge$/MgO MTJ and its interface, which have the non-collinear magnetic configuration. Due to its non-collinear magnetic structure, the computational cost and output data volume significantly increased, and the convergence worsened, necessitating the use of the ISSP Supercomputer.

The study presents the magnetic moments of the Mn layers at the vacuum surface and within the MgO multilayer film, with energy-based optimization of interfacial distances. Figure 1 shows the layer dependence of the magnetic moments of the Mn atoms. While the magnetic moments increase at the vacuum surface due to increased electron localization, this increase is not observed at the MgO interface for some Mn positions. The different surface states influence the magnetic moments of Mn atoms inside the interface.

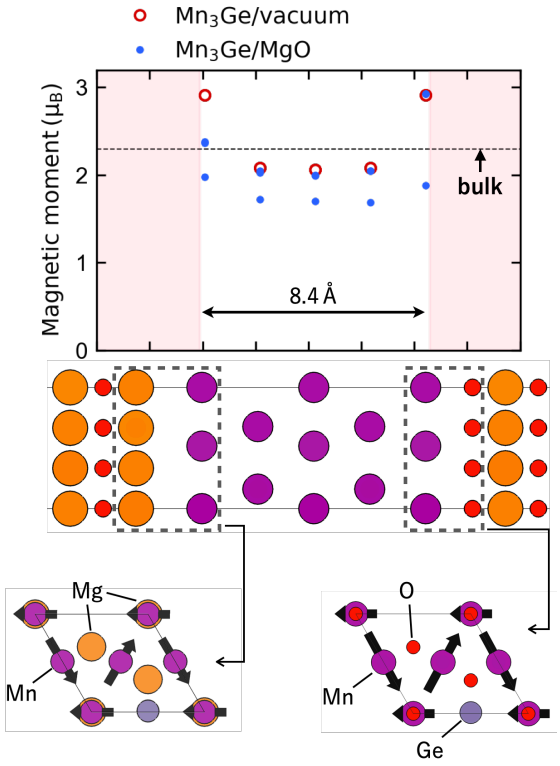


Figure 1: Magnetic moments of the Mn atoms near the surface and the interface.

As the performance of MTJs is influenced by the magnetic state near the interface, future research will investigate charge transfer, film thickness dependence, and their relation to the tunnel conductance.

## References

[1] X. Chen *et al.*, Nature **613**, 490 (2023).

[2] P. Qin *et al.*, Nature **613**, 485 (2023).

# RSDFT calculation of atomic displacements detected through energy dissipation measurement on noncontact atomic force microscopy

Toyoko ARAI[1], Takahiro Kato[1], Jun-Ichi Iwata[2], Atsushi Oshiyama[3]

[1]*Graduate school of Natural Science and Technology, Kanazawa University, Kanazawa, Ishikawa, 920-1192*

[2] *Institute of Innovative Research, Tokyo Institute of Technology, Tokyo 152-8550*

[3]*IMaSS, Nagoya University, Nagoya, Aichi 464-8601*

We had experimentally found that, when non-contact atomic force microscopy (nc-AFM) images showed the high resolution for the individual adatoms on a Si(111)-(7×7) surface, the simultaneously obtained energy dissipation signal increased in close proximity over the hollow sites surrounded by a Si adatom and a Si rest atom with a dangling bond per each [1]. To clarify the role of the dangling bonds on the Si adatom and the Si rest atom, we partially terminated the Si(111)-(7×7) surface with H, leading to chemical inactivation of some of the dangling bonds. Some distinct bright regions in the dissipation image were lost, which coincided with the hollow sites next to H-terminated rest atoms and/or H-terminated adatom (Fig. 1). This indicates that the dangling bonds of the rest atom and adatom around the

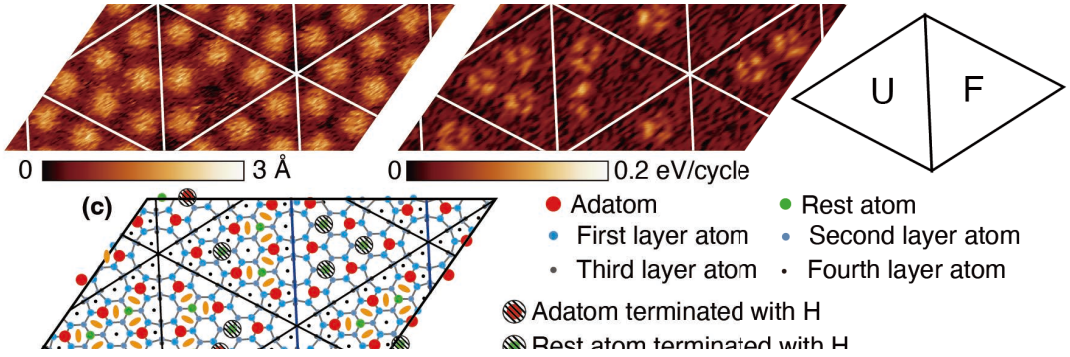


with a cantilever of $f_0$ = 199 kHz. The image area was 6.0×3.5 nm$^2$, sheared at 35° for drift compensation. The white meshes denote the unit cells. (c) Atomistic model of the H-terminated Si(111)-(7×7). The estimated H-terminated sites are hatched.

hollow site can change the dissipation. In this study, to elucicate the phenomena, the forces between Si tip and Si(111)-(7×7) surface were calculated using real-space density functional theory (RSDFT) [2]. RSDFT is a first-principles program developed by Oshiyama and Iwata, which uses a real-space difference method and a pseudopotential method.

First, we optimized the structure of a Si(111)-(7×7) reconstructed surface consisting of 298 Si atoms, the back surface of which was terminated with 49 H atoms, and the structure of a [001]-oriented Si tip by RSDFT; the tip consisted of 30 Si atoms having a Si dimer at the tip apex, the back side of which was terminated with 18 H atoms, named “dimer tip” [3]. Next, we calculated the structure changes and the forces acting between the tip and the Si surface during tip approaching and retracting over the hollow site at the separations between the tip apex atom and the Si adatom on the surface from 5.0 to 2.0 Å, as shown in Fig. 2. The atom structure and the force-distance curves exhibited hysteresis. The greyed area surrounding by the force-distance curve should correspond to the nonconservative dissipation energy that was experimentally measured. Furthermore, the calculations with Si(111)-(7×7) surface with H-terminated rest atoms or H-terminated adatom did not show such hysteresis during one cycle of tip travel. This calculation for the hydrogen termination was also in good agreement with the experiment.

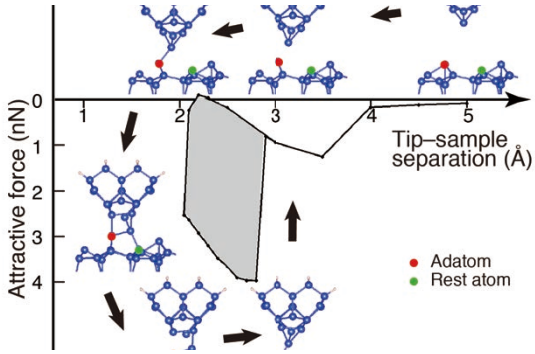


Fig. 2 Force–distance (separation) curve with the optimized structures of the Si tip and Si(111)-(7×7) surface, calculated by RSDFT.

## References

T. Arai, R. Inamura, D. Kura, and M. nitori, Phys. Rev. B **97**, 115428 (2018).

J.-I. Iwata, D. Takahashi, A. Oshiyama, T. ku, K. Shiraishi, S. Okada, and K. Yabana, J. mput. Phys. **229**, 2339 (2010).

P. Pou, S. A. Ghasemi, P. Jelinek, T. iosky, S. Goedecker and R. Perez, notechnology **20**, 264015 (2009).

# A study of nickelate superconductors in first-principles

Hirofumi SAKAKIBARA
*Department of Engineering,*
*Tottori University, Tottori, Tottori 680-8525*

A recently discovered superconductor $NdNiO_2$ [1] attracts broad interests among the field of low-temperature physics because of its cuprate-like electronic structure. Namely, $NdNiO_2$ has infinite layered structure to have monovalent nickel atoms in which the electron configuration is $3d^9$, the same with the copper site of cuprates. This striking similarity motivates researchers to compare the nickelates and the cuprates for the purpose of unveiling the high-$T_c$ pairing mechanism [2].

However, the nickelates also have several dissimilarity: (1) $T_c$ is lower (up to 20K, where that of cuprates are up to 135K), (2) no long-range magnetism on the vicinity of superconducting dome in the carrier-temperature phase diagram, (3) no superconductivity in the bulk materials [3]. Even the feature (1) and (3) is still under intense debate, however, some consensus for (2) is being formed. Namely, since the energy bands formed by lanthanoid atoms overlaps with 3*d* bands of nickelate unlike cuprates, the self-doped holes from the lanthanoid site break magnetic order so that no magnetic phase is observed [4,5].

A theory is proposed to interpret the feature (1) based on the combination of many-body theory and first-principles calculation [5]. In the theory, by applying fluctuation exchange approximation (FLEX, Ref. 6) on a seven-orbital model constructed in first-principle with maximally localized Wannier orbital [7], it is revealed that the first-principles Hubbard $U$ obtained in constrained random phase approximation (cRPA, Ref. 8) is much stronger than that of cuprates. Therefore, the self-energy induced by spin-fluctuation damps quasi-particles weight to degrade $T_c$. The main reason of this larger $U$ in the nickelates is the much larger energetical splitting $\Delta_{dp}$ between nickel ion and oxygen.

Considering the above numerical results, we can easily imagine that $T_c$ in nickelates goes up by applying hydrostatic pressure that may lower $U$ and/or $U/t$ values, where $t$ is the hopping integrals of the $3d_{x2-y2}$ orbitals between nearest neighbor sites. In this research, to confirm this idea, I have constructed the seven-orbital model by obtaining stable crystal structure under hydrostatic pressure (0GPa--20GPa). For computational details, quantum espresso package (QE, Ref. 9) and RESPACK [10] officially implemented in the system B are employed and the bulk crystal structure is

assumed. It is found that the *U/t* value becomes smaller by hydrostatic pressure, where the value of *t* is simply scaled by the lattice constant along the *a*-axis (along the layers). By performing FLEX calculation assuming such smaller *U/t* value, the larger $\lambda$, the eigenvalues of Eliashberg equation, is obtained. This means that $T_c$ may get higher if the hydrostatic pressure is applied on nickelates.

Interestingly, the value of *U* itself remains almost constant (or, slightly gets larger) when the applied pressure gets stronger. To give deeper insight to this result, I have calculated the value of *U* in cRPA by varying the valence of nickel atoms. Namely, I have performed virtual crystal approximation (VCA) for two Sr-doped systems $La_{1-x}Sr_xNiO_2$ and $Nd_{1-x}Sr_xNiO_2$, where the nickel's valence is simply formulated as $1+x$. In this calculation, the value of *U* gets smaller as the valence gets smaller. By constructing the so-called *d-p* model considering all of the 3*d*-orbitals and 3*p*-orbitals, it is found that $\Delta_{dp}$ is roughly scaled by the valence of nickel atoms.

To summarized, I have performed mainly two types of calculations employing QE+ R ESPACK to capture the possible variation of *U/t* value in the infinite layered nickelates: structural optimization under pressure and VCA calculation nickelates. The value of *U/t* may decrease by hydrostatic pressure while *U* itself possibly remains constant. By VCA calculation, it is found that *U* itself is roughly scaled by the valence of nickel atom. These results give us a hint to optimize *U/t* value for seeking higher $T_c$ materials such as cuprates. As a future task, I will challenge to theoretically explain the recent experimental result of praseodymium nickelate thin firm in which $T_c$ gets significantly higher by applying pressure [11].

# References

[1] D. Li et al., Nature (London) 572, 624 (2019).

[2] M. R. Norman, Physic 13, 85 (2020).

[3] Q. Li et al., Communications Materials 1, 1(2020).

[4] A. S. Botana and M. R. Norman, Phys. Rev. X 10, 011024 (2020).

[5] H. Sakakibara et al., Phys. Rev. Lett. 125, 077003 (2020).

[6] N. E. Bickers et al., Phys. Rev. Lett 62, 961 (1989).

[7] N. Marzari and D. Vanderbilt, Phys. Rev. B 56, 12947 (1997).

[8] F. Aryasetiawan, Phys. Rev. B 70, 195104 (2004).

[9] P. Giannozzi et al., J. Phys.: Condens. Matter 21, 395502 (2009)

[10] K. Nakamura et al., Comp. Phys. Comun. 261, 107781 (2021).

[11] N. N. Wang et al., Nat. Commun. 13, 4367 (2022).

# Growth mechanism of $MoS_2/MoO_2$ core shell nanowires studied by DFT calculation

Toshihiro SHIMADA

*Division of Applied Chemistry, Faculty of Engineering, Hokkaido University,*

*Kita 13 Nishi 8, Kita-ku, Sapporo, Hokkaido 060-8628*

We have experimentally found that $MoS_2$ nanotubes with rectangular cross sections are grown in certain conditions by chemical vapor deposition. After the detailed study of the growth conditions using turbulent flow, we found that $MoO_2$ nanowires are formed first, and the surface is sulfurized to make $MoS_2/MoO_2$ core shell nanowires as shown in electron microscopy images in Fig. 1[1].

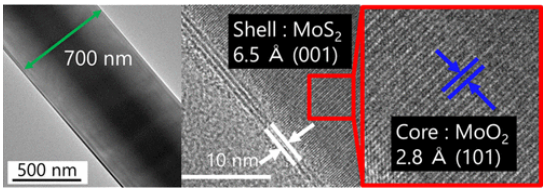


Fig. 1 : Transmission electron microscope images of $MoS_2/MoO_2$ core shell nanowires. (reprinted with permission: American Chemical Society[1])

In order to elucidate the mechanism of this growth feature, we used DFT calculation (VASP). We studied the surface energies of the precursor $MoO_2$ (Table 1 and Fig. 2).

We found that the surface energies do not so differ with each other as to explain the nanowire growth by surface stability effect. We concluded that the $MoO_2$ nanowires are grown from some other precursors with excess oxygen.

Table 1. Surface Energies of Various Faces of $MoO_2$

| Faces | Surface energy /Jm$^{-2}$ |
|---|---|
| (011) | 2.25 |
| (101) | 1.84 |
| (110) | 2.36 |
| (-111) | 2.55 |
| (11-1) | 2.55 |
| (010) | 1.30 |
| (-101) | 1.75 |

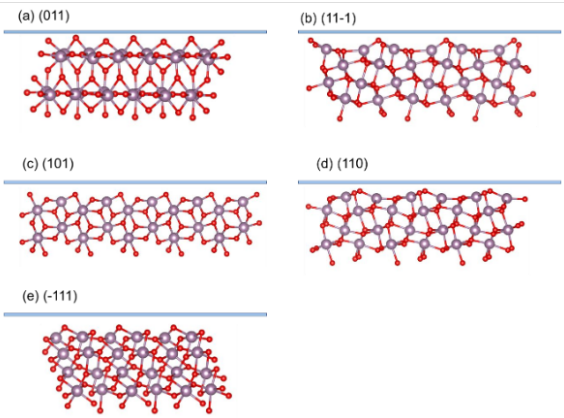


Fig. 2 : Optimized structures of $MoO_2$ surfaces.

## References

[1] M. Goto, I. Yamane, S. Arasawa, T. YAnase, S. Yokokura, T. Nagahama, Y.Chueh, Y. Shin, Y. Kim and T. Shimada, ACS Omega **7**, 39362-39369 (2022).

# First-principles calculation of graphitization of diamond surface and its exfoliation process

Kouji INAGAKI

*Graduate School of Engineering, Osaka University*

*Yamadaoka 2-1, Suita, Osaka 565-087*

Diamond is a material with a highest mechanical strength and has been applied as cutting tools. However, serious wear occurs in cutting ferrous materials. As the cause, oxidation of the diamond surface, diffusion of carbon atoms into iron, graphitization and its exfoliation, etc. have been proposed, but they are still unclear. It is well known that graphite is generally formed on diamond surfaces. The wear is most likely caused by the exfoliation of this graphite layer. Following the study of diamond surface oxidation [1], graphitization and its exfoliation on diamond surfaces were investigated. We found that for a simple diamond-Iron interface, the diamond surface is not significantly changed by the separation of the interface. However, it was found that the C-C bonds at the diamond-Fe interface can be cleaved by Fe with a low activation barrier of less than 1 eV, as in catalytic reactions. Furthermore, at the interface where the reaction takes place, the graphitized layer is found to be exfoliated by the subsequent interface separation. This study will be submitted for publication soon.

## References

[1] J. I. Enriquez, F. Muttaqien, M. Michiuchi, K. Inagaki, M. Geshi, I. Hamada, and Y. Morikawa Carbon 174, 36-51 (2021).

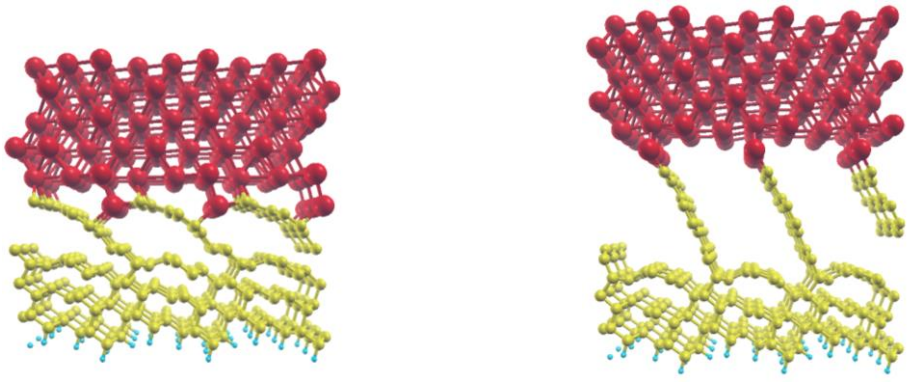

(a) (b)

Fig. 1: Peeling of graphitized diamond surface in the separation of diamond and iron interface. Yellow and red spheres represent carbon and Fe atom. (a) Formed interface between stepped diamond (111) and Fe (110) surfaces. (b) After interface separated.

# AB type 2D materials database construction by DFT

Masahiro FUKUDA

*Institute for Solid State Physics,*

*The University of Tokyo, Kashiwa-no-ha, Kashiwa, Chiba 277-8581*

Demand for high-throughput calculations based on the DFT is increasing rapidly due to developments in data science and artificial intelligence. In our previous research, we constructed a structure map [1] and a web-based database [2] of $AB_2$ type monolayers by high-throughput DFT calculations using OpenMX. These data also provided on the ISSP data repository [3].

In this project, a program code to perform high throughput electronic and phonon band and DOS calculations by using OpenMX [4] and Alamode [5] with Spglib [6] were developed to construct materials database. In addition, the developed job scripts for massive parallel bulk jobs using GNU parallel package enable us to perform high throughput DFT calculations on the ISSP supercomputer ohtaka effectively and comfortably.

These developed program codes are applied to the AB type structure map (Fig.1) construction, basic materials database construction [7], material search for quaternary metal hydrides [8], and AFM simulations to determine atomic arrangement of Si adatom on the Silicene/Ag(111) surface [9]. $Au_2X$ type monolayer study is currently being carried out.

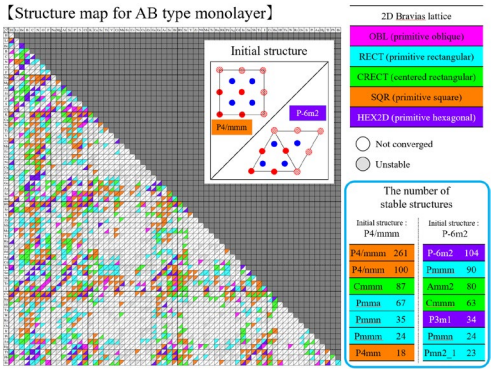


Fig.1: Structures map of AB type monolayers.

## References

[1] M. Fukuda, J. Zhang, Y.-T. Lee, T. Ozaki, Mater. Adv., 2, 4392 (2021).

[2] Structure map and database of $AB_2$ type 2D materials (www.openmx-square.org/2d-ab2/).

[3] Structure map of AB2 type 2D materials by high-throughput DFT calculations

[4] OpenMX, http://www.openmx-square.org

[5] T. Tadano, Y. Gohda, and S. Tsuneyuki, J. Phys.: Condens. Matter 26, 225402 (2014).

[6] Spglib package (github.com/atztogo/spglib/).

[7] OpenMX database of Atoms using standard basis sets, OpenMX database of bulks using standard basis set

[8] R. Koshoji, M. Fukuda, M. Kawamura, T. Ozaki, Phys. Rev. Materials 6, 114802 (2022).

[9] Y. Adachi, Z. Runnan, W. Xinbo, M. Fukuda, T. Ozaki, Y. Sugimoto, Applied Surface Science, 157336 (2023).

# Exploring dopants aiming at achieving high bulk insulation in Pb-based topological insulators

Yuki TOKUMOTO

*Institute of Industrial Science,*

*The University of Tokyo, Komaba, Meguro-ku, Tokyo 153-8505*

$PbBi_2Te_4$ topological insulator (TI) is considered as one of the promising candidates for future spintronics material with a large spin current density. However, experimental studies of its surface transport properties have not yet been reported, owing to a lack of bulk insulating crystals. So far, we achieved bulk insulating states in $Pb(Bi,Sb)_2Te_4$ topological insulators by tuning compositional ratio of Bi and Sb [1]. Furthermore, we recently revealed that In doping for $Pb(Bi,Sb)_2Te_4$ TI is effective for further lowering carrier concentrations and bulk resistivities, which is considered to be die to a localized impurity band that acts as a charge buffer occurring inside the bulk band gap.

We carried out band structure calculation of $PbBi_2Te_4$ based on density functional theory (DFT) using Vienna ab-initio simulation package (VASP) version 6.2.1. We adopted generalized gradient approximation (GGA) proposed by Perdew, Burke, and Ernzerhof (PBE) as the exchange correlation energy functional. For all calculations, we included spin-orbit coupling (SOC). We obtained band gap of 115 meV for $PbBi_2Te_4$, which is much lower than experimentally reported value ~230 meV. In order to estimate band gap more accurately, the Heyd-Scuseria-Ernzerhof (HSE06) and HSE03 hybrid functional was employed. As a result, band gap was further underestimated. We found that the HSE is not effective for accurate estimation of band gap of narrow-gap semiconductors.

In future, we plan to calculate electronic structure of In-doped $Pb(Bi,Sb)_2Te_4$ using GGA-PBE including SOC.

## References

[1] Y. Hattori, Y. Tokumoto, and K. Edagawa: Phys. Rev. Mater. **1** (2017) 074201.

# Dielectric function calculations in rare-earth-metal monoxides

Takayuki MAKINO

*Research Center for Development of Far-Infrared Region,*

*University of Fukui, Bunkyo, Fukui, 910-8507*

Oxygen in metals is an important and rapidly expanding field of theoretical and experimental study. One of studies is characterization of the electronic structure of metals containing a dissolved oxygen or ordered oxide phases. Compared to the oxygen adsorption metals, an ordered oxygen is more manageable because it can be handled within the framework of band theory. Owing to the metastable open-shell divalent ions, the ground state of rare-earth-metal monoxides are not trivial. In some cases, it results in a metallic ground state, while in other cases, it yields in an insulator. These monoxides can be viewed as prototypes of the large number of metallic monoxides which form in the same NaCl structure.

According to pioneering work [1], lineshape analysis of the spectra revealed that a certain rare-earth monoxide is an indirect-type narrow-gap Mott-Hubbard insulator, having a gap of *ca*. 0.2 eV [1]. The author has tried to reproduce this in the DFT- based calculation. To open the gap, there are representative three knocks. First, we should introduce an on-site Coulomb energy, which is otherwise known as the Hubbard energy [2]. Recently this has been turned out to be able to determine in *ab-initio* manner. Second, we should also introduce the Hubbard energy on the oxygen. We used a HP executable included in the Quantum ESPRESSO package [3]. Finally, the introduction of the antiferromagnetic order tends to open the gap even with smaller Hubbard energy. To reconcile with this experimental result (paramagnetic), we should assume the antiferromagnetic order is effective only within a short-range. To check this, we confirmed that the antiferromagnetic insulating ground state is energetically favored.

The Hubbard energy for the rare-earth is evaluated to be *ca.* 1 eV. The calculation under this condition yielded in a metallic ground state. If we wish to open the gap, the Hubbard energy must be 9 eV. This fact made the authors reconsider about a ground state of our rare-earth-metal monoxide system.

We used a 50 Ry energy cutoff for the electronic wave functions and a small smearing width of 0.02 Ry which required a 6×6×6 *k*-point mesh. Adopted pseudopotentials are based on the projector augmented-wave method.

We introduced that (*U*p) on the *p* orbital of the oxygen atom. The value of *U*p (*ca*. 21 eV) has been determined by the self-consistent linear response approach. To implement the antiferromagnetic ordering, we adopted four-atom-configuration including two cations with up and down spins.

The judgement for narrow-gap insulator has been based on the absorption spectrum. The Drude edges are less noticeable viewed in this spectrum. It is no longer true in cases of photoconductivity or dielectric function, dominated by large Drude tails. The authors [1] have presented the dependence of the electrical conductivity on the partial oxygen pressure during the growth. They identified that the specimen showing the lowest conductivity should be classified into a narrow-gap insulator rather than a (correlated) bad metal. We speculate that even this one should be a gapless compound. In the measurement of thin films, it is impossible to accurately and precisely quantify the small optical absorption coefficient region. Accurate information in the region of small coefficients is essential for determining whether it is indirect or direct transitions. This condition cannot be satisfied in the case of a metastable substance that can only be synthesized in a thin film state. Then, we are interested in the Hubbard energy dependence of the optical conductivity and dielectric function spectra for this compound.

We are now calculating various types of the optical spectra for this rare-earth-metal monoxide. We used the Wannier executable included in the Quantum ESPRESSO package [3]. By increasing the Hubbard energy in the DFT calculation, the infrared divergence in the conductivity spectrum is suppressed. On one hand, in addition to the optical absorption spectrum, we are now constructing the optical conductivity spectrum based on the same set of the measured data, i.e., transmissivity and reflectivity.

## References

[1] K. Kaminaga *et al.*, ACS Omega 2018, 3, 10, 12501.

[2] B. Himmetoglu *et al.*, Phys. Rev. B. 84, 115108 (2011).

[3] P. Giannozzi *et al.*, J. Phys.: Condens. Matter 21, 395502 (2009).

# Electronic Structure and Fermiology of $d$- and f-electron compounds

Isaki Kinjo, Juno Iraha, Yasutomi Tatetsu[1], and Takahiro Maehira[2]
*Graduate school of Engineering and Science, Nishihara, Okinawa 903-0213*
[1]*Center for Liberal Arts Education, Meio University, Nago, Okinawa 905-8585*
[2]*Faculty of Science, University of the Ryukyus, Nishihara, Okinawa 903-0213*

The calculation for an energy band structure of TaC was carried out using a relativistic linear augmented-plane-wave (RLAPW) method. $f$ electrons are assumed to be itinerant and the calculation is performed in the paramagnetic phase. Note here that relativity should be taken into account, because of large atomic numbers of the constituent atoms. The spatial shape of the one-electron potential is determined in the muffin-tin approximation, and we use the exchange and correlation potential in the local density approximation (LDA)[1]. The crystal structure of TaC is categorized into the NaCl-type structure, which is characterized by the space group Fm3m[2, 3, 4, 5, 6, 7]. The iteration process for solving the Dirac one-electron equation starts with the crystal charge density that is constructed by superposing the relativistic atomic charge densities for neutral atoms Ta($[\mathrm{Xe}]4f^{14}5d^{3}6s^{2}$), and C($2s^{2}2p^{2}$), where [Xe] symbolically indicate the closed electronic configuration for xenon. In Figure 1, we show the energy band structure for TaC along the symmetry axes in the Brillouin zone in the range from 0.0 to 2.0 Ryd. First note that in the vicinity of the Fermi level $E_{\mathrm{F}}$ located at 1.2860 Ryd., there occurs hybridization between Ta 5$d$ and C 2$p$ states. The number of the valence electrons in the APW sphere partitoned into the angular momenta is 0.612 ($s$), 0.993 ($p$), 3.327 ($d$) and 0.381 ($f$) in the Ta sphere, 0.570 ($s$), 1.044 ($p$), 0.006 ($d$) and 0.000 ($f$) in the C sphere. There are 2.012 valence electrons outside the APW sphere in the primitive cell.

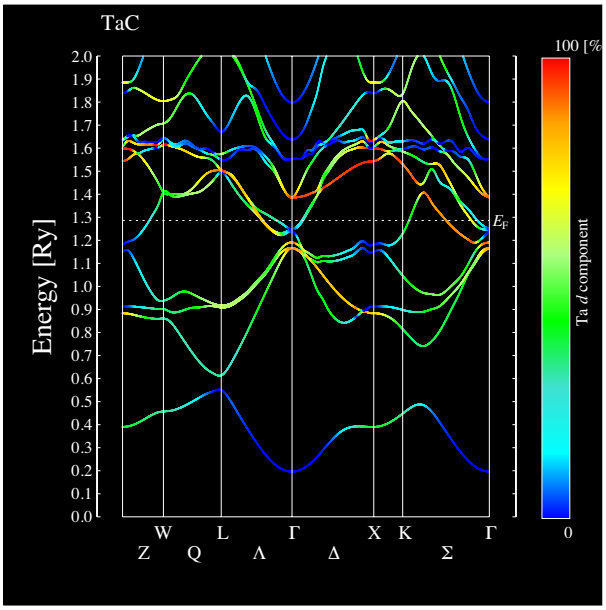


Figure 1: Energy band structure for TaC calculated by using the self-consistent RLAPW method.$E_{\mathrm{F}}$ indicate the position of the Fermi level.The contribution of Ta-5$d$ electrons to the Energy band is illustrated by color, where red corresponds to 100% (Ta-5$d$).

Now we discuss the Fermi surfaces of TaC. Since the lowest four bands are fully occupied, as shown in Figure 1, the next three bands are partially occupied, while higher bands are empty. Namely, the 5th, 6th, and 7th bands crossing the Fermi level construct the hole or electron sheet of the Fermi surface, as shown

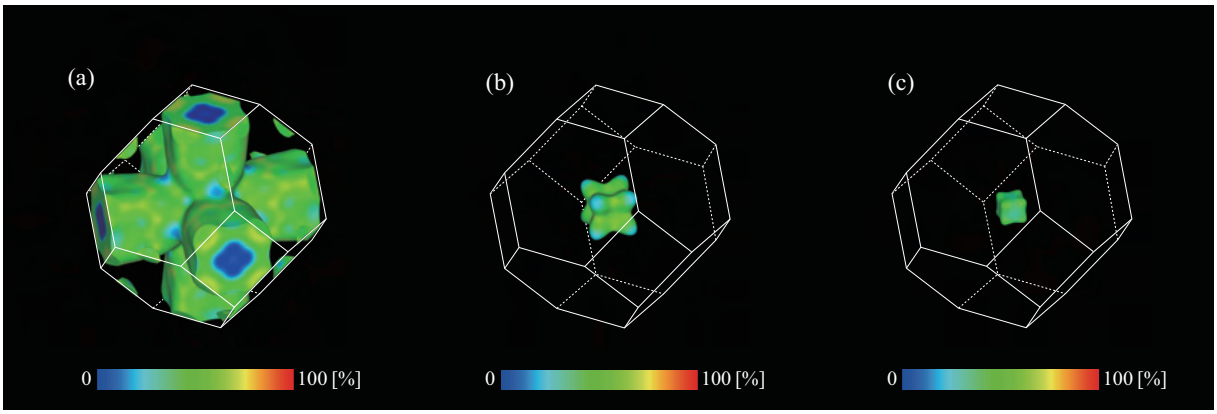


Figure 2: Calculated Fermi surfaces of TaC for (a) 5th band hole sheets, (b) 6th band electron sheets, and (c) 7th band electron sheets. Colors indicate the amount of 5$d$ angular momentum character on each sheet of the Fermi surface. Red-shift indicate the increase of the admixture of $d$ electrons. The center of the Brillouin zone is set at the Γ point.

in Figure 2. Note that the Fermi surfaces from 5th, 6th, and 7th bands are shown in (a), (b), and (c). The Fermi surface from the 5th band consists of two equivalent small hole sheets centered at the K points and one large hole sheet centered at the Γ point. The 5th band constructs a large hole sheet centered at the Γ point, which exhibits a complex network consisting of big "arms" which lie along the edges of Brillouin zone, as observed in Figure 2(a). The hole sheet centered at the Γ point is shown in Figure 2(b). It looks like a rounded cube having eight bumps in the <111> directions. The 7th band constructs a small electron sheet, which is centered at the Γ point is shown in Figure 2(c). The total number of holes is not equal to that of electrons, which represents that TaC is a uncompensated metal. Let us turn our attention to the analysis of the angular momentum character of the states forming various sheets of the Fermi surface. Here the most important quantity is the amount of Ta 5$d$ character, which is the partial density of states for Ta 5$d$ state for each point in $k$-space on the Fermi surface. This quantity is visualized in Figure 2, where the admixture of the Ta 5$d$ states is increased as the red shift in color, as shown in the scale diagram. The broad variation of the color from blue to red reflects a substantial variation of the 5$d$ contribution for different groups of states which change in the range from about 15% to about 80%. However, this distribution is different from part to part on the Fermi surface.

## References

[1] O. Gunnarsson and B. I. Lundqvist: Phys. Rev. B 13 (1976) 4274.

[2] Nowotny H., and Kieffer R.Z.: Metallkd. **38** (1947) 257.

[3] Allen P.B., and Cohen M.L.: Phys. Rev. Lett. B29 (1972) 1593.

[4] Klein B.M., and Papaconstantopoulos D.A.: Phys. Rev. Lett. B32 (1974) 1193.

[5] Mulokozi A.M.: J. Less-Common Met. **79** (1981) 139.

[6] Allison C.Y., Finch C.B., Foegelle M.D., and Modine F.A.: Solid State Commun. **68** (1988) 387.

[7] Frisk K., and Fernandez Guillermet A: J. Alloys Compd. **238** (1996) 167.

# Electronic Structure of 2D Boron Monosulfide

Masayuki TOYODA
*Department of Physics, Tokyo Institute of Technology*
*Ookayama 2-12-1, Meguro-ku, Tokyo 152-8551*

Ultrathin two-dimensional (2D) materials are a class of nanomaterials that exhibit unique mechanical, physical and chemical properties. Among them, 2D materials consisting of boron has been now attracting increasing interest due to their polymorphic properties. Recently, ultrathin boron monosulfied (BS) nanosheets have been successfully synthesized by the physical exfoliation of rhombohedral boron monosulfide (r-BS) [1]. The discovery of the BS nanosheets raised attention to their bulk layers. We have investigated the electronic and lattice vibrational properties of r-BS by performing first-principles density-functional theory (DFT) and density-functional perturbation theory calculations. The results agrees well with the experimental measurements including the infrared absorption spectroscopy [2] and microfocused angle-resolved photoemission spectroscopy [3]. By incorporating with the experiment, we have revealed the detailed electronic structure of r-BS and its *p*-type semiconductivity. In this study, we have utilized the efficient parallel computing power of ISSP Supercomputer System B (ohtaka).

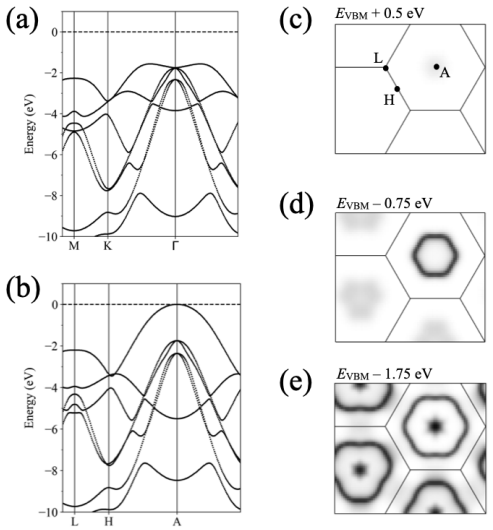


Figure 1: Calculated electronic structure of r-BS. The band dispersion (a and b) and 2D cross-section at different energies (c, d, and e) are shown.

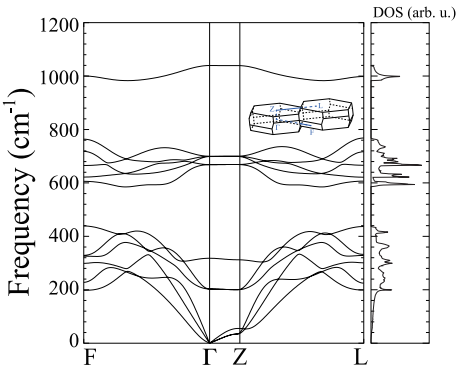


Figure 2: Calculated phonon dispersion of r-BS.

## References

[1] H. Kusaka, R. Ishibiki, M. Toyodaet al., J. Mater. Chem. A **9**, 24631-24640 (2021); J. Mater. Chem. A **10**, 4999 (2022).

[2] 0 N. Watanabe, K. Miyazaki, M. Toyoda et al., Molecules **28**, 1896 (2023).

[3] K. Sugawara, H. Kusaka, T. Kawakami et al., Nano Lett. **23**, 1673-1679 (2023).

# Exploration of exotic surface sites for catalyst informatics

Yoyo HINUMA

*National Institute of Advanced Industrial Science and Technology (AIST)*

*1-8-31, Midorigaoka, Ikeda, Osaka 563-8577*

Surface point defects of metal oxides, for instance O vacancies, have a dominant effect on heterogeneous catalysis. The Mars-Van Krevelen mechanism is one of the most frequently encountered catalytic process. In one example, O vacancies on a metal oxide catalyst surface act as reaction sites. The energy minimum required to remove O from a surface, which is denoted as the surface O vacancy formation energy ($E_{\mathrm{Ovac}}$), can be used to rationalize and predict catalytic performance in such a catalytic process. Calculation of $E_{\mathrm{Ovac}}$ requires a slab-and-vacuum model with sufficient spacing between O vacancies, hence some estimation of $E_{\mathrm{Ovac}}$ from less costly calculations, such as slab-and-vacuum model calculations with minimum cell size and even bulk calculations, will be effective in screening materials for a given purpose.

Computational exploration of previously unknown reactive sites is a powerful strategy for emergence of new catalytic reactions. The surface energies of experimentally known perovskite oxides with B-site cations with redox capability (Ti-Fe). The A-cation and B-cation terminated (100) surfaces were studied. The symmetry was reduced by hand to obtain the lowest energy structure. Fig. 1 shows $CaTiO_3$ shown in the setting of a 2x2x2 supercell of the cubic 5-atom.

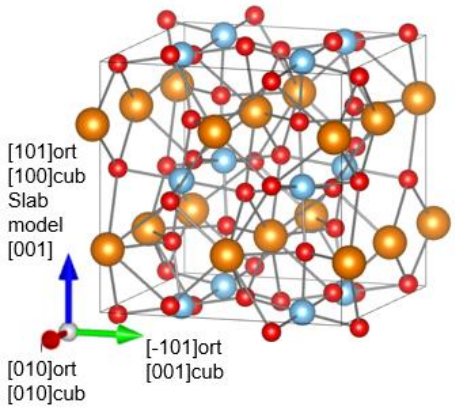


Fig. 1. Crystallographic conventional cell of CaTiO3 (space group type Pnma, number 62). Orange, blue, and red balls represent Ca, Ti, and O, respectively. The directions of basis vectors are shown in the orthorhombic (ort) and cubic (cubic) settings/

The following trends were found:

-Metallic compounds had small $E_{\mathrm{Ovac}}$; less than 2 eV and 1 eV for A-cation and B-cation terminated surfaces, respectively.

-Ti-containing compounds had very high $E_{\mathrm{Ovac}}$ with more than 4 eV for the B(Ti)-cation layer. This result implies that Ti-containing perovskites are not very reactive.

-Other compounds were in-between, with the trend of higher A-cation layer $E_{\mathrm{Ovac}}$ when the B-cation contains more 3*d* electrons

# Atom correlation of two-dimensional Cu-Ni alloy on the Ni(110) and Cu(110) surfaces

Tsuneo FUKUDA

*Division of Electronics and Physics, Graduate School of Engineering,*

*Osaka Metropolitan University, 3-3-138 Sugimoto, Sumiyoshi-Ku, Osaka 558-8585*

Copper-Nickel alloys are ubiquitous materials, and they are widely used as construction materials such as piping and various coinages. Cu and Ni are both simple fcc metals and form a uniform solid solution without any intermetallic compounds. The interaction energy is, however, known to be positive, resulting in a spinodal decomposition which has been established theoretically and experimentally. However, due to the lack of definitive experimental studies, no quantitative evaluation of the interaction energy between Cu and Ni has ever been conducted.

Here we studied atom correlation of two-dimensional alloy on Ni(110) and Cu(110) surfaces. The (110) face of fcc metals have a unique one-dimensional atom chain, and we have experimentally demonstrated one-dimensional attractive interaction of Cu-Cu on the Ni(110) surface.[1] The aim of this study is to evaluate the interaction energy from the first-principles. We used VASP, and by changing the Cu-Cu (Ni-Ni) distance on the Ni(110) (Cu(110)) surfaces the interaction energies were extracted as a function of Cu-Cu (Ni-Ni) distance (n). Atomic structures and the calculation parameters are respectively shown in the inset of Fig. 1 and Table 1.

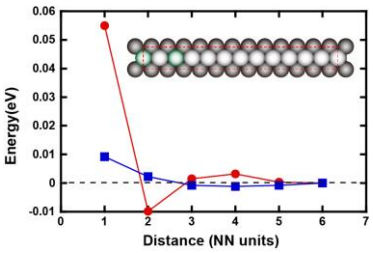


Fig. 1: Interaction energy as function of atomic distance. Red circles are for Cu-Cu pairs on the Ni(110) surface, and blue squares are for Ni-Ni pairs on the Cu(110) surface. Unit cell is indicated by a red broken rectangle in inset, and embedded Cu atoms for n=2 are indicated by green.

Table 1 Parameters for the present calculation

| | |
|---|---|
| VASP Version | 6.3.2 |
| slab geometry | 1×12 units 9 layers |
| k-points | 32×4 |
| potential | PBE [2] |
| cut off energy | 384.08 eV |
| Fermi level smearing | Methfessel & Paxton<br>σ = 0.12(Ni), 0.3 (Cu) eV |
| convergence condition | Electronic:$10^{-6}$ eV<br>Ionic: 0.01 eV/Ang. |
| SCF mixing parameters | AMIX = 0.02,BMIX = 0.0001<br>AMIX_MAG = 0.08<br>BMIX_MAG = 0.0001 |

The results shown in Fig. 1 clearly indicate attractive interaction both Ni-Ni and Cu-Cu pairs, which is direct confirmation of the clustering behavior of the two-dimensional Cu-Ni alloy.

## References

[1] T. Fukuda, T. Saito, I. Kishida, ACSIN-14, Sendai 2019, 23E28.

[2] J. P. Perdew, K. Burke, and M. Ernzerhof, Phys. Rev. Lett. 77 (1996) 3865.

# Search and realization of novel electronic properties of surfaces and interfaces and of nanostructures

Takeshi INAOKA
*Department of Physics and Earth Sciences, Faculty of Science, University of the Ryukyus, 1 Senbaru, Nishihara, Okinawa 903-0213*

This academic year, using the van-der-Waals density-functional theory, we investigated the electronic structure of the x-form phthalocyanine (Pc) crystal and the iodine doping effect on this structure. The Pc is a planar π-conjugated macrocyclic molecule which can include an atom of various species at its center. The x-form is one of several typical stacking forms of Pc in which molecular planes are perpendicular to the stacking axis. The x-form crystal is composed of a simple tetragonal lattice.

In each primitive unit cell of x-LiPc or x-NiPc, there are two molecules which are stacked along the c axis with a staggered angle of about 40° . The x-LiPc or x-NiPc is considered to be a Mott insulator because of its half-filled band. On iodine (I) doping, I atoms penetrate into one-dimensional (1D) open channels between x-form molecular chains, which results in x-LiPcI [1] or x-NiPcI [2]. Although x-LiPc or x-NiPc is a Mott insulator because of its half-filled band, doped I atoms oxidize partially Pc chains, shift the band occupancy from half-filling, and consequently leads to metallic nature [1]. In this analysis, we chosen SiPc and SiPcI, because a monomer of SiPc has a Si $p_z$-derived orbital just above the LUMO, and we expected x-SiPc to be 1D Si metal. However, as described below, dimerization of Si turns out to prevent formation of a metallic band.

We employed the program package 'Vienna Ab initio Simulation Package' (VASP) [3,4] on system B to optimize our structures.

To visualize our system, we show the optimized x-SiPcI structure in Fig. 1.

First, we consider the case without I doping. If we assume one period in the stacking direction, namely, one molecule in each primitive unit cell, we obtain a metallic band with about one-third occupied, and the cohesive energy per molecule of 1.82 eV. However, this is not the ground state.

In a single SiPc chain with two period, two Pc molecules in each primitive unit cell are stacked with a staggered angle 45° where eight C atoms nearest to the center Si atom in one molecule accord with those in the other molecule in projected position. This angle relation enables overlapping of $p_z$ orbitals of adjacent molecules at these C-atom positions. The cohesive energy is 3.41 eV which is larger than that of the above one-period system.

In the x-SiPc crystal without I doping, which includes intermolecular interaction, the staggered angle deviates to 38.4° . Although this angle is somewhat unfavorable in terms of the above-mentioned overlap of C-atom $p_z$ orbitals, s-orbital overlap occurs between two H atoms at the outer edges of neighboring molecule planes, as shown in the total electron density distribution in Fig. 2. This overlap can be ascribed to the fact that a number of k-states in some σ-bond dominant bands about 7 eV below the

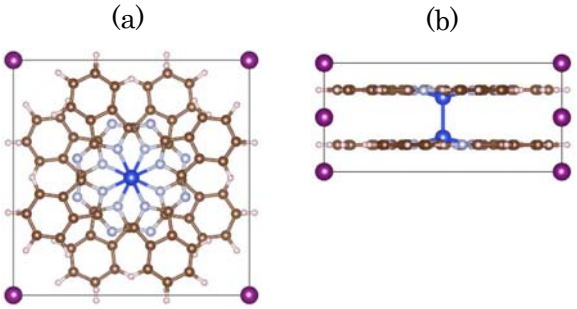


**Fig. 1** Optimized x-SiPcI crystal structure. (a) top view, (b) side view. As for circles, blue: Si, gray: N, brown: C, white: H, purple: I.

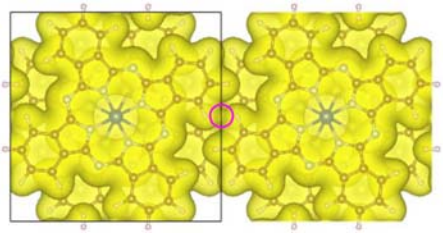

**Fig. 2** Total electron-density distribution of x-SiPc. The purple circle shows s-orbital overlap between two H atoms.

Fermi level have local orbitals like H molecules. The Si atoms dimerize in the stacking direction, as in Fig. 1 (b), which prevents formation of a metallic band owing to Si $p_z$ orbitals. The molecule cohesive energy is as large as 4.01 eV. Figure 3 (a) exhibits the band dispersion along the Γ–Z line in the stacking direction. The band b185, which is fully occupied, derives from Si $p_z$ orbitals. Two almost degenerate bands, each of which is spin-degenerate, are half-filled ones, which leads to Mott insulators, according to the experimental results of x-LiPc [1] or x-NiPc [2].

Iodine (I) doping to x-SiPc turns this insulator into a metal. Figure 3 (b) displays the band dispersion along the Γ–Z line for x-SiPcI. We can identify the I-derived bands by following the energy levels labeled red in this panel. The highest one of these band dispersions that passes the levels b199 and b195 decreases rapidly in energy and intersects the Fermi level. Since this implies appearance of a metallic band, we analyzed the electronic structure. Figures 4 (a) and (b) shows the top and side views of the electron density distribution of the state at the Fermi level which is arrowed and marked b195 in red in Fig. 3 (b). The metallic states along the I atomic chains are connected to π-electron systems extending around the outer edges of Pc molecular planes. We consider that I doping makes a wide range of x-form Pc crystals metallic, including LiPcI and NiPcI.

To verify existence of 1D metallic bands due to I atomic chains, we are performing further calculations taking more k points in the Brillouin zone and upgrading the calculational scheme to the hybrid density functional method with higher accuracy. We will report the confirmed results in a near future [5].

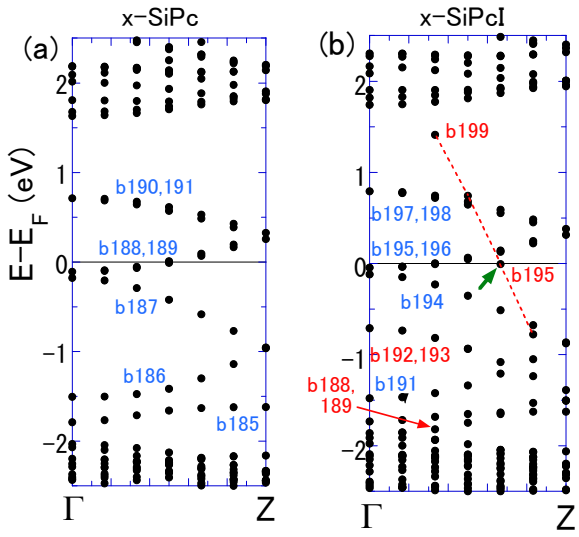


**Fig. 3** Band dispersion of (a) x-SiPc and (b) x-SiPcI along the c axis. The bands labeled in red in (b) stem from the I-atomic chains, and one of these bands crosses the Fermi level, as is eye-guided by a red broken line.

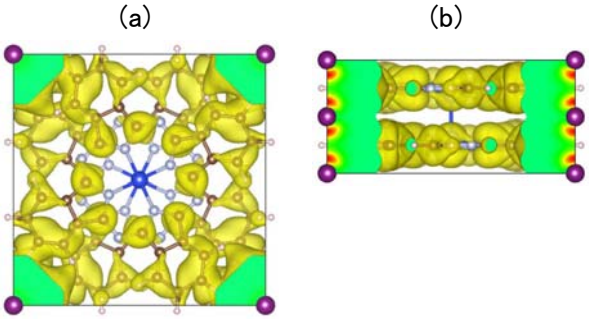


**Fig. 4** Electron-density distribution of the state at the Fermi level that is arrowed and labeled b195 in red in Fig. 3 (b). (a) top view, (b) side view.

## References

[1] R. Teruya et al., Angew. Chem. Int. Ed. **61**, e202206428 (1–6) (2022).
[2] C. J. Schramm et al., J. Am. Chem. Soc. **102**, 6702–6713 (1980).
[3] G. Kresse and J. Hafner: Phys. Rev. B **47**, 558–561 (1993).
[4] G. Kresse and J. Furthmüller: Comput. Mat. Sci. **6**, 15–50 (1996).
[5] T. Inaoka, to be submitted.

# DFT calculations of organic halogen molecules and their reaction products on metal surfaces

Noriyuki TSUKAHARA

*National Institute of Technology, Gunma College, Toriba-machi 580, Maebashi, Gunma, 371-0845, Japan.*

In this study, DFT calculations were carried out to clarify the contribution of intermolecular halogen and hydrogen bonds to the structures of the 1,3,5-tris(bromophenyl)benzene (TBB) molecular film on Ag(111) and Si(111) (√3×√3)-Ag surfaces [1]. In combination with STM experiments, the structure of TBB molecular films and the intermolecular interactions are clarified. Fig. 1 shows the spatial distribution of the differential charge density for the isolated TBB molecule and TBB assembly on Ag(111). The difference in the distribution between the isolated molecule and the TBB assembly is derived from electrostatic attraction with a Br atom in the neighboring TBB molecule for the TBB assembly. It indicates intermolecular halogen bond. Similar calculation indicates the intermolecular hydrogen bond on Si(111) (√3×√3)-Ag.

In addition, STM and DFT calculations were carried out to clarify the growth mechanism of the metal cluster using the metal-organic layer obtained by coupling reaction of TBB molecules on Ag(111) as a template [2].

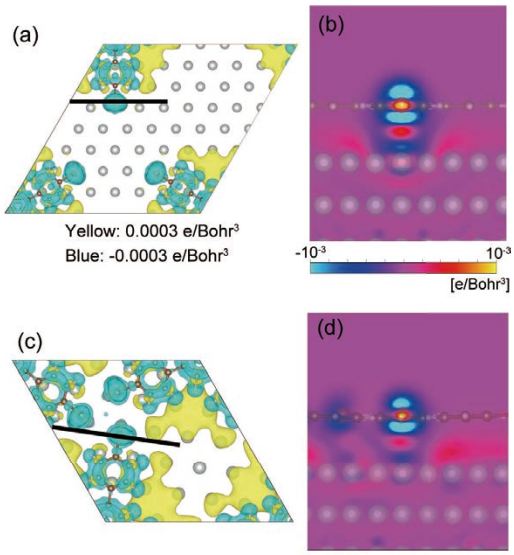


Fig. 1: The spatial distribution of the differential charge density for the isolated TBB molecule and the TBB assembly on Ag(111), and the vertical cross section of the distribution along the line in (a) and (c). Reprinted with permission from N. Tsukahara and J. Yoshinobu, Langmuir, **38**, 8881 (2022). Copyright 2022, American Chemical Society.

## References

[1] N. Tsukahara and J. Yoshinobu, Langmuir, **38**, 8881 (2022).

[2] N. Tsukahara, R. Arafune, and J. Yoshinobu, Langmuir, to be submitted.